ABSTRACT

Computational Modeling of Fiber Reinforced Composites Melt Flow in Nozzle Extrudate for Polymer Deposition Additive Manufacturing

Zhaogui Wang, Ph.D.

Mentor: Douglas E. Smith, Ph.D.

Understanding effects of processing conditions on properties of processed composite materials for polymer deposition additive manufacturing is critical, especially in the recent-emerging Large Area Additive Manufacturing (LAAM) polymer composite deposition technology. This dissertation aims to broaden the knowledge of how manufacturing inputs affect LAAM bead output properties (e.g., extrudate swell, fiber orientation, and effective elastic constants). The finite element method is applied to solve the flow kinematics and free surface shape of the nozzle-extrudate polymer melt that is defined by generalized Newtonian and viscoelastic flow models. The Folgar-Tucker Isotropic Rotary Diffusion (IRD) model and the Reduced Strain Closure (RSC) model are employed to compute the Advani-Tucker second order fiber orientation tensors throughout the flow domain of interest. The one-way weakly coupled and two-way fully coupled analyses of flow and fiber orientation in the nozzle-extrudate flow domain are both implemented separately.

The computed results, based on typical LAAM nozzle flow conditions, show that the non-Newtonian viscoelastic rheology effect significantly increases the die swell ratio of the Acrylonitrile Butadiene Styrene (ABS) melt by 50% as compared to the result predicted by using the Newtonian model. The swirling-flow-predicted fiber orientation tensor results yields a 25% increase in the predicted flow-direction elastic modulus of a 13% carbon fiber filled ABS (CF-ABS) as compared to that of a non-swirling simulation. It is also found that the bias of ignoring the screw-extrusion-resulted fiber length distribution in the prediction of elastic properties can be as large as 12%. Numerically predicted elastic properties from above studies exhibit a favorable agreement with related experimental measurements in the literature on similar materials and LAAM systems, which supports our proposed computational methodologies. Above results are obtained based on the weakly coupled formulation. Finally, it is found that the fully coupled interactions between the polymer melt flow and the fiber orientation has a pronounced impact on the nozzle-extrudate flow domain where the die swell of the free extrudate of 20% CF-Polyethylenimine reduces by a factor of ~2× as compared to the result of the neat polymer alternative. This agrees well with data appearing in prior experimental studies on similar filled-polymers.

Computational Modeling of Fiber Reinforced Composites Melt Flow in Nozzle Extrudate for Polymer Deposition Additive Manufacturing

by

Zhaogui Wang, B.S.E., M.S.M.E.

A Dissertation

Approved by the Department of Mechanical Engineering

_____

Paul I. Ro, Ph.D., Chairperson

Submitted to the Graduate Faculty of
Baylor University in Partial Fulfillment of the
Requirements for the Degree
of

Doctor of Philosophy

Approved by the Dissertation Committee

_____

Douglas E. Smith, Ph.D. Chairperson

_____

David Jack, Ph.D.

_____

Alex Yokochi, Ph.D.

_____

Jill Klentzman, Ph.D.

_____

Ronald Morgan, Ph.D.

Accepted by the Graduate School

December 2019

_____

J. Larry Lyon, Ph.D., Dean

Page bearing signatures is kept on file in the Graduate School.

TABLE OF CONTENTS

LIST OF FIGURES

LIST OF TABLES

ACKNOWLEDGMENTS

I would like to express my most sincere gratitude to my advisor Dr. Douglas E. Smith for all of his support and guidance through this research. He is a true mentor in not only my academic training but also in my life. Dr. Smith's spirit of teaching and rigorous attitude in research toughed me deeply. This five-year graduate study is a priceless gift given by him, which I believe will affect me in a lifelong period.

As well I would like to thank Dr. David A. Jack for his help in helping me debugging the MATLAB code, answering me many questions and many encouraging words that help me surviving from the PhD study. I would like to also thank Dr. Alex Yokochi, Dr. Ron Morgan, and Dr. Jill Klentzman for their willingness to be a member of my dissertation committee as well as for their help on the improvement of the dissertation content. A special thanks goes to all of my office mates that keep the office environment as stress free and lighthearted as possible. Last, I would like to thank my wife and parents for all their support and understanding for the long time I have spent on finishing this dissertation.

DEDICATION

To my beloved wife, QUN WANG, and parents, KAI WANG and YUJUAN ZHAO

CHAPTER ONE

Introduction

1.1 Research Background

Additive Manufacturing (AM) is a novel method for rapid prototyping of parts and tooling with intrinsic geometries that can be practically tailored to end-use structures in advanced industries such as automobile or aerospace. A typical AM process is to slice a three-dimensional Computer-Aided Design CAD model of a product into multiple two-dimensional in-plane outlines and then to manufacture the structure additively in a layer-by-layer fashion.

To date, AM technologies are emerging in several major formats, which often are categorized by their hardware setup and/or energy source for manufacturing. Stereolithography (SLA), Selective Laser Sintering (SLS), and Fused Filament Fabrication (FFF) are three of the mainstream techniques (e.g., also see Digital Light Processing (DLP) [1], Laminated Object Manufacturing (LOM) [2], etc.), which experience widespread applications. Specifically, Stereolithography (SLA) is an AM technique based on the photopolymerization phenomenon, where a light source energy changes the chains of molecules to be linked, and ultimately makes the liquid polymer feedstock in the base bath solidify to form a 3D object [3]. Alternatively, the Selective Laser Sintering (SLS) method employs the laser energy to melt material powders contained in a base plate. The powdered feedstock is first heated up to a temperature that is slightly below its melting temperature and a thin layer of heated powder is spread onto

the printing bed. Then, the laser source travels to selected points to increase the temperature above the melting point to fuse powder particles together. The dimensions of a printed part are defined through the locations of a laser exposure [4]. Both SLA and SLS techniques are capable of creating structures with relatively high dimensional accuracy, such that the industry average manufacturing tolerance is around 0.05 mm [5]. While SLA is limited exclusively to liquid polymer, the SLS technique may include a diversity of materials such as plastics, ceramics or metals. Nevertheless, both the hardware setup and material feedstock of SLA and SLS technologies are much more expansive as compared to other popular AM method, polymer deposition additive manufacturing, otherwise known as Fused Filament Fabrication (FFF). A typical process of FFF is where polymer filament feedstock is melted, extruded, and then deposited through a metal nozzle onto a heated platform, layer-by-layer, to form three-dimensional (3D) objects [6]. Compared to SLA and SLS, the FFF method is a relatively low-cost AM approach in terms of both hardware and material feedstock, even though the typical printing resolution is a little bit higher (i.e., 0.2 mm [5]). In addition, FFF-fabricated parts exhibit relatively high material stiffness and strength as compared to those manufactured through layer-melting processes, especially when fiber reinforced polymer composites are employed as feedstock (e.g., see [7, 8]). However, the dimensional accuracy of FFF method is lower as compared to SLS or SLA technique. A brief summary of the advantages and disadvantages of SLS, SLA, and FFF appears in Table 1-1. Readers interested in further exploring the recent innovations in AM technologies are referred to the review papers published to date (e.g., see [9-11]).

Table 1-1. Summary of three major additive manufacturing technologies.

Technology name	Advantage	Disadvantage
Stereolithography	High accuracy, fast printing speed	High cost, low material stiffness and strength
Selective Laser Sintering	High accuracy, fast printing speed	High cost, porous structure, high material waste
Fused Filament Fabrication	High material elastic properties, low cost	Low accuracy, relatively low printing speed

Based on the fundamental concept of the polymer deposition process (i.e., FFF), researchers have developed the Large Area Additive Manufacturing (LAAM) polymer deposition technology by employing a vertical single screw extruder to melt and deposit pelletized thermoplastics rather than using filament feedstocks, which yields a significant increment in the material output rate. In addition, the material deposition rate of large-scale AM machines is also increased as compared to most desktop-size printers, typically from 0.04 lbs/hr (i.e., roughly 1 lb per day) for a typical desktop device to upwards of 100 lbs/hr for today's LAAM machine [12]. The development of LAAM applications has enjoyed a rapid pace. To date, the maximum material output rate per hour of a LAAM system is over 200 times higher than that of a conventional desktop FFF printer [12]. Researchers from Oak Ridge national Laboratory (ORNL) and their industrial collaborators from Cincinnati, Incorporated (Harrison, OH, USA) developed the Big Area Additive Manufacturing (BAAM) system which is the first of few LAAM systems. The BAAM machine has the ability to print parts in size up to 6-meter length × 2.5-meter width × 1.8-meter height with material output rates up to 45 kg/h (dependent on the choice of material) [13]. In a similar fashion, Thermwood Incorporated created a Large Scale Additive Manufacturing (LSAM) system that offers an even larger print size capability (30-meter length × 3-meter width × 1.5-meter height) and higher maximum

material output rate (up to 226kg/h) as compared to the BAAM system. The LSAM system is also fitted with a Computer Numerical Control (CNC) router such that a printed part can be machined following the polymer deposition process [14].

Unfortunately, the inherent weak meso-structures of LAAM printed parts significantly reduce their stiffness and strength when virgin polymer materials are used. Prior research has shown that adding fibers into a neat polymer significantly enhances the mechanical performance of the polymer composite structure (e.g., see [7, 8]). The superior mechanical properties of filled polymers over their neat polymer alternatives reduce warpage and enhance dimensional stability and material stiffness of a printed structure. Carbon fiber reinforced materials are one of the most commonly used types of feedstock in LAAM applications. For example, the BAAM created Strati car is the first 3D printed car which is made of 13% carbon fiber reinforced Acrylonitrile Butadiene Styrene (ABS) [15]. A significant advantage of using of carbon fiber fillers is their low Coefficient of Thermal Expansion (CTE) which greatly improves the dimensional stability of the printed part. Although filled-polymers enhance the mechanical performances of the LAAM-produced parts, the reinforcements also cause severe issues during the manufacturing (e.g. severe clogging in FFF-type nozzles in commercial printers, especially at high fiber volume fraction [16]). The material anisotropy is also found to be even more pronounced in deposited beads, where the material stiffness transverse to the print direction is much lower than the enhanced stiffness along the print bead axis. Obtaining acceptable bead transverse mechanical properties is one of the vital limiting factors in the applicability of the large-scale AM technology [12], which may be improved by z-pinning printing (e.g. see [17]) or adding rotational kinematics into the

melt deposition flow to change the microstructural fiber orientation within the composite extrudate during manufacturing (e.g., see [18]).

Figure 1-1 shows the microstructure of a LAAM-deposited composite material bead which directly affects the mechanical properties of printed structures. The microstructure of the short fibrous composites feedstock includes fibers with specific alignment, polymer matrix, and voids in between fibers and the matrix, which are all sensitive to the LAAM fabrication process, e.g., a small variation in the processing condition settings can result in notable different fiber orientation states in the deposited composites [19]. Currently, a lack of fundamental understanding of the effect of processing conditions on the resulting fiber orientation and associated elastic performances of printed composite parts yields a cumbersome and tedious trial-and-error approach when setting print parameters for LAAM. More significantly, the unpredictable material performances of the manufactured parts greatly reduce the applicability of the LAAM deposition technology. This dissertation is designated to extend the fundamental knowledge base that explains the effects of polymer flow characters in LAAM applications on the resulting microstructure of end-use printed parts made of short fiber composites. The gained knowledge is expected to improve the ability to print superior material microstructures in LAAM polymer deposition. Additionally, this document will not specifically discuss the microstructure-level voids within the composites (which may be generated by the tumbling motions of the fibers [20]) as it beyond the main scope of this dissertation that mainly aims in quantifying the fiber orientation kinetics in the LAAM nozzle extrudate flow scenario.

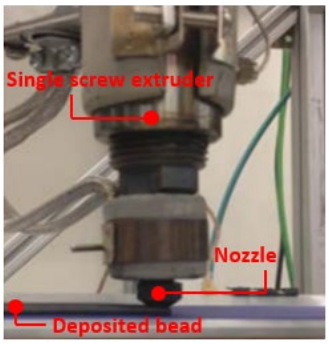

(A)

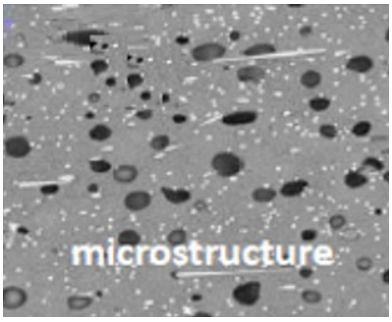

(B)

Figure 1-1. (A) Polymer deposition manufacturing and (B) microstructure of a deposited bead of 13% Carbon Fiber filled Acrylonitrile Butadiene Styrene (CF-ABS): White is fiber, black is void and grey is polymer matrix [21].

1.2 Research Objective

It is well understood that the structural and thermal responses of a part made of fiber reinforced polymers are greatly influenced by the material's microstructure formations [22-24]. What remains unclear in polymer deposition additive manufacturing is how molten polymer flow orients the reinforced particles as the feedstock is extruded and deposited. In addition, the mutual effects between the polymer melt and orientation of reinforced fibers during deposition also play important role in the contribution of the final performances of a printed part. Hence, it is critical to establish a bridge to correlate the microstructural formation of the filled polymer to the polymer deposition process inputs, especially when large area manufacturing is of interest.

The objective of this research is to expand the knowledge base on quantifying the interactions between the polymer flow and the reinforced fibers' orientation kinematics during a LAAM polymer deposition. The obtained knowledge is expected to help researchers identifying the process-structure-property relations between the microstructure of short fiber composites feedstock and process conditions of the LAAM technology, which avoids otherwise the tedious and costly trial and error process for the

technology. We ultimately hope to enrich the potential applicability of this energy-efficient manufacturing technology, making it more broadly useful in engineering design and manufacturing. In particular, to realize the overall goal, several sub-objectives are specified as follows: I) Understanding effects of flow rheology modeling on predicted outcomes (e.g., flow kinematics and free surface extrudate swell). II) Explaining the importance of tooling on resulting fiber orientation and associated elastic properties of the overall composite feedstock (e.g., the screw swirling kinematics impacts and the fiber length attrition effects). III) Exploring the fully-coupled interactions between the polymer flow and fiber orientation kinetics in the post extrudate (e.g., anisotropic material behaviors of composites including the shear viscosity and the elastic properties). In addition, this research mainly investigates two material systems: the neat Acrylonitrile Butadiene Styrene (ABS) and the 13% Carbon Fiber filled Acrylonitrile Butadiene Styrene (13% CF-ABS) provided by PolyOne Corp. (Avon Lake, OH, USA). This enables us to evaluate the material behaviors of a polymer under both unfilled and filled conditions.

1.3 Dissertation Outline

The focus of this PhD research includes the flow-induced fiber orientation and the effects of fiber fillers on the polymer suspension rheology and mechanical properties of the LAAM-deposited composites. There are numerous factors within a LAAM process affecting the flow kinematics of the molten polymer, including but not limited to the effects of polymer rheology, influences of tooling components (e.g., screw design, nozzle design) of a LAAM system, and flow/fiber-orientation coupling effects.

This dissertation models significant polymer composite melt flow features within the manufacturing process of the LAAM technology and analyzes the inter-relations between the polymer matrix flow and the flow-induced fiber orientation, and ultimately predicts the mechanical performance of a deposited composite bead. The rest of the document is organized as follows:

Chapter Two reviews the literature addressing the numerical identifications associated with the large-scale polymer deposition additive manufacturing, especially for the processes of the single screw extruder material feeding and the melt extrusion of the feedstock of fiber reinforced polymer composites.

Chapter Three provides a fundamental overview of the theories that are applied in the modeling work presented in this dissertation, including the governing equations of the polymer flow and the associated flow-induced fiber orientation. The constitutive equations that couple the interactions between the flow and fiber orientation in a polymer composite suspension are reviewed as well. In addition, the orientation homogenization method is discussed, which is used to predict the elastic constants of the post-extrudate of composites from LAAM applications.

Chapter Four presents a numerical methodology investigating the effect of non-Newtonian viscoelastic rheology of polymer materials on the resulting melt extrudate swell and fiber orientation for a LAAM nozzle extrudate flow. This chapter is based on the paper "Rheology Effects on Predicted Fiber Orientation and Elastic Properties in Large Scale Polymer Composite Additive Manufacturing" in the *Journal of Composites Science*. The first author, Zhaogui Wang, carried out the main work of experiments and numerical simulations, and wrote the initial draft. The correspondence author, Douglas E.

Smith, conceived and designed the experiments and numerical modeling procedure, and mentored the first author, Zhaogui Wang, in writing this paper.

Chapter Five analyzes the impact of screw swirling kinematics in LAAM applications on the resulting flow fields and associated fiber orientation state of the extruded composites. This chapter is based on the paper "Numerical Analysis of Screw Swirling Effects on Fiber Orientation in Large Area Additive Manufacturing Polymer Composite Deposition" in the *Composites Part B: Engineering*. The first author, Zhaogui Wang, carried out the main work of experiments and numerical simulations, and wrote the initial draft. The correspondence author, Douglas E. Smith, conceived and designed the experiments and numerical modeling procedure, and mentored the first author, Zhaogui Wang, in writing this paper.

Chapter Six investigates the fiber length attrition resulting from the aggressive screw extruder feeding process and related effects on the predicted elastic properties of extruded composite materials.

Chapter Seven provides a finite-element-based custom MATLAB code characterizing the mutually dependent interactions between the polymer melt flow and the fiber reinforcements orientation in an open flow of melt extrusion which simulates the nozzle-extrudate flow for LAAM applications.

Chapter Eight summarizes the accomplishments obtained throughout Chapters Four to Seven and recommends the future work regarding the achievements obtained with above studies.

CHAPTER TWO

Literature Review

To facilitate the introduction of the LAAM polymer deposition application, a custom-designed large area polymer composite deposition system is adopted, which was built at Baylor University. As shown in Figure 2-1, the system is mainly composed of a Strangpresse (Youngstown, OH, USA) Model-19 large-scale single screw extruder, associated gantry system consisting of a 4-feet-by-4-feet printing substrate and 6-inch room for vertical-direction manufacturing, and the computer-supervised control system. A typical process of LAAM polymer deposition is where pelletized feedstock is compounded by a screw extruder and then deposited through a heated nozzle onto a preheated print-bed at atmospheric pressure. During this process, a circular extrudate is formed into an elliptical deposited bead. Virgin thermoplastics printed parts exhibit severe defects such as warpage and low material stiffness and strength. Alternatively, short fiber reinforced polymer composites are extensively adopted for LAAM applications [12, 13, 25] which significantly improves the performances of end-use fabricated parts (e.g., see Figure 2-2, where the bar printed by using 13% CF-ABS exhibits less warpage to that printed by using neat ABS [25]). However, the second-phase reinforcements also bring up significant issues regarding the LAAM fabricating process such that the unpredictable microstructure of the polymer composites processed through the LAAM applications requires tedious empirical pre-testing to find proper printing condition parameters associated with different composite materials applied.

The primary focus of this dissertation is to explain the unclear relationships between the feedstock of short fiber reinforced composites and the manufacturing process of the LAAM polymer deposition. This ultimately provides insights to design and optimize the process of LAAM technologies towards end-used printed-parts with superior mechanical performances. Numerical simulations are often regarded as an important way to identify the complex physics behind the manufacturing. In this chapter, we review preceding articles numerically addressing the physic phenomena that occur during polymer deposition processes, including processes of feedstock feeding, nozzle extrusion, post-extrusion extrudate swell and material deposition.

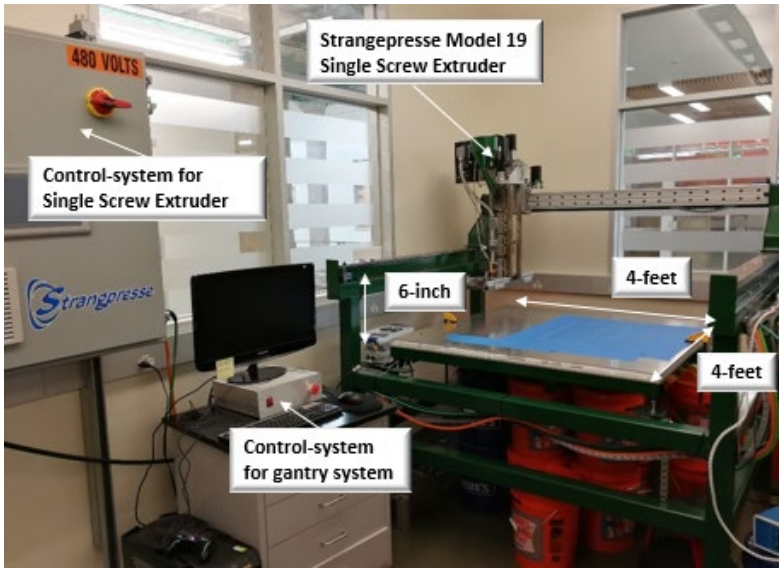

Figure 2-1. Baylor Large Area Additive Manufacturing (LAAM) system.

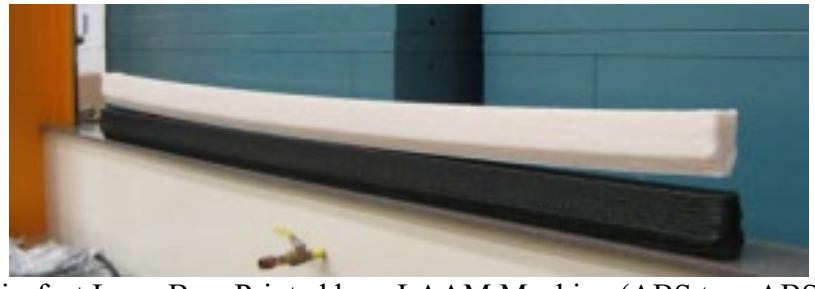
Figure 2-2. Six-feet Long Bars Printed by a LAAM Machine (ABS top, ABS/CF 13% bottom) [25].

2.1 Feedstock Feeding

Ramanath, et al., [26, 27] modeled the extrusion liquefier flow of a FFF process in a 2D planar model for the bio-polymer Polycaprolactone (PLC). The flow kinematics fields, temperature fields and the pressure gradients of the flow within the liquefier were studied. Mostafa, et al. [28] developed a liquefier head flow simulation for both 2D and 3D models for an iron powder reinforced ABS material, and the flow fields along with the pressure drop and temperature fields of the composite ABS melt were examined. Unfortunately, most of the prior studies focus on the conventional filament-extrusion process. Specifically, the single screw extrusion feeding process is different from what has been investigated above for traditional FFF processes. For example, the built-up pressure for a vertical extruder is pivotal for successfully extruding the composite materials while the pinch-roller filament extrusion needs more delicate calibration between the liquefier and the nozzle to avoid bending of filaments [29]. In the following, we particularly explore the associated literature in screw-involved extrusions of filled polymers (not limited to AM applications).

Single screw extruders are often seen in the material feeding system of LAAM applications. Herein, we take the Baylor LAAM system as an example (c.f. Figure 2-1) to facilitate our introduction. In detail, the Baylor LAAM system adopts a Strangpresse Model 19 single screw extruder provided by Strangpresse Corp. (Youngstown, OH, USA, a licensed extruder manufacturer partnership with ORNL). The Model-19 extruder is designed for large volume polymer deposition AM application, which has the capability to extrude polymeric based material up to 20 lbs. per hour. As can be seen in Figure 2-3, the temperature of three zones, including the feeding zone, compression zone and the

metering zone of the Model 19 single screw extruder, can be adjusted. The extruder has a maximum Motor RPM of 90 rad/s which yields a volumetric flow rate up to 1.5×10^{-6} m^3/s for virgin ABS and 13% CF-ABS [30]. While the internal design of the extruder is not available to us, the feeding mechanism of screw extrusion can be easily found in existing literature (e.g., see [31]) and is not given in detail here as this is beyond the main focus of the dissertation.

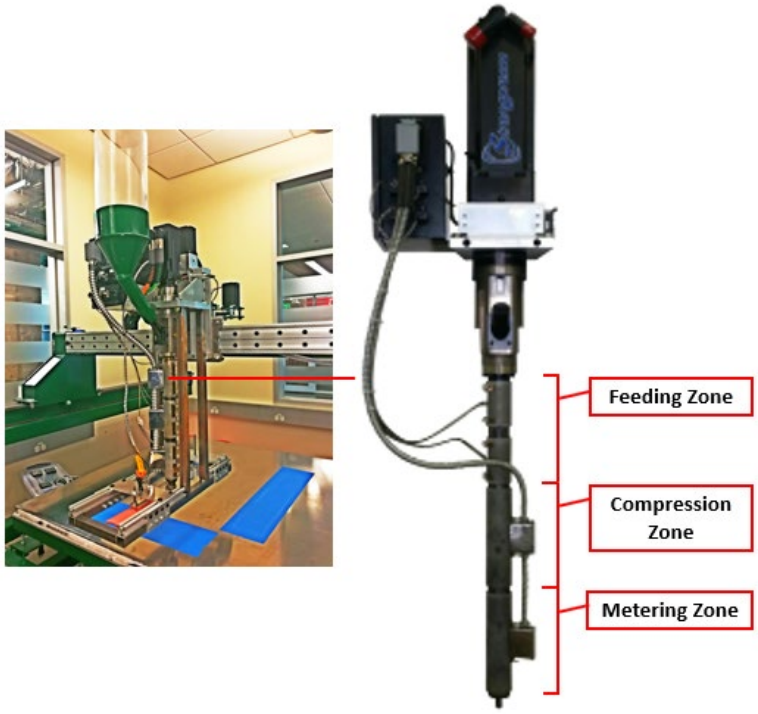

Figure 2-3. Strangpresse Model 19 Extruder Involved in the Baylor LAAM System.

It is important to note that the screw-involved feeding process is different from that of a pinch-roller filament extrusion, which is typically employed in the FFF technique, especially when short fiber filled polymers are used as the feedstock. For instance, the fiber orientation within the filament is predominately parallel to the extrusion direction due to the fabrication process of the continuous filament extrusion, while the pelletized feedstock may exhibit more diversity in terms of the fiber orientation

due to the unique swirling kinematics generated during the screw rotation [18]. Additionally, the fiber attrition of a screw extrusion is much more severe than the smooth transition in traditional FFF process (e.g., see [32]), which yields a significant reduction on the property enhancements of the extrudate composites as the fiber aspect ratio reduces greatly. In the following, we review articles discussing the potential effects of the screw extrusion process onto the extruded fiber reinforced composites, with a specific focus on the property variations of the feedstock due to the screw extrusion process.

The single screw extruder has a distinctive way of feeding polymeric-based feedstock as compared to other methodologies such as the hydraulic piston pression. For instance, the interactions between the rotational screw and the pelletized feedstock yields intense viscous heating on the polymer materials and ultimately varies the apparent shear viscosity of the melt. More importantly, for filled polymers, the screw barrel cuts off the reinforced fibers into smaller pieces, which significantly changes the rheological behaviors of the molten composite fluid flow. In particular, previous literature demonstrated the single screw rotation had a direct effect on the properties of an extruded composite material. For example, Ke, et al. [33] used simulation to show that the viscosity dropped initially and then tended to recover in single screw extruder flows. This trend appeared to be periodic and related to the geometry of the screw. Canevarolo, et al. [34] explored the effects of various screw element types on the degradation of Polypropylene (PP). Five different screw designs were employed to show that increasing the screw number as well as the screw profile aggressiveness yielded a noticeable reduction in the average molecular weight of PP. Kelly, et al. [35] experimentally measured the melt temperature profiles in single screw extrusion flow using various

screw geometries. Ramani, et al. [36] investigated the fiber length degradation in a twin-screw extruder. The reported data indicated that the injection molding process did not benefit from the screw-yielded wet-out and dispersion of fiber reinforcements. More recently, Duty, et al. [12] measured the structural performances of fiber reinforced polymers printed with Big Area Additive Manufacturing (BAAM). The measured stiffness of 13% CF-ABS beads showed that the printed material exhibited a high degree of anisotropy owing to the fiber orientation within the extrudate, where the elastic modulus in the print direction is much higher than those normal to the axis of the printed bead. In addition, their work revealed that screw design (cf. Figure 2-4) significantly affected the resulting elastic properties of the printed materials, such as the principal modulus (that parallel to the printing direction). Duty showed that the elastic modulus 20% glass fiber reinforced ABS bead printed with a conventional screw was 5.67 GPa, while that using a retrofit screw was 3.33 GPa (cf. Figure 10 in [12] for screw geometric designs).

(A) (B)

Figure 2-4. Screw Designs for Big Area Additive Manufacturing Machine: (A) Custom-designed Retrofit Screw; (B) Original Dohle Extrusion Screw [12].

While improving the efficiency of material feeding, the aggressive screw extrusion process also yields negative side-effects on the fibers reinforced in the processed composite material. Hausnerova, et al. [37] showed that the high shear force yielded by the single screw rotation has a direct effect on degrading the geometry of the reinforced fibers. In addition, Aigner, et al. [38] studied the fiber breakage condition of a

glass fiber polymer composite using X-ray computed tomography. They found that the single screw extruder compounding and extrusion process led to a roughly 50% reduction in the maximum fiber length (e.g., reduces from ~2 mm to 1 mm) compared to the manufacturer's specification sheet. Several studies investigated the degradation of fiber length for long fiber reinforced composites in injection molding applications, where the effects of different processing conditions of the screw extrusion (e.g., melting temperature [32], residence time [39], molding pressure [40]) are explored. Jin and Wang [41] and Phelps, et al. [42] presented theoretical formulas to predict the fiber length reduction of Long Fiber Thermoplastic (FLT) in a injection molding process. Results obtained by Phelps' study showed a good agreement with corresponding experiments on glass-fiber/Polypropylene FLT molding. Bereaux, et al. [43] conducted numerical simulations that depicted the fiber breakage in a single screw extrusion process. In their study, the model sensitivity to different screw processing parameters, such as the material viscosity, barrel temperature, and screw geometry, were evaluated. Furthermore, prior literature stressed the importance of the geometries of fiber fillers on determining material properties of the polymer composite processed through the screw extrusion. Bayush, et al. [44] studied the fiber length distribution of a natural fiber reinforced polypropylene and concluded that maintaining the critical fiber length and minimizing the fiber breakage would enhance the mechanical and dynamic properties of the overall compound. In another study of natural fiber filled plastics, Gamon, et al. [45] pointed out the longer fibers would benefit the flexural strength of the extruded composite. Inoue, et al. [46] also emphasized the vital character of the fiber length in the mechanical properties of the mixed composite in their study of the effects of the screw design on the

fiber breakage and dispersion. Additionally, Hausnerova, et al. [37] proposed that the shear viscosity and die swell of filled polymers would decrease in high shear rates screw extrusion owing to the fiber length reduction and the polymer matrix degradation. With the above review, it is seen that the geometrical loss of reinforced fibers in the short fiber composites may also play a significant role in varying the material properties of LAAM-extruded composite materials.

2.2 Nozzle Extrusion

Simulations associated with the thermoplastic feedstock flow in the polymer deposition process have been carried out for decades, such as the thermal history in the extrusion liquefier [26] and the nozzle region [27]. In addition, a few studies focused on the deposition process, which includes the extrudate swell [19, 47], bead-bead interactions (i.e., inter-layer bonding [48], crystallization [49], and thermal residual stresses [50]). As mentioned above, fiber reinforced polymeric-based composites are largely employed for LAAM applications to improve the mechanical performances of end-use printed parts from LAAM processes [12, 25]. Unfortunately, once the second phase reinforcements are added into the thermoplastics, the melt flow behaviors during the deposition process become more complex as compared to those studied for virgin polymers [51]. It is important to note that the flow fields within the nozzle orifice induce the fiber fillers to orient to a certain alignment, which greatly determines the material properties of a deposited bead [19, 52]. On the other hand, the fiber reinforcement alters the rheological behaviors of the fluid flow, which in turn affects their own alignment [53, 54]. In the rest of this section, we mainly focus on the melt extrusion process in the nozzle orifice, which is usually the very last component of the extrusion process before

the molten composite feedstock is extruded and deposited onto the substrate. At this stage, the material flow and the orientation of reinforced fibers interact with each other, and the resulting fiber alignment within the extrudate is a major factor in determining the mechanical properties of the deposited composite beads. Hereinafter, we explore the numerical simulations conducted in previous studies that focus on the fiber suspension flow in the extrusion nozzle and nearby extrudates.

Fiber orientation analysis on the composite material flow for polymer deposition AM exhibits a notable increase as short fiber reinforced polymers continue to see increased applications in this technology. Nixon, et al. [52] investigated the fiber orientation pattern of the polymer composite feedstock in the nozzle of a commercial FFF printer using the Moldflow software. The fiber orientation is computed through the Folgar-Tucker model [23] implemented in Moldflow. They found that a convergent nozzle geometry resulting in a higher fiber reinforcement than a straight nozzle and a divergent nozzle. But Nixon did not include the effect of die swell at the nozzle exit in the computation of the fiber orientation. Heller, et al. [19, 30, 55] conducted the first few studies that assessed the impact of extrudate swell on fiber orientation in FFF-type additive manufacturing. Their work simulated the extrudate swell of a carbon fiber filled ABS in vertical extrusion [19] and planar deposition [30, 55] scenarios, assuming a Newtonian creeping flow for the molten ABS composite. The free surface location was identified by minimizing the normal stress over the free surface to a value near zero through an optimization formulation. The fiber orientation tensors were computed by the Folgar-Tucker model [22, 23]. They found that the die swell decreased the fiber alignment along the loading direction and reduced the axial tensile modulus of the

extruded composite material by 20% [19]. Russell, et al. [55] reported the Coefficient of Thermal Expansion (CTE) of the ABS composite material using the same flow model as proposed in Heller, et al [19] with the advanced Reduced Strain Closure (RSC) fiber orientation prediction model [56]. A parametric study on different parameters associated with the RSC model was conducted and the computed results were compared with their experimental data [55]. On the other hand, Lewicki, et al. [57] modeled the flow of an 8% vol. carbon fiber filled epoxy in the tip of a printed nozzle, where the fiber inclusions were characterized as individual particles and thus the fiber-fiber interaction and fiber-wall interaction were carefully considered. However, due to the high computational cost of modeling every fiber, the fiber orientation of the flow is not calculated but assumed based on the flow velocity fields.

2.3 Post-extrusion Die Swell

Extrudate swell occurs not only in the LAAM polymer deposition process but many extrusion-based polymer processing applications as well. Heller, et al. [19] evaluated the extrudate swell of the LAAM process, where a Newtonian flow model was employed. While melt flow of thermoplastics is known to exhibit strongly non-Newtonian behaviors, which have a direct impact on the die swell. Crochet, et al. [58] theoretically analyzed the die swell of an upper-convected Maxwell fluid based on the mixed finite element method for fluids with implicit constitutive equations. Luo and Tanner [59] applied the Streamline Finite Element Method (SFEM) to the die swell problem, which avoided the numerical instability in high Weissenberg number problems. Luo and Mitsoulis [60] extended the SFEM by adding in a particle-tracking scheme along the streamlines with a Picard iterative scheme. Béraudo, et al. [61] applied a finite-

element-based method to investigate the extrudate swell of LLDPE and LDPE melts using a multi-mode Phan-Thien-Tanner (PTT) model. Their approach provided an accurate die swell prediction for die geometries of a 2D slit die and a 2D axisymmetric capillary die in low and intermediate shear conditions. Ganvir, et al. [62] applied an Arbitrary Lagrangian Eulerian (ALE) algorithm to calculate the extrudate free surface which enabled the die swell simulations to be performed in both steady state and transient problems. Alternatively, Limtrakarn, et al. [63] employed the Simplified Viscoelastic (SV) model implemented in ANSYS-Polyflow to predict die swell of a 3D circular die flow of LDPE. A good agreement between the numerical results and the experimental data was achieved. Clemeur, et al. [64] found that the SV model was a cost-effective approach for evaluating the flow-viscoelasticity as compared to conventional viscoelastic fluid flow models including the Oldroyd-B and the PTT models.

The reviewed works appearing above primarily focused on virgin polymer systems mostly, where the effects of fiber reinforcements on the flow fields are ignored. As mentioned previously, the presence of fibers and their specific alignments contribute to the stress field of the flow (i.e., fully coupled formulation, see, e.g., Equation 3-28 in next chapter), which essentially may vary the behavior of the die swell of the melt. Papanastasiou and Alexandrou [65] and Rosenberg, et al. [66] investigated the die swell phenomenon of an open flow with a fully-coupled flow-fiber scheme, where the flow fields were solved through the Galerkin Finite Element Method (GFEM) and the fiber orientation equation was solved through flow streamlines with some type of numerical integration. While the Newtonian flow model is adopted in both of their works, the

quantification of the fiber effects on the free surface extrusion flow stresses the importance of the fully-couple formulation in open extrusion applications.

2.4 Material Deposition

Bellini [67] was one of the first few researchers to characterize the shape of a free extrudate for a Fused Deposition Modeling (FDM) process assuming a temperature-dependent non-Newtonian power law viscous flow. Bellini simulated the vertical extrudate as well as an extruded and deposited bead using 2D planar models for ceramic materials. Recently, Heller, et al. [30] developed a 2D planar model to simulate the polymer flow deposition process for LAAM applications, where the planar swell of the bead during material deposition with respect to different deposition distance (i.e., distance between nozzle end to print-substrate) was investigated through the commercial software COMSOL (Burlington, MA, USA). The swelled shape of the free extrudate was captured by an optimization MATLAB (Natick, MA, USA) subroutine live-linked with the COMSOL simulation.

It is important to note that designs of the to-be-printed structure and their associated printing paths contribute significantly to the mechanical performances of the end-use printed parts. Researchers attempted to optimize the material properties of printed parts from different perspectives including the interlayer bonding [68], crystallization [50], thermal history and residual stress layout [48], etc. Nevertheless, physical phenomena that occur after the first-layer bead-deposition are beyond the main scope of this dissertation and will be explored much beyond this point. Interested readers are referred to a few recent review papers such as Brenken, et al. [51].

CHAPTER THREE

Theoretical Basis

Generally, we explain the co-relations between the LAAM polymer deposition process and the fiber reinforced polymers feedstock through the following three steps: I) Modeling the flow fields of filled polymer melt in the nozzle region plus a short section of post extrudate. II) Solving the fiber orientation along the modelled flow domain with the achieved flow kinematics. III) Predicting the elastic constants of the post-extrudate of composite materials with an orientation homogenization method. This three-step analyzing procedure composes the weakly coupled analysis, which assumes that the flow fields induce the fiber orientation but are not affected by the presence of fibers. In contrast, the fully coupled formulation solves the flow fields and fiber orientation fields simultaneously. This chapter gives an overview of the basic theories associated with the proposed two solution schemes as follows.

3.1 Governing Equations for Polymer Melt Flow

One of the first key factors in the polymer composite deposition AM process is identifying the features of the flow fields of the filled-polymer melt flow as the molten feedstock extrudes through the nozzle and is then deposited onto a substrate. Because the flow kinematics around the nozzle orifice induce the reinforced fiber to re-orient, and the resulting fiber orientation pattern within the extruded composite greatly determines the material properties of solidified deposited beads [22]. Typically, the thermal gradient of the polymer composite melt in nozzle extrusion scenarios exhibits trivial variation [69].

In other words, the polymer flow of nozzle extrusions can be regarded as an isothermal event. In addition, it is also typical (e.g., see [53, 70, 71]) to assume an incompressible, and highly viscous creeping flow (due to that most polymer melt flows exhibit low Reynolds numbers, i.e., ~10^{-5} [72]) for polymer processing of thermoplastics. Ultimately, the thermal effects, inertia effect, and the time transient effect are neglected for modelling the flow in a nozzle extrusion scenario for LAAM applications. Under these assumptions, the mass and momentum conservation equations of the flow field can be, respectively, written as [73]

$$\nabla \cdot \boldsymbol{v} = 0, \tag{3-1}$$

and the conservation of momentum as [73]

$$\nabla \cdot \boldsymbol{\sigma} + \rho \boldsymbol{f} = 0, \tag{3-2}$$

In the above, "$\nabla \cdot$" refers to the divergence operator, t refers to the time. ρ is the density of the fluid, $\boldsymbol{f}$ is the body force vector, and $\boldsymbol{v}$ and $\boldsymbol{\sigma}$ denote separately the velocity vector and the Cauchy stress tensor. Among them, the Cauchy stress tensor $\boldsymbol{\sigma}$ can be written as

$$\boldsymbol{\sigma} = \boldsymbol{\tau} - P\boldsymbol{I}, \tag{3-3}$$

where P is the pressure. $\boldsymbol{I}$ is the identity tensor and $\boldsymbol{\tau}$ is the stress tensor that relates to the shear deformation. For Newtonian viscous fluids, $\boldsymbol{\tau}$ can be written as

$$\boldsymbol{\tau} = 2\eta \boldsymbol{D}, \tag{3-4}$$

Here, η is the viscosity of the fluid without considering the effects of the any fibers. In other words, the flow governing equations shown here are designated for the weakly coupled analysis of the fiber suspension flow applications. In addition, $\boldsymbol{D}$ is the rate-of-deformation tensor that equates the symmetric part of the velocity gradient tensor as

$$\boldsymbol{D} = (\nabla \boldsymbol{v} + \nabla \boldsymbol{v}^T)/2, \tag{3-5}$$

where "T" denotes to the matrix transpose operator. In addition, it is also worth noting that the skew-symmetric part of the gradient field forms the vorticity tensor $\boldsymbol{W}$ such that

$$\boldsymbol{W} = (\nabla \boldsymbol{v} - \nabla \boldsymbol{v}^T)/2, \tag{3-6}$$

3.1.1 Rheological Models for Molten Polymer

A specific perspective in modeling the polymer melt flow is to properly define the material rheological properties of the fluid flow, which is especially important for molten thermoplastics, that exhibit intense non-Newtonian behaviors [73]. Therefore, we review several of the most widely used rheological models that characterize the flow behaviors of polymer melts in the following.

The Newtonian fluid model is the most simply form of a rheological model that describes the viscosity of a fluid as a constant such that [73]

$$\eta = \eta_o, \tag{3-7}$$

where η_o is often referred to as the Newtonian viscosity or zero-shear-rate viscosity. While the Newtonian model has been seen in the preceding literature for LAAM melt flow modeling [19, 55], most thermoplastics exhibit shear-rate-dependent viscosity under semi-molten conditions. Moreover, feedstock used in LAAM polymer deposition often exhibits the shear thinning behavior, such that the shear viscosity of the melt reduces with increased shear rate [73], which can be captured by a few Generalized Newtonian Fluid (GNF) models. The Power law model is a widely-used GNF model that experiences extensive applications in polymer processes. The equation of the Power law model can be written as [73]

$$\eta = K(\lambda_c \dot{\gamma})^{n-1}, \tag{3-8}$$

where $\dot{\gamma}$ is the shear rate, λ_c is the natural time (equates the reciprocal of a reference shear rate [74]), K is the consistency index, and n is the power-law index. The Power law model is able to depict the viscous behaviors of polymer materials with shear rates over a few decades (the interval of such shear rate is also called the power-law region). However, the Power law model fails to represent the Newtonian viscosity at low shear rate, which can be characterized by some other models, such as the Carreau-Yasuda model or cross law model. In detail, the Carreau-Yasuda model can be written as [73]

$$\eta = \eta_\infty + (\eta_o - \eta_\infty)\left[1 + (\lambda_c\dot{\gamma})^{a^c}\right]^{\frac{n-1}{a^c}}, \tag{3-9}$$

Here, η_∞ refers to the infinite-shear-rate viscosity and a^c is the transition index that controls the viscosity transfers from the Newtonian plateau to the power-law region. In addition, the Cross law model can be written as [73]

$$\eta = \frac{\eta_o}{1+(\lambda_c\dot{\gamma})^m}, \tag{3-10}$$

where m denotes the Cross law index. The Cross law is also capable of capturing the transition between the Newtonian plateau and the power-law region, while the curvature of the viscosity curve in the vicinity of the transition depicted by the cross law model is different from that yielded by applying the Carreau-Yasuda model. The differences of applying the above GNF models can be seen from an example of numerical fitted data obtained by applying the above models appearing in Figure 3-1. Other GNF models such as the Bingham law model and the Herschel-Bulkley law are not given explicitly in the thesis as these models are more suitable for concrete and mud rather than the polymer materials. More information for the GNF models can be found in [72, 73].Note that the shear viscosity property of a polymeric fluid is sensitive to thermal effects, such that, for example, the consistency index K will vary due to a thermal gradient. However, as an

isothermal assumption is made at the beginning of this section, we do not include the thermal effects on the GNF models and readers of interest are referred to [72, 73] for further information.

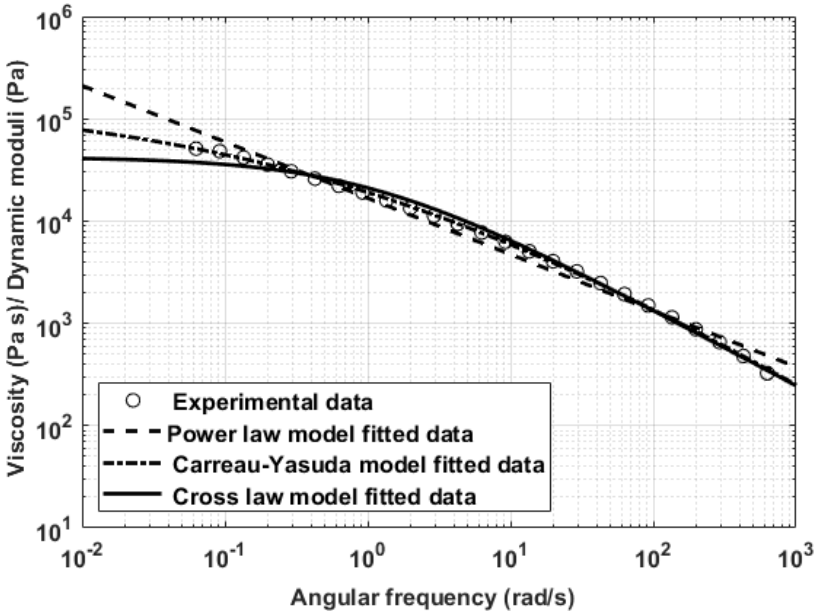

Figure 3-1. Fitting the shear viscosity data of neat ABS polymer measured at 210 ℃ with different GNF models. Note, the Cox-Merz rule is applied to transfer the complex viscosity data measured from the rotational rheometer to the shear viscosity.

3.2 Governing Equations for Fiber Orientation Kinetics

Flow-induced fiber orientation is a key element connecting the processing condition of a polymer processing approach and the material performances of a processed composite material. In general, the dynamic kinetics of particle orientation are considered as a result of the flow fields of the underlying suspension. The direction of a single rigid fiber within a polymer matrix is commonly described by a unit vector $\boldsymbol{p}(\varphi, \phi)$, as shown in Figure 3-2, with coordinates [22, 47]

$$\boldsymbol{p}(\varphi, \phi) = \begin{Bmatrix} sin\varphi cos\phi \\ sin\varphi sin\phi \\ cos\varphi \end{Bmatrix}, \tag{3-11}$$

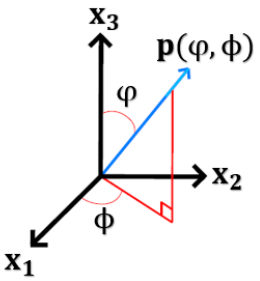

Figure 3-2. Coordinates of the Vector $\boldsymbol{p}(\varphi, \phi)$ Defining by the Angles φ and ϕ.

3.2.1 Jeffery's Theory

Numerous common fiber orientation analysis theories are evolved out of the foundational work of Jeffery back to the early 1920's, in which Jeffery first evaluated the fiber orientation of a single ellipsoidal particle in an incompressible simple shear viscous flow as [75]

$$\frac{D\boldsymbol{p}}{Dt} = \dot{\boldsymbol{p}} = \boldsymbol{W} \cdot \boldsymbol{p} + \lambda_{a_r}(\boldsymbol{D} \cdot \boldsymbol{p} - \boldsymbol{D}:\boldsymbol{ppp}), \tag{3-12}$$

Here, $\dot{\boldsymbol{p}}$ is defined as the time derivative of the hydraulic component of rotational motion of the ellipsoid, and t refers the time. $\boldsymbol{W}$ and $\boldsymbol{D}$ are the vorticity and rate-of-deformation tensors which are written as a function of the velocity gradient fields of the flow. In addition, the fiber geometric factor λ_{a_r} depends on the fiber geometry such that

$$\lambda_{a_r} = ({a_r}^2 - 1)/({a_r}^2 + 1), \tag{3-13}$$

and a_r refers to the aspect ratio of an ellipsoidal fiber. Jeffery's equation proposed that an ellipsoid will experience periodic motion in a shearing flow [75]. When Jeffery's equation is applied to characterizing the fiber suspension kinematics, fiber-fiber and fiber-boundary interactions are neglected.

3.2.2 Folgar-Tucker Model

Folgar and Tucker extended Jeffery's theory to evaluate the orientation of multiple fibers using a fiber orientation probability density function $\psi(\boldsymbol{p})$ which quantifies the rate of change in $\psi(\boldsymbol{p})$ as [23]

$$\frac{D\psi}{Dt} = -\nabla \boldsymbol{p} \cdot \left[\psi(\boldsymbol{p})\left(\frac{D\boldsymbol{p}}{Dt}\right) - D_r \nabla \boldsymbol{p}\psi(\boldsymbol{p})\right], \tag{3-14}$$

Here, D_r refers to the rotary diffusion term that captures the fiber-fiber interaction effects depending upon the suspended flow kinematics. Folgar and Tucker [23] defined $D_r = C_I\dot{\gamma}$, where $\dot{\gamma}$ is the scalar magnitude of the rate-of-deformation tensor $\boldsymbol{D}$ and C_I is the empirically fitted coefficient that characterizes the intensity of fiber-fiber interaction. Unfortunately, the proposed theory as casted by Folgar and Tucker is computationally prohibitive for flow problems such as those in LAAM polymer depositions [19]. Thus, a more efficient method is in demand for our proposed research.

3.2.3 Advani-Tucker Tensor Approach

Advani and Tucker re-casted the Folgar-Tucker model and proposed a fiber orientation evaluation equation based on moment tensors of $\psi(\boldsymbol{p})$ to efficiently describe the statistical orientation behaviors in concentrated fiber suspensions as [22]

$$\frac{D\boldsymbol{A}}{Dt} = (\boldsymbol{A}\cdot\boldsymbol{W} - \boldsymbol{W}\cdot\boldsymbol{A}) + \lambda_{a_r}(\boldsymbol{D}\cdot\boldsymbol{A} + \boldsymbol{A}\cdot\boldsymbol{D} - 2\mathbb{A}\!:\!\boldsymbol{D}) + C_I\dot{\gamma}(2\boldsymbol{I} - 6\boldsymbol{A}), \tag{3-15}$$

where

$$\boldsymbol{A} = \oint_{\mathbb{S}} \boldsymbol{pp}\psi(\boldsymbol{p})d\boldsymbol{p} \text{ and } \mathbb{A} = \oint_{\mathbb{S}} \boldsymbol{pppp}\psi(\boldsymbol{p})d\boldsymbol{p}, \tag{3-16}$$

are the second and fourth order orientation tensors. The term $C_I\dot{\gamma}(2\boldsymbol{I} - 6\boldsymbol{A})$ refers to the Isotropic Rotary Diffusion (IRD) term that is first proposed in [23]. This method enables

an efficient computation for concentrated fiber suspensions such as the fiber-filled polymers that are commonly applied in LAAM fabrications [19].

3.2.4 Reduced Strain Closure Model

More recently, experimental works revealed that the fiber orientation kinetics evolved in a slower rate as compared to predictions yielded by the Folgar-Tucker model. Wang, et al. provided the Reduced Strain Closure (RSC) model based on the IRD model of Folgar and Tucker, which is able to count the experimentally observed slow-kinetics of fiber orientation in shear flow applications, such that [56]

$$\frac{D\boldsymbol{A}}{Dt} = (\boldsymbol{A}\cdot\boldsymbol{W} - \boldsymbol{W}\cdot\boldsymbol{A}) + \lambda_{a_r}(\boldsymbol{D}\cdot\boldsymbol{A} + \boldsymbol{A}\cdot\boldsymbol{D} - 2\mathbb{R}\!:\!\boldsymbol{D}) + \kappa C_I\dot{\gamma}(2\boldsymbol{I} - 6\boldsymbol{A}), \tag{3-17}$$

and

$$\mathbb{R} = [\mathbb{A} + (1-\kappa)(\mathbb{L} - \mathbb{M}\!:\!\mathbb{A})], \tag{3-18}$$

where $\mathbb{L} = L_{ijkl} = \sum_{m=1}^{3}\lambda_m n_i^m n_j^m n_k^m n_l^m$, $\mathbb{M} = M_{ijkl} = \sum_{m=1}^{3} n_i^m n_j^m n_k^m n_l^m$, and λ_m refers to the m-th eigenvalue of $\boldsymbol{A}$, and n_i^m is the i-th component of the m-th eigenvector associated with second order orientation tensor. In the above, κ serves as a strain reduction factor limiting the growth rate of fiber alignment, by which the growth rates of eigenvalues of the second-order orientation tensors are reduced while the rotation rate of the eigenvectors remains unchanged. Note, κ is a scalar between zero and one.

3.2.5 Anisotropic Rotary Diffusion Models

Regarding to the un-satisfied matching between the experimental orientation measurements and existing orientation models (e.g., Advani-Tucker tensor approach with Folgar-Tucker IRD model [22], RSC model[56]) for polymer materials reinforced with

long discontinuous fibers, Phelps and Tucker proposed an Anisotropic Rotary Diffusion (ARD) model as [76]

$$\frac{D\boldsymbol{A}}{Dt} = (\boldsymbol{A}\cdot\boldsymbol{W} - \boldsymbol{W}\cdot\boldsymbol{A}) + \lambda_{a_r}(\boldsymbol{D}\cdot\boldsymbol{A} + \boldsymbol{A}\cdot\boldsymbol{D} - 2\mathbb{A}\vdots\boldsymbol{D}) + D_r^{ARD}, \tag{3-19}$$

and

$$D_r^{ARD} = \dot{\gamma}(2\boldsymbol{C} - 2[tr(\boldsymbol{C})]\boldsymbol{A} - 5(\boldsymbol{D}\cdot\boldsymbol{C} + \boldsymbol{C}\cdot\boldsymbol{D}) + 10\mathbb{A}\vdots\boldsymbol{C}), \tag{3-20}$$

where $\boldsymbol{C}$ is a rotary diffusion tensor that controls the spatial directionality of any diffusive flux. Every objective ARD model is dependent on the choice of $\boldsymbol{C}$. Specifically, Phelps and Tucker proposed the format of $\boldsymbol{C}$ as [76]

$$\boldsymbol{C} = b_1\boldsymbol{I} + b_2\boldsymbol{A} + b_3\boldsymbol{A}^2 + \frac{b_4}{\dot{\gamma}}\boldsymbol{D} + \frac{b_5}{(\dot{\gamma})^2}\boldsymbol{D}^2, \tag{3-21}$$

Here, b_i are five constant coefficients that are fitted based on a desired steady-state orientation in simple shear flow [76, 77]. In addition, different forms of the $\boldsymbol{C}$ tensor are presented by Tseng, et al. [78, 79], and Bakharev, et al. [80], and Wang, et al. [80]. These advanced ARD models improve the robustness of the ARD-type orientation model [80].

3.3 Fully Coupled Fiber Suspension Theory

The computationally efficient weakly coupled flow-induced fiber orientation analysis experiences widespread implementations in polymer processing studies (e.g., [19, 70, 71]), where the effect of the fiber presence is ignored in the flow computation and the fiber orientation within the fiber suspension is then determined by the uncoupled flow fields. This approach has been proved in shear dominant narrow gap flows applications such as injection and compression modelling processes [70, 71]. In contrast, Evans, et al. [81] and Lipscomb, et al. [82] considered a fully coupled approach where the motion of suspended fibers depends on the flow field, and the fiber orientation

influences flow kinematics, typically through the suspension melt viscosity. In particular, the traction of the surface of the reinforced fiber is counted to evaluate the particle contribution of the stress field of the overall suspension flow, in an averaged sense, such that [83]

$$\boldsymbol{\tau} = 2\eta\boldsymbol{D} + 2\eta v_{frac}[a\boldsymbol{D}:\mathbb{A} + b(\boldsymbol{D}\cdot\boldsymbol{A} + \boldsymbol{A}\cdot\boldsymbol{D}) + c\boldsymbol{D} + f\boldsymbol{A}D_r], \tag{3-22}$$

where $\boldsymbol{\tau}$ refers the stress tensor, η denotes the viscosity of the solvent. In the above equation, $\boldsymbol{A}$ and $\mathbb{A}$ are the second and fourth order fiber orientation tensors appearing in Equation 3-16, respectively, and v_{frac} refers to the volume fraction of the filler. D_r is the rotary diffusion due to Brownian motion, and a, b, c and f are the four geometrical shape factors associated with the fiber fillers. Lipscomb, et al. [82] proposed an expression for the materials constants a, b, c and f, such that

$$a = a_r/\{2[\ln(2a_r) - 1.5]\}, \tag{3-23}$$

and

$$b = 6\ln(2a_r) - 11\ /(a_r)^2, \tag{3-24}$$

and

$$c = 2, \tag{3-25}$$

and

$$f = 3(a_r)^2/[\ln(2a_r) - 0.5], \tag{3-26}$$

The above equations yield an error of ~15% at $a_r = 10$ and less than 1% for $a_r = 50$, as compared with the corresponding experimental measurements [83].

Dinh and Armstrong [84] proposed a constitutive equation based on the slender-body theory, which ultimately yields a similar format as appearing Equation 3-22, except that the expression for the shape factors varies. As slender-body theory assumes trivial

particle thickness which leads the constants b and c being equal to zero. In addition, the Brownian motion of relatively large particles (e.g., size of fillers in typical short fiber filled thermoplastics) is negligible and thus the constant f and its associated term can also be ignored. Eventually, we can recast Equation 3-22 as

$$\boldsymbol{\tau} = 2\eta \boldsymbol{D} + 2\eta N_p \boldsymbol{D} : \mathbb{A}, \tag{3-27}$$

where N_p stands for the particle number that describe the intensity of the fiber effect on viscosity, which can be evaluated by

$$N_p = a v_{frac}, \tag{3-28}$$

and

$$a = \frac{(a_r)^2}{3\ln\left(\frac{2h_f}{D_f}\right)}, \tag{3-29}$$

where D_f is the diameter of a fiber and h_f refers to a characteristic distance between a fiber and its nearest neighbors, which can be expressed as

$$2h_f/D_f = \sqrt{\pi/v_{frac}}, \text{ for aligned fibers} \tag{3-30}$$

and

$$2h_f/D_f = \pi/(2v_{frac}a_r), \text{ for random fibers} \tag{3-31}$$

Notice that h_f is a factor depending on the fiber volume fraction, and thus the contribution of the fiber filler to the stress field is no longer proportional to the volume fraction as appearing in Equation 3-22 [83]. A significant benefit of applying the slender-body theory is that the hydrodynamic interactions between reinforced fibers can be incorporated, in an averaged sense, so that estimations beyond the dilute regime can be considered [83]. This is pivotal in the analysis of the polymer composites of interest for LAAM applications, where most filled polymers involved are beyond the dilute regime.

We note that, in the case of non-Newtonian fluid flow models applied, the computation of the viscosity as well as the stress field will become more complex. To our best knowledge, flow-fiber coupling effect has been quantified in a Newtonian fluid flow (e.g., [53, 85]), while that of the viscoelastic fluid has not been seen. This is an interesting yet challenging field for researchers to explore.

3.4 Orientation Homogenization Approach

It is important to quantify the effect of suspended fibers and fiber orientation on elastic properties within the extruded bead of the LAAM process. The development of micromechanics models provides analytical approximations for the stiffness tensor components of a unidirectional aligned fiber reinforced polymer (see e.g., [20,39-41]). These unidirectional models serve as a basis for orientation homogenization methods (see e.g., Advani and Tucker [19] and Jack and Smith [21]) that yield orientation averaged elastic properties for a short fiber polymer composite. The local orientation average stiffness tensor $\tilde{C}_{ijkl}$ may be written as [19]

$$\begin{aligned}\tilde{C}_{ijkl} = M_1 A_{ijkl} + M_2\left(A_{ij}\delta_{kl} + A_{kl}\delta_{ij}\right) + M_3\left(A_{ik}\delta_{jl} + A_{il}\delta_{jk} + A_{jl}\delta_{ik} + \right.\\ \left. A_{jk}\delta_{il}\right) + M_4 A_{ij}\delta_{kl} + M_5\left(A_{ik}\delta_{jl} + A_{il}\delta_{jk}\right),\end{aligned} \tag{3-32}$$

where material constants M_I, $I = 1,\ldots,5$ are computed from

$$M_I = \begin{Bmatrix} C_{11} + C_{22} - 2C_{12} - 4C_{66}, & \text{for } I = 1 \\ C_{12} - C_{23}, & \text{for } I = 2 \\ C_{66} + (C_{23} - C_{22})/2, & \text{for } I = 3 \\ C_{23}, & \text{for } I = 4 \\ (C_{22} - C_{23})/2, & \text{for } I = 5 \end{Bmatrix}, \tag{3-33}$$

In the above, δ_{ij} is the Kronecker delta [42], and the A_{ij} are orientation tensor components solved previously. It is common to compute the A_{ijkl} through some type of

closure approximation (e.g., [86]). The C_{ij} appearing in Equation 3-33 are components of the stiffness tensor for the associated unidirectional fiber filled composite written in contracted notation, which we compute using the Tandon-Weng micromechanics model [87] (cf. Appendix A for the Tandon-Weng equation [87]). It is shown by Tucker and Liang [88], as well as other researchers (e.g., [89]), that the Tandon-Weng equation yields one of the most accurate estimates for elastic properties over the range of fiber aspect ratios found in the short fiber composites.

CHAPTER FOUR

Effects of Polymer Rheology Modeling on Melt Extrusion

This chapter has been published as part of the citation [47]: Wang, Zhaogui, and Douglas Smith. "Rheology effects on predicted fiber orientation and elastic properties in large scale polymer composite additive manufacturing." *Journal of Composites Science 2.1 (2018): 10.*

Rheological properties of the polymeric melt greatly determine the flow field of the molten composite feedstock in LAAM extrusion and deposition, which ultimately affect the fiber alignment within the solidified extrudate. In addition, the extrudate swell of the melt determined by the polymer rheology also contributes to the resolution of a printed structure, especially in the manufacturing of large parts. This chapter considers the effect that various rheological fluid models have on the melt flow extrudate swell, kinematics and resulting flow-induced fiber orientation state. The material models considered in this section are virgin ABS polymer and 13% CF-ABS, supplied by PolyOne Corporation (Avon Lake, OH, USA).

4.1 Flow Domain Modeling

The geometry of the flow domain in our study is based on the large-scale AM Strangpresse Model-19 single screw extruder nozzle appearing in Figure 4-1. In addition to the nozzle orifice, we include an 1-inch section of free extrudate beyond the nozzle exit in the simulation to capture die swell. The length of the free extrudate is much higher than that of the deposition distance (i.e., distance between nozzle tip and substrate), and thus this length of free extrudate guarantees the flow reaches near steady state. Due to the

axisymmetry of the nozzle geometry and assumed flow, we simplify the flow domain to a 2D axisymmetric model, which saves significant computational expense. Furthermore, our axisymmetric assumption ignores any swirling motion in the flow that may result from the extruder screw. Since only a short section of the free extrudate material is considered, gravitational effects are ignored, which results in the body force $\boldsymbol{f}$ in Equation 3-2 being zero as well.

The boundary conditions of the flow domain appear in Figure 4-2, in which

- $\boldsymbol{\Gamma_1}$: Flow domain inlet, where the prescribed volumetric flow rate Q is specified. Also, a fully developed velocity profile is computed and imposed at the inlet by ANSYS-Polyflow based on Q and the selected rheology model.
- $\boldsymbol{\Gamma_2}$ and $\boldsymbol{\Gamma_4}$: No slip wall boundary, where $v_s = v_n = 0$.
- $\boldsymbol{\Gamma_3}$: Axis of symmetry, where $F_s = v_n = 0$.
- $\boldsymbol{\Gamma_5}$: Free surface, where $\mathbf{v} \cdot \vec{\boldsymbol{n}} = 0$.
- $\boldsymbol{\Gamma_6}$: Flow domain exit, where $F_n = v_s = 0$.

In the above, F_s is the tangential force, F_n is the normal force, v_s is the tangential velocity, v_n is the normal velocity, $\boldsymbol{v}$ is the velocity vector at the free surface, and $\vec{\boldsymbol{n}}$ is a unit vector normal to the free surface [21]. The die swell of the free surface is computed using the methods of spines in ANSYS-Polyflow, which is an efficient remeshing rule often applied to 2D free surface problem [74].

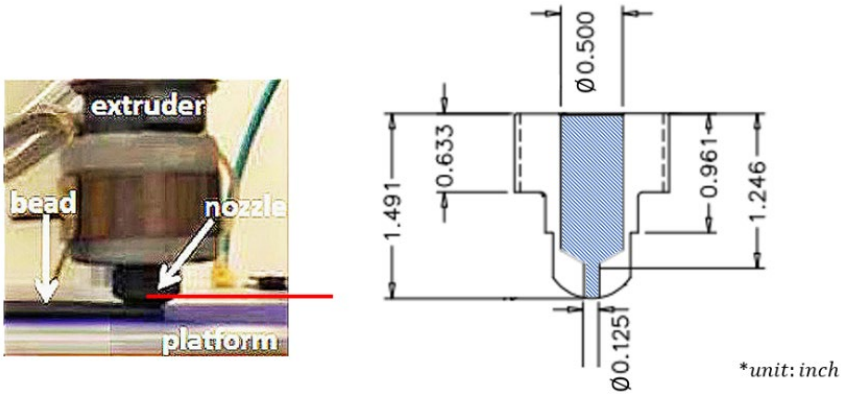

Figure 4-1. Geometric Dimensions of a Strangpresse Model-19 Extruder Nozzle.

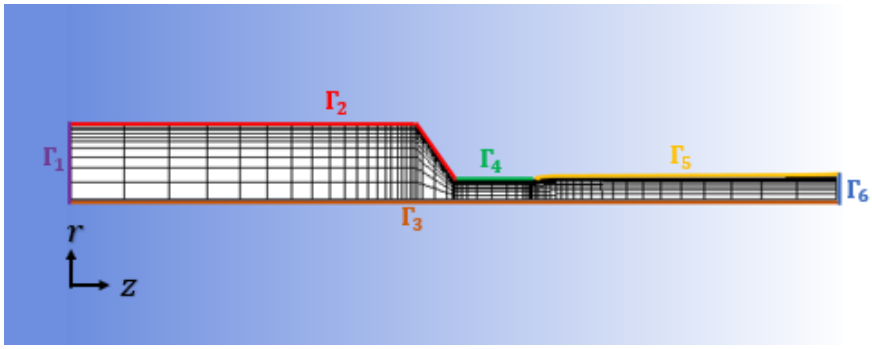

Figure 4-2. Mesh and boundary condition of the flow domain. Note, the flow domain is shifted 90° as compared to the layout appearing in Figure 4-1.

4.1.1 Flow Kinematics Computation

For the numerical study presented in this chapter, a weakly coupled scheme is adapted in characterizing the melt flow and the associated flow-induced fiber orientation in the fiber reinforced composite such that the flow fields are solved first neglecting the effects of fiber alignment within the melt flow and then the fiber orientation state is computed based on the resulting flow kinematics. We use ANSYS-Polyflow [24] to evaluate the flow kinematics in the polymer melt flow domain based on conservation of momentum and conservation of mass as appearing in Equations 3-1 and 3-2, where an isothermal and incompressible Stokes flow is assumed to represent the melt flow. Note that the simplified flow solutions neglect thermal effects, time-dependent effects and

inertia effects that are usually considered as trivial contributors in related simulations [19, 55, 69]. Specifically, non-isothermal effects such as temperature gradients within the free extrudate or viscous heating in the melt flow may result in nonuniform melt rheology. These effects are commonly captured through temperature dependent properties such as K in the power law model (c.f. Equation 3-8), which is often addressed with an Arrhenius-type temperature dependency (e.g., the Williams–Landel–Ferry equation) [73]. Consequently, the isothermal assumption employed here may yield some inaccuracy in the predicted numerical data. However, it is expected, as suggested by others (e.g., [19, 55, 69]), that any temperature-related variation in the rheology properties would be small and not have a significant effect on the results presented below.

4.1.2 Viscoelastic Fluid Model

Flow rheological phenomena exhibited by polymeric fluid flows beyond the range of validity of the Newtonian or GNF models. Among these are the presence of intense normal stresses in viscometric flows, high resistance to extensional deformation, and the memory effects related to the elastic component of the fluid. Viscoelastic fluid models are designed for characterizing the complex rheology of these non-Newtonian fluids such as the molten polymer flows.

The constitutive equation of the shear stress tensor $\boldsymbol{\tau}$ for viscoelastic fluids is different as compared to a purely viscous fluid (cf. Equation 3-4)

$$\boldsymbol{\tau} = \boldsymbol{\tau_1} + \boldsymbol{\tau_2}, \tag{4-1}$$

and the viscosity of the viscoelastic polymeric fluids can be written as

$$\eta = \eta_1 + \eta_2, \tag{4-2}$$

In the above, $\boldsymbol{\tau_1}$ and η_1 correspond to the viscous component of the fluid, and $\boldsymbol{\tau_2}$ and η_2 are the contributions from the non-viscous component of the viscoelastic fluid [73].

The linear Maxwell model is one of the simplest viscoelastic fluid models, which can be written as [73]

$$\boldsymbol{\tau_2} + \lambda^r \frac{D\boldsymbol{\tau_2}}{Dt} = 2\eta_2 \boldsymbol{D}, \tag{4-3}$$

where λ^r refers to the relaxation time of the fluid. In the Maxwell model, the viscous parts of $\boldsymbol{\tau}$ equates zero.

Furthermore, nonlinear forms of the viscoelastic fluid model may be more capable for advanced characterizations. Among those the Oldroyd-B model is one of the simplest which can be written as [73]

$$\boldsymbol{\tau_2} + \lambda^r \left(\frac{D\boldsymbol{\tau_2}}{Dt} + \overset{\backsim}{\boldsymbol{\tau_2}}\right) = 2\eta_2 \boldsymbol{D}, \tag{4-4}$$

and the viscous parts of $\boldsymbol{\tau}$ and η are evaluated in a regular manner as introduced above. $\overset{\backsim}{\boldsymbol{\tau_2}}$ appearing in Equation 4-4 is known as the upper convective derivative operator which can be written as

$$\overset{\backsim}{\boldsymbol{\tau_2}} = (\boldsymbol{v} \cdot \nabla)\boldsymbol{\tau_2} - (\nabla \boldsymbol{v})\boldsymbol{\tau_2} - \boldsymbol{\tau_2}(\nabla \boldsymbol{v})^T, \tag{4-5}$$

The Oldroyd-B Model behaves better than the Maxwell model, especially for the simulation of the polymer melt exhibiting very high elongational viscosity. However, the Oldroyd-B Model describes the stress field of the fluid with a linear constitutive equation which is not often the case for polymeric materials.

The limitation of the Oldroyd-B model motivates further derivations for the more advanced Giesekus model, which can be written as [73]

$$(\boldsymbol{I} + \frac{\alpha_G \lambda^r}{\eta_2}\boldsymbol{\tau_2}) \cdot \boldsymbol{\tau_2} + \lambda^r \overset{\backsim}{\boldsymbol{\tau_2}} = 2\eta_2 \boldsymbol{D}, \tag{4-6}$$

where α_G is a material constant and a non-zero value of α_G yields a bounded steady elongational viscosity and a shear-rate dependent shear viscosity. The Giesekus model is one of the most realistic differential viscoelastic models that yields rheological behaviors of shear thinning and non-quadratic first normal-stress difference at high shear rates.

In addition, the widely-used Phan-Thien-Tanner (PTT) model exhibits similar rheological features as the Giesekus model did, which can be written as [73]

$$e^{\left[\frac{\varepsilon_{PT}\lambda^r}{\eta_2}tr(\boldsymbol{\tau_2})\right]}\boldsymbol{\tau_2} + \lambda^r[\left(1 - \frac{\xi_{PT}}{2}\right)\overset{\sim}{\boldsymbol{\tau_2}} + \frac{\xi_{PT}}{2}\widehat{\boldsymbol{\tau_2}}] = 2\eta_2\boldsymbol{D}, \tag{4-7}$$

and $\widehat{\boldsymbol{\tau_2}}$ is the lower convective derivative operator as

$$\widehat{\boldsymbol{\tau_2}} = (\boldsymbol{v}\cdot\nabla)\boldsymbol{\tau_2} + (\nabla\boldsymbol{v})^T\boldsymbol{\tau_2} + (\nabla\boldsymbol{v}), \tag{4-8}$$

Note, Equation 4-7 is also referred as the exponential form of the PTT model. In the above, ε_{PT} and ξ_{PT} are two material constants that are used to separately control the shear and elongational behaviors. Particularly, a non-zero value of ε_{PT} leads to a bounded steady elongational viscosity. It is important to note that the viscoelastic fluid models introduced above can have single relaxation time or multiple relaxation time constants in which case the non-viscous stress tensor $\boldsymbol{\tau_2}$ represents the sum of all viscoelastic contributions from sub-modes at each of the relaxation times [73, 74].

Herein, the advanced PTT model is employed in the flow rheology modeling. Nevertheless, viscoelastic models are not limited to the discussed examples. An exhausted review on the viscoelastic fluid rheology models can be found in [90] and will not be included in the dissertation for conciseness.

Alternatively, ANSYS-Polyflow includes the Simplified Viscoelastic (SV) model that reduces computational expense when predicting die swell in viscoelastic flows. In the SV formulation, it is understood that extrudate swell in polymer extrusion is

associated with the first normal stress difference in the fluid. Hence, the SV model extends the Generalized Newtonian Fluid (GNF) model, where the total stress tensor is given as [74]

$$\boldsymbol{\tau_2} = \begin{bmatrix} \Psi_s \mu(\dot{\chi})\dot{\chi} & \eta(\dot{\gamma})\dot{\gamma} & 0 \\ \eta(\dot{\gamma})\dot{\gamma} & 0 & 0 \\ 0 & 0 & 0 \end{bmatrix}, \tag{4-9}$$

where the off-diagonal terms given as $\eta(\dot{\gamma})\dot{\gamma}$ are the shear stress components. In this form, $\eta(\dot{\gamma})$ is expressed by a typical generalized Newtonian model, and $\dot{\gamma}$ is the magnitude of the strain rate tensor $\boldsymbol{D}$. In the above, $\Psi_s \mu(\dot{\chi})\dot{\chi}$ represents the first normal stress component, in which $\mu(\dot{\chi})$ is described in a similar fashion as is done for the shear strain rate. In Equation 4-9, $\dot{\chi}$ is the specialized viscoelastic variable, which is evaluated with the transport equation

$$\theta_s(\dot{\gamma})\frac{D\dot{\chi}}{Dt} + \dot{\chi} = \dot{\gamma}, \tag{4-10}$$

where $\theta_s(\dot{\gamma})$ is the relaxation time of the melt which controls the development of the extrudate swell diameter once the melt flow exits the nozzle. In addition, Ψ_s appearing in Equation 4-9 is an artificial weighting factor, which controls the swelling enhancement versus the input flow rate [74].

4.2 Material Rheology

To obtain data needed for the melt rheology models considered here, we conduct the rheometry characterization of our filled and unfilled ABS through a HAAKE MARS 40 rheometer (Thermo Fisher Scientific, Waltham, MA, USA), where the complex shear viscosity and the dynamic shear moduli of the molten material are obtained. The measured data are fitted with both purely viscous and viscoelastic rheology models as described below, through the assistance of commercial code ANSYS Polymat [91].

4.2.1 Rheometry Data Acquisition

The rheological properties, including the complex shear viscosity, storage shear modulus and loss shear modulus, are measured for virgin ABS polymer using the MARS 40 rheometer (cf. Figure 4-3). The test temperature of 210 ℃ is selected since it is typical of the LAAM nozzle temperature when manufacturing ABS through LAAM applications. An isothermal frequency sweep measurement is conducted, where the applied strain of the test is fixed at 0.01%, which is within the linear viscoelastic region of the tested polymer. The angular frequency of the test is set between 0.0628 to 628 rad/s, which covers the typical range that a polymer melt would experience in the LAAM processes [92]. Data obtained through the custom frequency test appears in Figure 4-4.

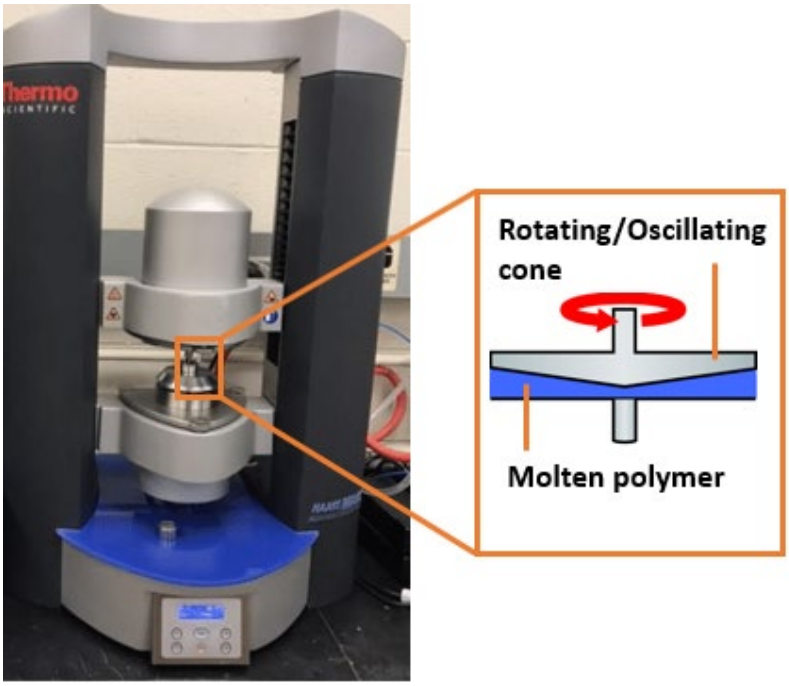

Figure 4-3. Rheometry Measurement Undertaken through HAAKE MARS 40 Rheometer.

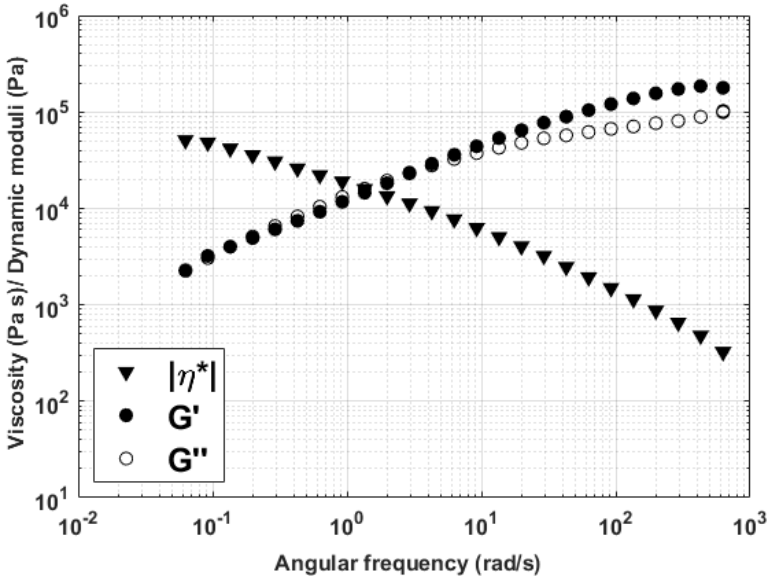

Figure 4-4. Rheological Properties Measured through Frequency Sweep Test.

4.2.2 Rheometry Data Curve Fitting

Experimental viscosity data shown in Figure 4-4 exhibit obvious shear thinning behavior as expected for ABS (i.e., the shear viscosity of the molten polymer reduces with increased shear rate). In this study, we acknowledge the effectiveness of the Cox-Merz rule, where the shear viscosity is the magnitude of the complex viscosity as [73]

$$\eta(\dot{\gamma}) = |\eta^*(\omega)| = \frac{\sqrt{(G')^2+(G'')^2}}{\omega}, \text{ for } \dot{\gamma} = \omega \tag{4-11}$$

where η and η^* denote, respectively, the shear viscosity and the complex viscosity of the polymer melt. In Equation 4-11, G' and G'' refer to the storage and loss shear moduli, respectively, and ω and $\dot{\gamma}$ are angular frequency and shear rate, respectively. Shear viscosity obtained using experimental data of G' and G''through Equation 4-11 is plotted against the measured magnitude of complex viscosity as shown in Figure 4-5, from where a good agreement is seen.

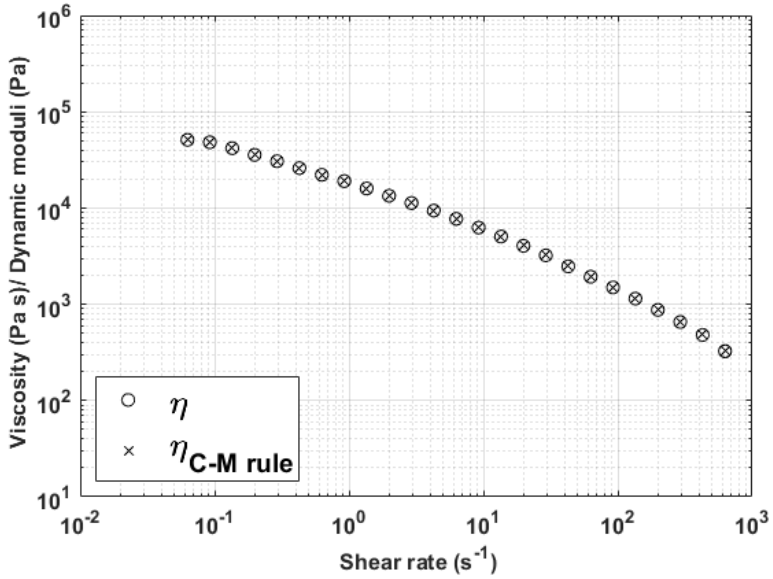

Figure 4-5. Curves of Shear Viscosity and Magnitude of Complex Viscosity as a Function of Shear rate. Note, Shear Viscosity η Data is Obtained from Measured data of G' and G''.

Shear viscosity of the ABS polymer shown above is also used to obtain parameters for a Newtonian fluid model, and Generalized Newtonian fluid (GNF) models including the Power law model and the Carreau-Yasuda model. The Carreau-Yasuda model characterizes the Newtonian plateau at low shear rates while the power law model does not. The governing equations of the models are given through Equations 3-7 to 3-9. Here, the fitting process is conducted in the commercial suite ANSYS Polymat (version 19.1, ANSYS, Inc., Canonsburg, PA, USA), which is a curve-fitting tool for non-Newtonian rheology models [91]. The fitting interval of shear rate is between 10^{-2} to 10^{3} s^{-1} which includes the angular frequency range used in the rheometer tests described above. Data generated from the fitted models are plotted against actual measurements in Figure 4-6. Fitted coefficients of the various rheology models appear in Table 4-1. Note that the constant shear viscosity of the Newtonian fluid model is estimated at a shear rate

of 100 s^{-1}, which is within the typical shear rate range that polymer melt experiences during the LAAM extrusion [92].

In addition, measured shear dynamic moduli are fitted with the differential viscoelastic fluid model, Phan-Thien-Tanner (PTT) model (cf. Equation 4-7), and the results are given in Figure 4-7. In this fitting process, the shear rate interval shares the same standard as that for the GNF models. The fitted coefficients of the PTT model appear in Table 4-2.

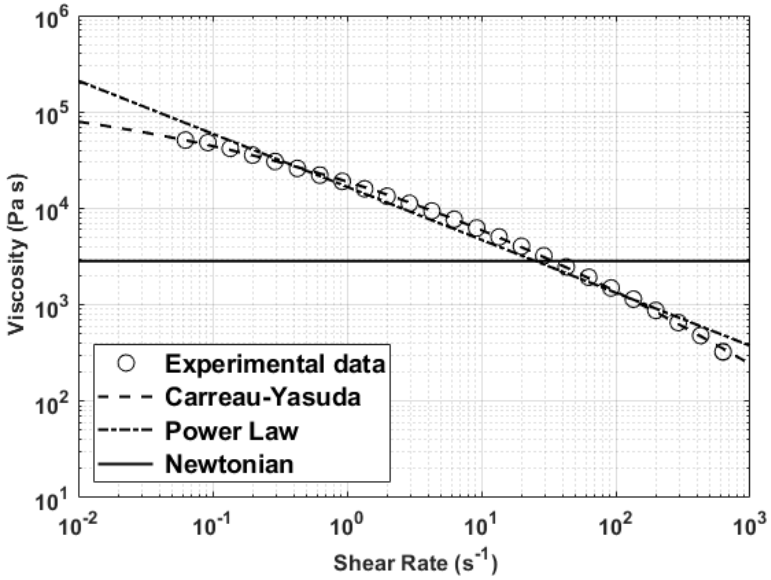

Figure 4-6. Shear Viscosity Curve Fitting using Generalized Newtonian Fluid Models.

Table 4-1. Fitted Coefficients of Applied Generalized Newtonian Fluid Models.

Rheology Model	η_o or K	η_∞	n	a	λ_c
Newtonian	3200	N/A	N/A	N/A	N/A
Power law	16761	N/A	0.4503	N/A	1
Carreau-Yasuda	204064	0	0.000001455	0.2398	0.3333

Note, units of η_o (and K) are $Pa \cdot s$, $Pa \cdot s^n$, $Pa \cdot s^{(n-1)/a}$ for Newtonian, power law and Carreau-Yasuda models. Unit of λ_c is s^{-1}, and the rest constants are unitless.

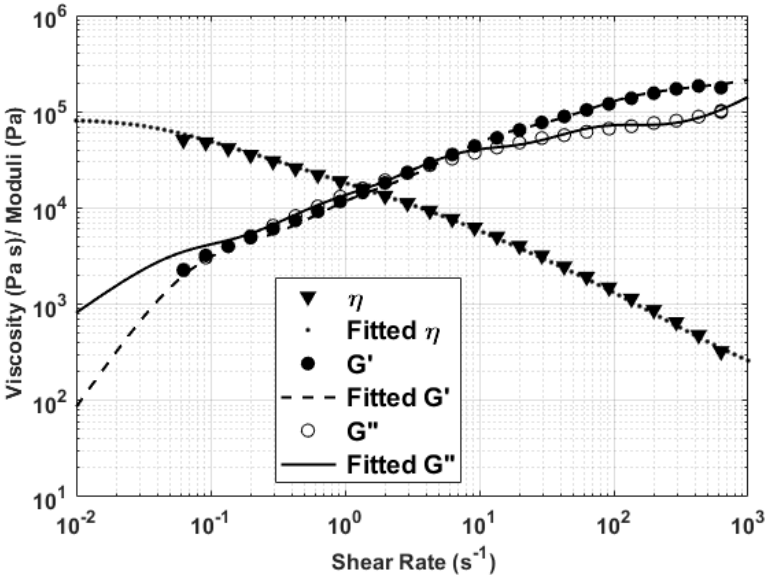

Figure 4-7. Curve Fitting the Experimental Rheology Data using the PTT Model.

Table 4-2. PTT Model Fitted Parameters for ABS Rheological Data.

Mode No. (i)	λ_i^r(s)	$\eta_{2_i}\,(Pa \cdot s)$
1	0.00022	131.7
2	0.0022	44.7
3	0.012	1180.8
4	0.12	6286.4
5	1.14	13065.7
6	13.82	61917.7

Note, ε_{PT} and ξ_{PT} (cf. Equation 4-7) are fitted as 0.75 and 0.18, respectively

The Simplified Viscoelastic (SV) model is an empirical construction defined in terms of θ_s and ψ_s (cf. Equation 4-9), each of which is typically defined to obtain a known flow domain property such as the die swell. As shown in Equation 4-9, the SV model requires a description of the shear viscosity which unfortunately cannot be the Power law model since it exhibits an unrealistic unbounded viscosity at a near-zero shear rate. Since our free surface predictions occur in a region with near-zero shear rates, we employ the fitted Carreau–Yasuda law (cf. Table 4-1) to represent the behavior of shear viscosity. It has been shown that defining an independent law for the normal stress

viscosity increases computational cost, but does not greatly enhance the accuracy of die swell calculation [74]. Therefore, we choose to use the same fitted Carreau–Yasuda model form as that for shear to describe the first normal stress viscosity term in the SV model employed here.

In our simulations, different sets of parameters θ_s and ψ_s are attempted and values are selected to provide a predicted die swell profile that is in good agreement with results obtained using the PTT viscoelastic fluid model, which is the most realistic rheology model considered in this chapter. Consequently, θ_s and ψ_s are thus defined as 0.26 and 0.47, respectively. And the predicted results are given in the following results section.

4.3 Fiber Orientation Modeling

Recently, fiber orientation measurements in injection molded plaques have showed that fiber alignment occurs slower than that simulated using traditional Advani-Tucker approach IRD model [19, 93]. In response, Wang, et al. [56] modified the Advani-Tucker orientation tensor evaluation equation (cf. Equation 3-15) by introducing a term that reduces the growth rate of fiber orientation owing to the strain effects. The resulting Wang-O'Gara-Tucker model is given through Equation 3-17. Upon comparing Equation 3-17 to Equation 3-15, the additional terms in the Wang-O'Gara-Tucker model of Equation 3-17 appear as a closure approximation, thus the model is also referred to as the Reduced Strain Closure (RSC) model, where κ is a slipping factor between zero to one that controlling the reduction of interaction between the fiber orientation and the flow strain fields. Note that when $\kappa = 1$, the RSC model in Equation 3-17 reduces to Advani-Tucker IRD model in Equation 3-15. In flow fields that promote changes in fiber

orientation, such as those found in LAAM nozzle flow, computation of $\boldsymbol{A}$ depends on the value of κ in the RSC model.

Selection of the RSC modeling parameters is required for its application into our nozzle flow problem. Wang, et al. [56] proved that the RSC model was effective in computing fiber orientation with C_I=0.01,and κ=0.1, for transient simple shear flows such as those seen in the injection molding process and some extrusion scenarios. Our computations assume the same values of the RSC parameters. It is noted that the imposed values of C_I and κ can potentially bring in some bias in the resulting predicted fiber orientation. But we expect that the parameter setting of the RSC model does not significantly affect our focus in this chapter, which is to show the variations of predicted outcomes (e.g., fiber orientation states of the flow domain, elastic properties of composite extrudates) by applying different rheological flow models. A corresponding experimental work may be needed in the future to further explore effective values for C_I and κ in predicting fiber orientation of the nozzle extrudate flow of a composite feedstock (e.g., 13% CF-ABS).

Under the weakly coupled formulation, we evaluate the tensors $\boldsymbol{W}$ and $\boldsymbol{D}$ in Equation 3-17 from velocity gradients computed along streamlines within the polymer melt flow field from our ANSYS-Polyflow simulation results. Once velocity gradients have been computed, we integrate the RSC equation (cf. Equation 3-17) over time along each streamline of the flow domain to compute second-order orientation tensors $\boldsymbol{A}$. Herein, the time scale is a time measurement recording a particle traveling along a streamline of the flow. The resulting provides computed orientation tensors values along flow streamlines.

A few clarifications are made as follows regarding the evaluation of the second-order orientation tensors (i.e., $\boldsymbol{A}$). Due to the normalization condition, the trace of $\boldsymbol{A}$ equates to unity. It can also be shown that A is symmetric, yielding just 5 independent components (see e.g., [22]). In addition, the constant λ_r appearing in Equation 3-17 depends on the fiber aspect ratio a_r (i.e., length to diameter ratio for a cylindrical fiber, which is the case considered in this study). We fix a_r = 40, which represents a typical value for the 13% CF-ABS composite material based on our measurements which shall be seen in Chapter Six. Consequently, λ_{a_r} is highly close to unity (cf. Equation 3-13) and we ultimately fix λ_{a_r} equates one as did in Wang, et al [56] (as well as other literature discussing the fiber orientation in shear dominate flows [53]). The fourth order fiber orientation tensor, $\mathbb{A}$ in Equation 3-16, is typically computed with a closure approximation in fiber orientation simulations [19, 53, 94]. Prior studies have focused on the natural–type closure [95] and the orthotropic-type closure [86]. In this dissertation, we employ the Orthotropic Closure (ORT) to compute components of $\mathbb{A}$ from A as defined in [86].

The assignment of the initial fiber orientation state at the nozzle inlet directly influences the fiber orientation throughout the flow domain. For example, the initial condition of the fiber orientation has been found to have an influence on predicted fiber orientation in injection molding processes by Meyer, et al. [96]. We assume the fiber orientation state prior to entering the nozzle has attained a fully developed steady state as the flow reaches the nozzle inlet. We note that the complexity in the melt flow in the LAAM extruder before the flow reaches the nozzle will indeed influence the fiber orientation state as the melt enters the nozzle. To better understand the effect of inlet fiber

orientation on computed outputs, we performed other simulations using a uniformly random fiber orientation at the nozzle inlet. It was found that using the alternate inlet fiber orientation condition had little effect on the trends in predicted extrudate fiber orientation and mechanical properties shown below. Therefore, in this work, the steady state fiber orientation tensor is obtained from an associated prior work [19].

4.4 Results and Discussion

Numerical data including the computed flow fields of the nozzle flow domain, die swell, and second-order orientation tensors along the flow streamlines and associated elastic properties of an extrudate composite are reported in this section.

4.4.1 Flow Fields and Extrudate Swell

Duty, et al. [92] showed that the typical wall shear rate in Big Area Additive Manufacturing systems is between 30 and 40 s^{-1}, and reaches a peak value near 100 s^{-1}at the nozzle exit. In our simulations, the average wall shear rate using the PTT model with material constants from Table 4-2 and an inlet flow rate of Q = 100 mm^3/s is calculated to be 36 s^{-1}, with a peak value of 87 s^{-1} at nozzle exit, which agrees well with the literature data [92]. Here, the average wall shear rate $\bar{\dot{\gamma}}_w$ is computed from the wall shear rate $\dot{\gamma}_w$ on $\mathbf{\Gamma_4}$ (cf. Figure 4-2) as

$$\bar{\dot{\gamma}}_w = \frac{1}{L_t}\int_{\mathbf{\Gamma_4}} \dot{\gamma}_w \; dz, \tag{4-12}$$

where L_t is the length of the nozzle exit tube defined by $\mathbf{\Gamma}_4$ in the z-direction.

Flow field contours within the LAAM nozzle are computed using Polyflow in this work, which also provides values of local shear rate, magnitude of velocity tensor, and flow streamlines which appear in Figure 4-8. Here, the flow domain is reflected about the

axis of symmetry for a visual aid of the full nozzle, while Polyflow only solves the axisymmetric plane as modeled above. It is seen that the magnitude of velocity tensor increases significantly one order of magnitude (e.g., ~0.002 m/s to ~0.02 m/s) as the flow exiting the convergence zone of the nozzle. Similarly, the shear rate within the flow exhibits significant change in the flow as it approaches the nozzle exit, where the shear rate near the fix-wall boundary is ~30 s^{-1}, which is much higher than the core of the flow (which is at ~ 3 s^{-1}).

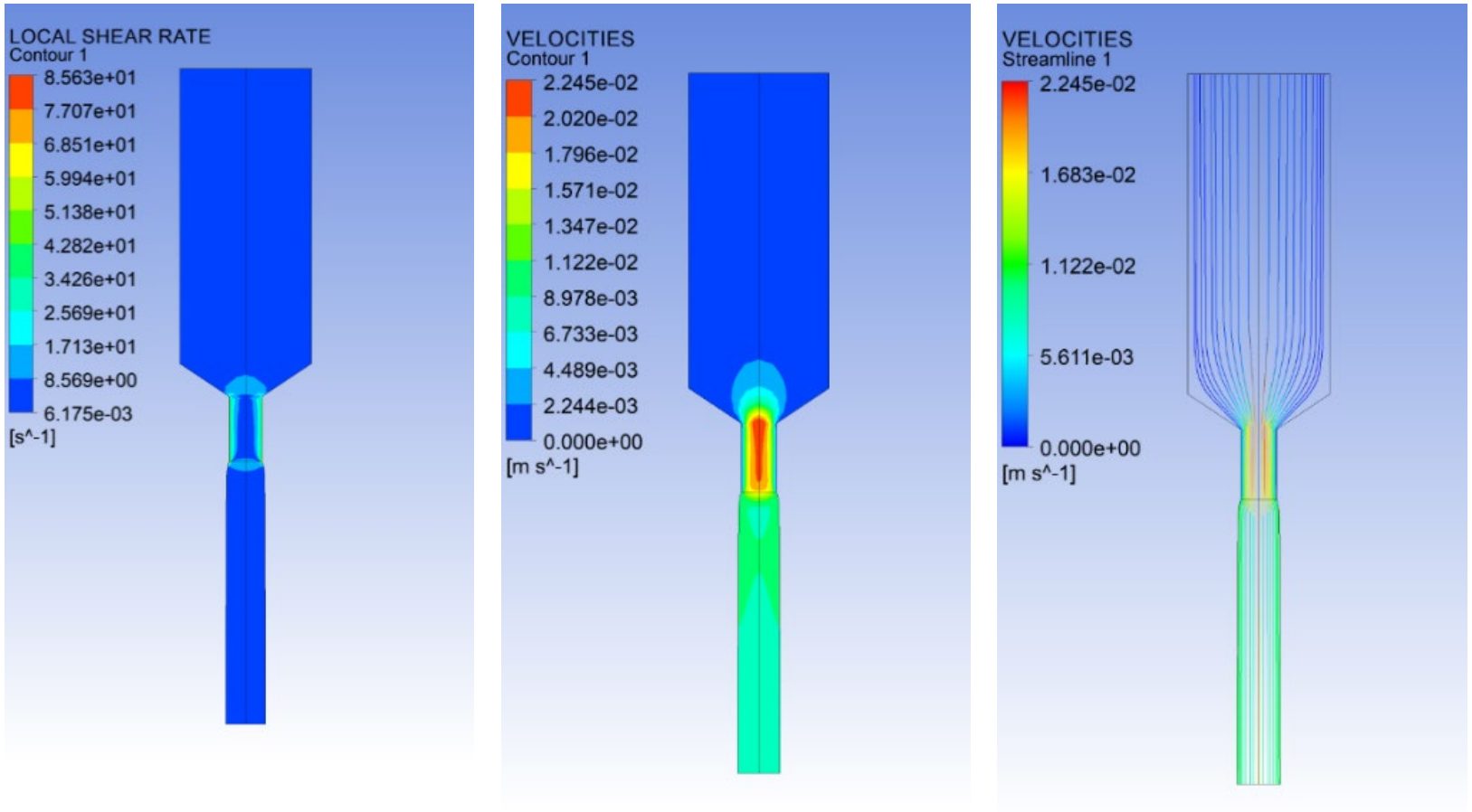

(A) (B) (C)

Figure 4-8. Computational Results of Flow Fields using the PTT model: (A) Local Shear Rate; (B) Magnitude of Velocity Vector; (C) Flow Streamlines.

Predicted die swell profiles for the flow appear Figure 4-9, where results are obtained using Newtonian, power law, Carreau-Yasuda, PTT and the SV models. The die swell just downstream of the nozzle exit is assessed using the apparent swell ratio B defined as [47]

$$B = \frac{d}{d_0}, \tag{4-13}$$

where d is the steady state swell flow diameter evaluated along the free surface downstream of the die exit (i.e., length of $\boldsymbol{\Gamma_6}$ appearing in Figure 4-2), and d_0 is the nozzle exit diameter. The computed data for B at the $\boldsymbol{\Gamma_6}$ surface is given in Table 4-3. The apparent die swell ratio B = 1.133 computed using the Newtonian fluid model agrees with the swell ratio of 1.13 predicted by Reddy and Tanner [97]. The steady state die swell ratios calculated using the Power law and Carreau-Yasuda rheology model are nearly identical and significantly lower than the swell ratio of B = 1.199 computed using the PTT model.

Moreover, the die swell profile obtained using the SV model converges to that computed with the PTT model as the flow reaches steady state. As shown in Table 4-4, simulation time using the SV model was 58 s which is similar to the GNF laws but much less than the 328 s when using the PTT model with the mesh given in Figure 4-7. Therefore, for a larger size of flow domain or a finer mesh quality, the SV model is a good alternative to qualitatively solve the flow problem with less computational cost.

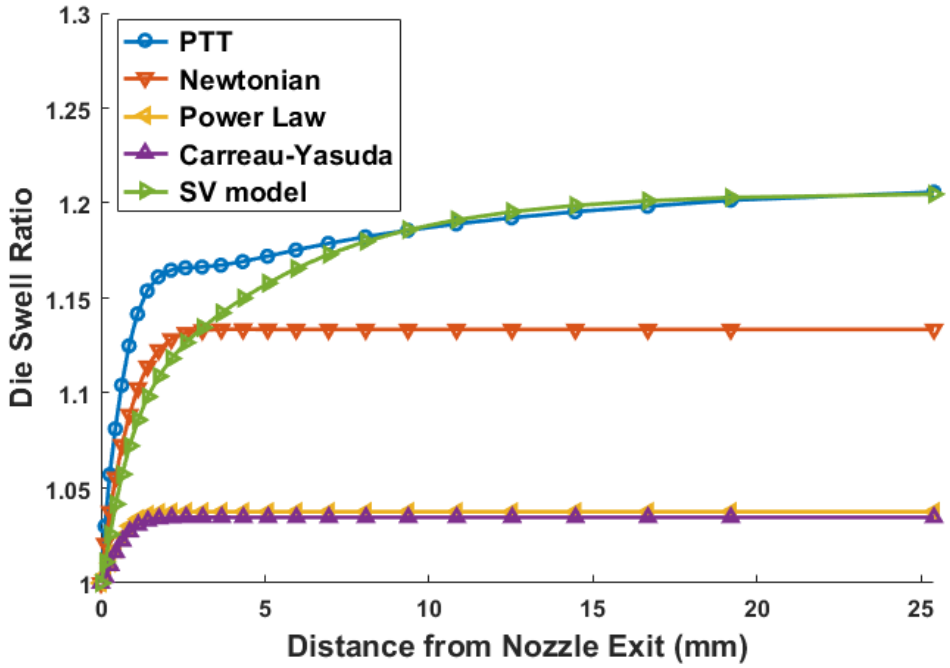

Figure 4-9. Die Swell Profiles Predicted by Using Different Rheology Models.

Table 4-3. Apparent Swell Ratio Values Resulted by Applied Rheology Models.

Model Name	*B*
Newtonian model	1.133
Power law model	1.037
Carreau-Yasuda model	1.035
PTT model	1.199
SV model	1.197

Table 4-4. CPU Time for Simulations with Applied Rheology Models.

Model Name	Simulation Time (s)
Newtonian model	30
Power law model	54
Carreau-Yasuda model	35
PTT model	328
SV model	58

4.4.2 Fiber Orientation Tensors

As described in Section 4.3, fiber orientation is computed in this research using the RSC model (cf. Equation 3-17). Our primary interest is in the direction of extrusion,

i.e., in the direction of the positive z axis in Figure 4-2. A different coordinate system is used in the polymer flow equations, which are written in terms of a cylindrical coordinate frame, than in the computation of the second order orientation tensor field which are in terms of a Cartesian coordinate frame. Hence, the velocity gradients computed in our polymer flow calculation are transformed to the Cartesian system for fiber orientation computation through (see e.g., [93])

$$\nabla \boldsymbol{v} = \begin{bmatrix} \frac{dv_r}{\partial r} & \frac{1}{r}\frac{dv_r}{d\theta} - \frac{v_\theta}{r} & \frac{dv_r}{dz} \\ \frac{dv_\theta}{dr} & \frac{1}{r}\frac{dv_\theta}{d\theta} + \frac{v_r}{r} & \frac{dv_\theta}{dz} \\ \frac{dv_z}{\partial r} & \frac{1}{r}\frac{dv_z}{d\theta} & \frac{dv_z}{dz} \end{bmatrix} = \begin{bmatrix} \frac{dv_1}{dx_1} & \frac{dv_1}{dx_2} & \frac{dv_1}{dx_3} \\ \frac{dv_2}{dx_1} & \frac{dv_2}{dx_2} & \frac{dv_2}{dx_3} \\ \frac{dv_3}{dx_1} & \frac{dv_3}{dx_2} & \frac{dv_3}{dx_3} \end{bmatrix}, \tag{4-14}$$

where we use subscript 1, 2, 3 to represent the coordinate directions in the 3D Cartesian frame when computing solutions to Equation 4-14. Spatial locations are transformed between (r,θ,z) and (x_1, x_2, x_3,) in the usual manner where we designate x_3 as the axial direction of the nozzle. Herein, our primary focus is on fiber alignment in x_3, which is best represented by the A_{33} component of the second order orientation tensor $\boldsymbol{A}$.

The solution of A_{33} along various streamlines shown in Figure 4-10 is computed based on the flow kinematics solved using the PTT rheology model (as an example) with Q = 100 mm^3/s. Values of A_{33} computed for each of the rheology models show similar trends as that appearing in Figure 4-10, so that these other results are omitted here for conciseness. ANSYS suite [74] generates the 2D surface streamlines based on the mesh quality. Due to the mesh defined in Figure 4-2, we consider flow velocity fields along 8 streamlines computed from the finite element results computed with ANSYS-Polyflow. Note that A_{33} values near unity indicate fibers are highly aligned along the x_3 direction. It can be seen that the fiber orientation tensor values start at steady state at flow inlet

(appearing as FI in Figure 4-10) as assumed. The A_{33} components then separate as the flow approaches the nozzle convergent zone (appearing as CZS in Figure 4-10). The peak value of the A_{33} component occurs at the convergent zone exit (appearing as CZE in Figure 4-10). Then the orientation tensor values along inner region streamlines decrease while those located at outer region increase as the flow continues towards the nozzle exit (appearing as NE in Figure 4-10). Once the polymer melt passes the nozzle exit at NE, values of A_{33} in outer region increase immediately and those more central begin to increase also, but more slowly. This change occurs due to the shear rate limitation vanishing at the outer boundary just after nozzle exit. The velocity along the outer boundary accelerates first, causing fibers nearby to orientate in the flow direction. Also, the elongational flow near the center of the nozzle accelerates so that the extrudate attains a uniform speed at some point not far from the nozzle exit. The final state of fiber orientation is set once variation across the bead ceases and a plug flow develops

Similar to the results appearing in Figure 4-10, we also compute the fiber orientation tensor along streamlines in the flow domain using other rheology models. Values of A_{33} at the end of the flow domain (i.e., across $\boldsymbol{\Gamma_6}$, in Figure 4-2) for all simulations considered here appear in Figure 4-11. Results indicate that the alignment of fiber generally increases from the edge of the flow towards the center of the extrudate for all applied rheology models. Also, it can be seen that the PTT model yields the lowest alignment in x_3 among the applied models. Alternatively, the Power law and Carreau-Yasuda law result in a similar steady state fiber orientation, which are the highest among these results. Moreover, the orientation result obtained using the SV model shows a good agreement with that of the PTT model in the shear dominant flow boundary but varies at

other locations within the flow. Finally, the Newtonian model yields an intermediate value of the fiber orientation, somewhat positioned between the GNF laws and the viscoelastic model results.

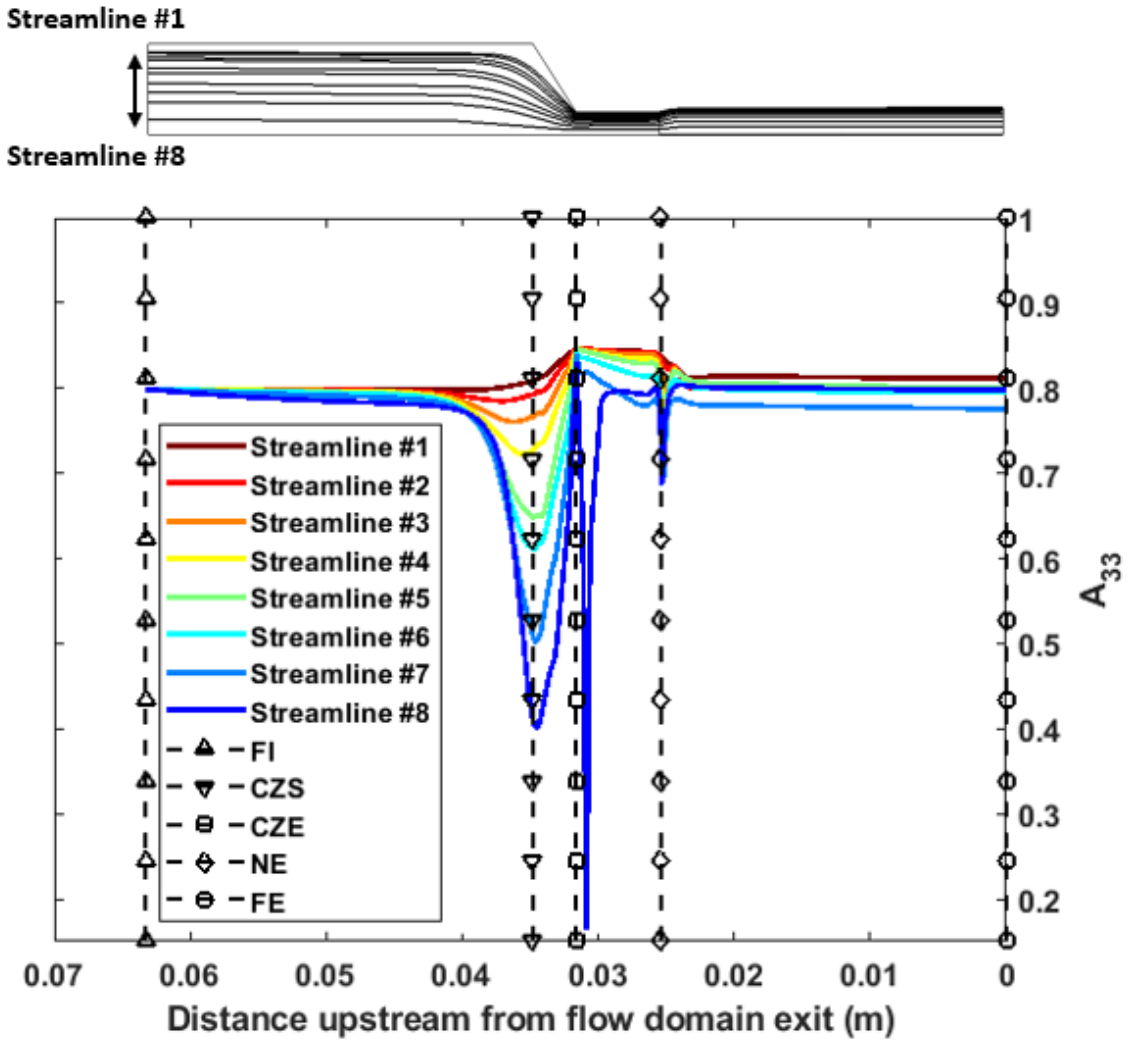

Figure 4-10. A_{33} component of fiber orientation solution computed using the flow kinematics solved by the PTT model at Q equates 100 mm^3/s.

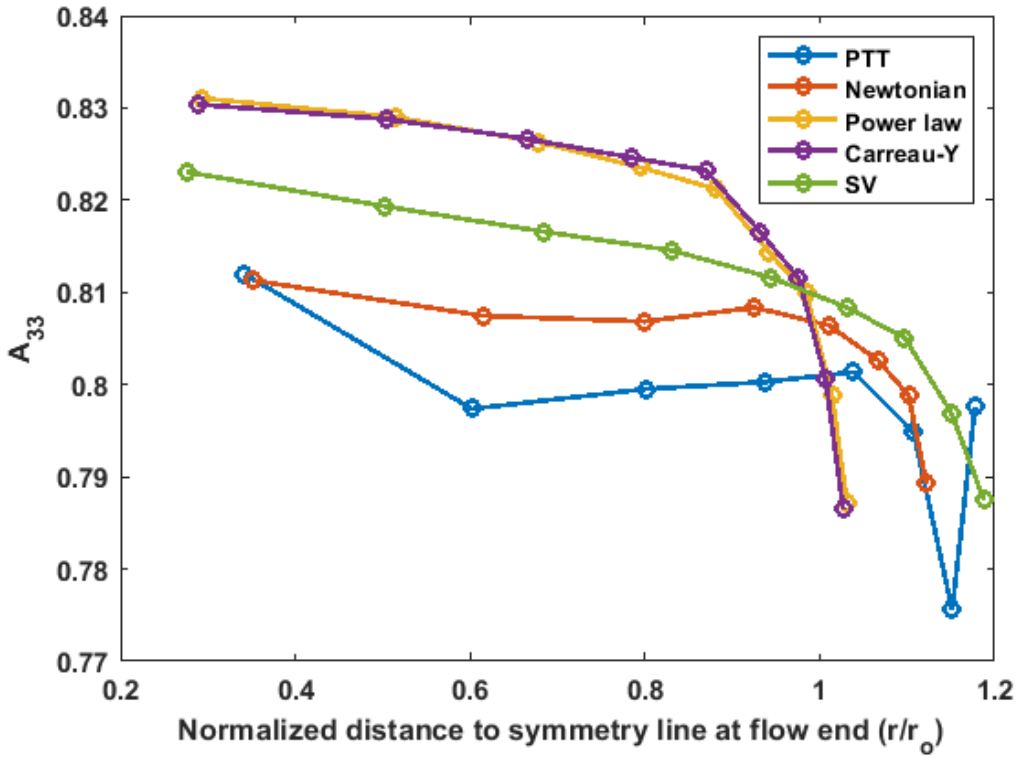

Figure 4-11. A_{33} component at the flow domain exit solved using employed rheology models.

4.4.3 Predicted Effective Elastic Constants

Elastic properties for a 13% CF-ABS using the volume-averaged stiffness tensor are computed from the steady state fiber orientation tensor (cf. Jack and Smith [89]) and the Tandon-Weng analytical equation (cf. Tandon and Weng [87]). In this work, values of orientation tensor components A_{ij} are calculated along flow streamlines with Equation 3-17 (i.e. RSC model) as described above. Then, elasticity tensor components $\tilde{C}_{ijkl}$ (cf. Equation 3-32) are computed at the end of each streamline (i.e., at the flow domain exit $\boldsymbol{\Gamma_6}$) which is considered to be the steady-state orientation state of the extruded bead. Extrudate cross-section averaged values form the mean bead stiffness tensor $\bar{C}_{ijkl}$ representing the material properties of the bulk composite extrudate, which can be written as

$$\bar{C}_{ijkl} = \frac{1}{\pi r_e^2}\int_0^{2\pi}\int_0^{r_e}(\tilde{C}_{ijkl}\cdot r)\, drd\theta, \tag{4-15}$$

which are obtained through numerical integration using the trapezoidal rule as in [42]. In the above, r_e is the radius of the free extrudate at the flow domain exit which is different for each rheology model. To present the results with a clear view, we further calculate the mean elastic properties of computed results of material stiffness by [98]

$$[\mathbf{C}]^{-1} = \begin{Bmatrix} \frac{1}{E_{11}} & -\frac{\nu_{21}}{E_{22}} & -\frac{\nu_{31}}{E_{33}} & 0 & 0 & 0 \\ -\frac{\nu_{12}}{E_{11}} & \frac{1}{E_{22}} & -\frac{\nu_{32}}{E_{33}} & 0 & 0 & 0 \\ -\frac{\nu_{13}}{E_{11}} & -\frac{\nu_{23}}{E_{22}} & \frac{1}{E_{33}} & 0 & 0 & 0 \\ 0 & 0 & 0 & \frac{1}{G_{12}} & 0 & 0 \\ 0 & 0 & 0 & 0 & \frac{1}{G_{13}} & 0 \\ 0 & 0 & 0 & 0 & 0 & \frac{1}{G_{23}} \end{Bmatrix}, \tag{4-16}$$

where $[\mathbf{C}]$ is a 6×6 matrix, which refers to a material stiffness matrix, C_{ijkl}, written in contracted notations [98]. Subscripts {1,2,3} refer to coordinate directions of a 3D Cartesian coordinate. For our calculations, the elastic properties of the fiber and matrix phase materials are given in Table 4-5, where *E*, *G* and ν refer to the Young's modulus, shear modulus and the Poisson's ratio, respectively.

Additionally, the 13% CF-ABS material supplied from PolyOne is 13% fiber weight percentage (wt.) while the Tandon-Weng approach requires the fiber volume fraction in its computation process. The density values of the ABS and carbon fiber are 1040 and 1700 $\mathrm{kg/m^3}$, respectively [55]. Thus, we translate the weight fraction to the volume fraction through the following equation as

$$vol = wt_f\ \rho_m/[wt_f\ \rho_m + (1 - wt_f)\rho_f], \tag{4-17}$$

where "vol" and "wt" are the fiber volume percentage and weight percentage, respectively, and ρ refers to the density of the material. The subscripts "f" and "m" indicate the fiber and matrix phases, respectively. Consequently, the fiber volume fraction of the composite system is 8.4%.

Computed results shown in Table 4-6 indicate that the printed composite exhibit quasi transverse isotropic mechanical behavior. Specifically, the Carreau-Yasuda law (i.e., appearing as Carreau-Y. in Table 4-6) yields the highest $\bar{E}_{33}$ value while the PTT model results in the lowest. In contrast, the shear moduli computed using the PTT model are higher than those computed with all GNF models. Finally, as we consider more non-viscous effects of the flow (e.g., see data from the Power law or the Carreau-Yasuda law, to the PTT model), it can be seen that the principal (i.e., direction of the flow) mean modulus ($\bar{E}_{33}$) decreases while other moduli increase. Also, the transverse isotropic behavior of results predicted by the PTT model is the most obvious one, in which the $\bar{E}_{33}$ and $\bar{G}_{23}$ are unique values and $\bar{E}_{11}$, $\bar{E}_{22}$ as well as $\bar{G}_{12}$,$\bar{G}_{13}$ show highly agreement. Our material stiffness predictions show a good agreement generally with test data appearing in the literature. For comparison, Duty, et al. [12] measured the Young's modulus of a 13 % CF-ABS printed bead, reporting a mean value of 7.24 GPa and standard deviation of 0.59 GPa. Our predictions of the elastic modulus for the same material system shown as $\bar{E}_{33}$ in Table 4-6 are slightly higher than these previously published experimental results. The overestimation of our simulation may be caused by neglecting the effects of microstructural voids (cf. Figure 1-1B), macro-level inter-bead voids and material distribution variance during bead deposition in the properties prediction. In addition, Duty found the stiffness of a BAAM printed tensile test sample to be highly anisotropic,

which is also seen in our results. Furthermore, the previously reported test sample transvers moduli show some skewness in the transverse plane (i.e., $\bar{E}_{11}$ = 2.26 GPa and $\bar{E}_{22}$ = 2.56 GPa). Our results also present the similar trend (e.g., PTT model results: $\bar{E}_{11}$ = 3.14 GPa and $\bar{E}_{22}$ = 3.43 GPa). While we are not able to show experimental data specific to each rheology model, the overall favorable comparison with previously published experimental work supports our computational approach.

Table 4-5. Elastic Properties of the Phase Materials of a 13% wt. CF-ABS.

Material	E (GPa)	G (GPa)	ν
ABS matrix	2.25	0.83	0.35
Carbon fiber	230	96	0.2

Note, the volume fraction of the material model is 8.4%.

Table 4-6. Predicted Mean Elastic Properties of the Printed Extrudate.

Model name	$\bar{E}_{11}$ (GPa)	$\bar{E}_{22}$ (GPa)	$\bar{E}_{33}$ (GPa)	$\bar{G}_{12}$ (GPa)	$\bar{G}_{23}$ (GPa)
PTT	3.14	3.43	10.14	1.12	1.61
Power law	3.13	3.40	11.24	1.10	1.59
Carreau-Y.	3.13	3.40	11.28	1.10	1.59
Newtonian	3.14	3.42	10.61	1.11	1.61
SV model	3.14	3.42	10.83	1.11	1.61

Table 4-6. Predicted Mean Elastic Properties of the Printed Extrudate (continued).

Model name	$\bar{G}_{13}$ (GPa)	$\bar{\nu}_{12}$	$\bar{\nu}_{13}$	$\bar{\nu}_{23}$
PTT	1.36	0.45	0.38	0.39
Power law	1.31	0.46	0.36	0.41
Carreau-Y.	1.30	0.46	0.36	0.41
Newtonian	1.34	0.45	0.37	0.40
SV model	1.33	0.46	0.37	0.40

In addition, we note that the finite element domain is discretized into 704 nodes and 630 elements using 4-node quadrilateral elements as shown in Figure 4-7. The mesh size is reduced near the flow boundary as well as the nozzle exit to avoid potential singularity issues. Additionally, results obtained using a coarse mesh (448 nodes, 378 elements) and a fine mesh (960 nodes, 882 elements) are compared with those obtained with the model in Figure 4-2. We found that the elastic moduli predictions appearing in Table 4-6 using the model in Figure 4-7 are within 1% absolute relative difference to the fine mesh model output. We therefore use the model in Figure 4-2 in this chapter to avoid the extra computational expense that would be required for a model having a finer mesh.

CHAPTER FIVE

Impacts of Screw Swirling Effects

This chapter has been published as part of the citation [99]: Wang, Zhaogui, and Douglas E. Smith. "Numerical analysis of screw swirling effects on fiber orientation in large area additive manufacturing polymer composite deposition." *Composites Part B: Engineering (2019): 107284.*

Large Area Additive Manufacturing (LAAM) polymer deposition employs a single screw extruder to deliver pelletized feedstock (cf. Figure 2-1), which results in significantly higher flow rates as compared to conventional filament-based extrusion additive processes. Swirling kinematics in LAAM melt flow that result from the screw rotation are expected to generate unique particle alignment patterns within the fiber-filled polymer during deposition processing.

This chapter extends the flow domain appearing in last chapter and investigates the effect of the single screw swirling motion on the resulting fiber orientation in a short fiber polymer composite extrudate. An axisymmetric non-Newtonian viscoelastic flow is simulated with the finite element method, where the flow nearby the extruder screw tip, within the printing nozzle, and a short section of free extrudate compose the flow domain (cf. Figure 5-1). Fiber orientation tensors within the flow domain are evaluated using the Wang-O'Gara-Tucker Reduced Strain Closure (RSC) fiber orientation diffusion model [56]with the Orthotropic fitted closure [86].

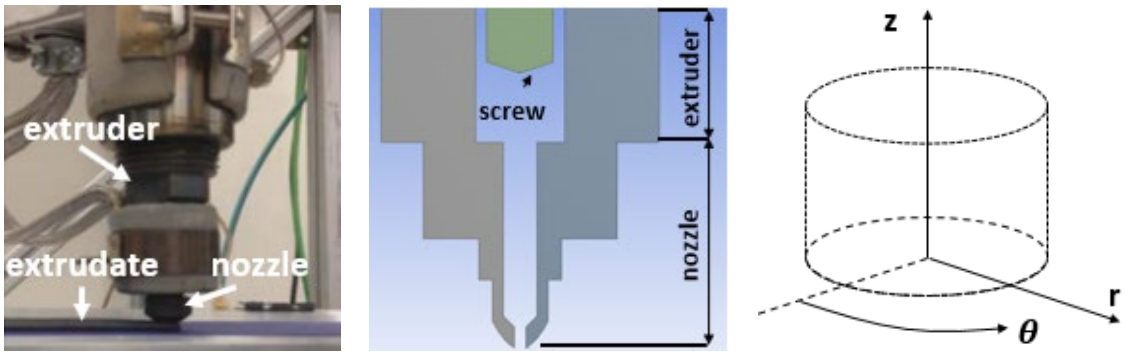

(A) (B) (C)

Figure 5-1. Strangpresse Model 19 single screw extruder nozzle: (A) external view of nozzle; (B) flow of interest; (C) cylindrical coordinates system.

5.1 Material Rheometry Input

In this chapter, the simulation method for fiber suspension flow is the same weakly coupled formulation as did in Chapter Four. Even though under the weakly coupled formulation, it is still useful to take the effects of the fiber and associated orientation into the consideration of flow computation. To this end, we consider rheological properties of the 13% CF-ABS (supplied by PolyOne) directly for the simulation carried on here while the last chapter only measures the properties of virgin ABS polymer. Particularly, modeling the melt flow with measured rheological data of the 13% CF-ABS is regarded as an indirect approach to count some effect of the fibers and associated alignments on the flow fields formulation in the nozzle extrudate flow domain.

Rheological frequency sweep testing is performed for the 13% CF-ABS using the rotational rheometer HAKEE MARS 40 (Thermo Fisher Scientific, Waltham, MA) at 215 Celsius, which is a common temperature for printing of this material. Dynamic viscosity is measured over a frequency range of 0.01–100 Hz which are converted to shear rate using the Cox-Merz rule [100], as did in Chapter Four. It should be noted that the application of the Cox-Merz rule for filled polymer systems can influence the

predicted rheological properties. Prior experimental work [101] has shown that the deviation between Cox-Merz-rule-estimated data and the same measured by a capillary rheometer can be as high as one order of magnitude (e.g., ~10×) when fiber filled composites are employed. While the presence of fiber reinforcements may introduce error into the measured data, it is expected that the swirling kinematics of the relatively low fiber content polymer flow would not be greatly affected as compared to other factors, such as the inlet flow rate or screw RPM. An alternative approach is to employ a fully-coupled fiber orientation-flow analysis (e.g., see VerWeyst and Tucker [53] and Chapter Seven below) that more directly incorporates the effects of fiber reinforcements into the computation of the flow.

The Phan-Thien-Tanner (PTT) model is used here to simulate the polymer melt rheology in LAAM deposition. PTT model parameters are computed for measured viscosity values using ANSYS Polymat [91] where curve fit results of the PTT model appear in Figure 5-2 and the parameters fitted for the PTT model are given in Table 5-1. Note that the length of each error bar appearing in Figure 5-2 is twice of the absolute value between the measured data and the fitted data at that shear rate. It can be seen that the fitted rheology properties show a good agreement with those obtained from the frequency sweep test, except at extreme shear regions (e.g., very small or very large shear rates).

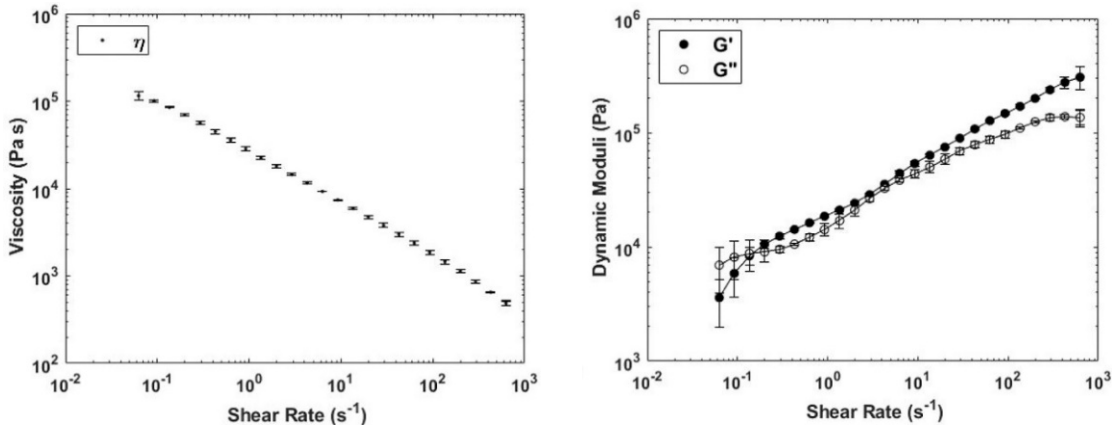

(A) (B)

Figure 5-2. Rheological Properties Measured through Frequency Sweep Test: (A) Shear Viscosity; (B) Dynamic Shear Moduli.

Table 5-1. PTT model fitted parameters for ABS.

Mode No. (i)	λ_i^r(s)	$\eta_{2_i}\,(Pa \cdot s)$
1	0.0032	719.238
2	0.024	2009.14
3	0.17	6812.35
4	1.37	11716.6
5	10.00	124392

Note, ε_{PT} and ξ_{PT} (cf. Equation 4-7) are fitted as 0.5 and 0.15, respectively

5.2 Flow and Fiber Orientation Modeling

The flow domain considered in this chapter includes the lower section of the extruder near the tip of the rotating screw, the nozzle, and a short section of free extrudate just outside the nozzle exit as shown in Figure 5-3. Notice, the rotating screw tip introduces swirling kinematics into the flow fields and thus the flow model developed in this chapter yields non-trivial velocity fields in the θ direction of a 3D cylindrical coordinate (cf. Figure 5-1C).

As did in Chapter Four, an axisymmetry flow domain is assumed which is modeled with a 2-D finite element mesh to reduce computational expense. Gravity is not

considered in the simulation. In addition, the length of free extrudate in the model is one-inch which allows for the fiber orientation to reach steady state beyond the nozzle exit. As the design of the single screw is not provided by the manufacturer, we have chosen to adapt the geometries as referred in Duty, et al. [12], where the investigated large-scale polymer deposition system incorporated a 25-mm (~1-inch) diameter screw. In addition, Duty has improved the design of a screw in order to achieve higher material feeding rate, where a 50-mm (~2-inch) longer screw is used as an alternative design. Based on data in Duty, et al. [12], we assume an 1-inch distance between the screw tip to the nozzle entrance as shown in Figure 5-3. Additionally, the angle of the screw tip is assumed as shown. Moreover, the boundary conditions for the flow domain appear in Figure 5-3, where most of the boundaries share the same definition as did in Section 4.1 for the nozzle flow, such that

- $\boldsymbol{\Gamma_1}$: Flow inlet with the prescribed volumetric flow rate Q. In this Chapter, Q is increased to 1000 mm^3/s, which is a result computed based on an 80 RPM screw speed of the Strangpresse Model 19 extruder or approximately 8 lbs./hour of 13% CF-ABS.
- $\boldsymbol{\Gamma_2}$: No slip wall boundary, where $v_s = v_n = 0$.
- $\boldsymbol{\Gamma_3}$: Screw barrel edge, where $v_s = v_n = 0, v_\theta = \frac{2\pi r n_s}{60} = 8.4r$ for a screw RPM of n_s = 80. Note that r is the radial distance in the axisymmetric model as defined in Figure 5-2.
- $\boldsymbol{\Gamma_4}$: Axis of symmetry, where $F_s = v_n = 0$.
- $\boldsymbol{\Gamma_5}$: Free surface, where $\mathbf{v} \cdot \vec{\boldsymbol{n}} = 0$.
- $\boldsymbol{\Gamma_6}$: Flow domain exit, where $F_n = v_s = 0$.

In addition, fiber orientation tensors within the flow domain are evaluated using the RSC) model (cf. Equation 3-17) with the Orthotropic fitted closure [86] in the common weakly coupled formulation as did in Chapter Four (cf. Section 4.3 for more detail).

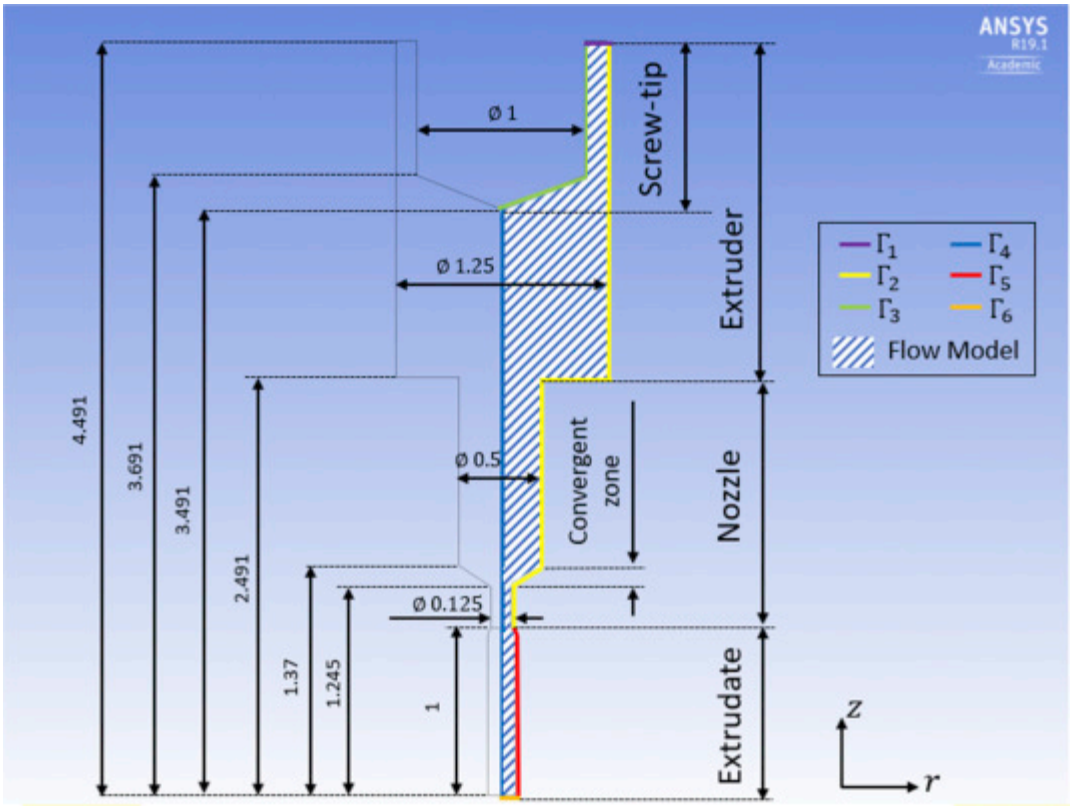

Figure 5-3. The Boundary Conditions of the Swirling Flow Domain (units: inches)

5.2.1 Screw Swirling Flow Kinematics

Flow fields within the extrusion orifice induce the suspending fibers to orientate and ultimately form the fiber alignment of an extrudate of fiber filled polymers. To evaluate fiber orientation in the LAAM process, we focus on the velocity and velocity gradients within the polymer melt flow through the extruder nozzle and within the die swell just outside the nozzle exit. The flow domain in our work is based on the single screw extruder, which is common in LAAM polymer deposition additive manufacturing

systems. The flow domain in our model includes the lower section of the extruder near the tip of the rotating screw (cf. Figure 5-3 for example). Axisymmetry of the flow domain is assumed which is modeled with a 2D finite element mesh to reduce computational expense. However, with the consideration of the tip of the single screw, the swirling kinematics will be added such that the velocity vectors solved through Equations 3-1 and 3-2 will contains non-trivial values for both v_r, v_z, and v_θ, whereas a typical FFF process flow fields can be depicted with only v_r, and v_z. To obtain a clear view of the flow computation, we extend the continuity and momentum equations (cf. Equations 3-1 and 3-2) in a 3D cylindrical coordinate, such that [73]

$$\frac{1}{r}\frac{\partial(\rho r v_r)}{\partial r} + \frac{\partial \rho v_z}{\partial z} = 0, \tag{5-1}$$

and,

$$\rho\left(v_r\frac{\partial v_r}{\partial r} - \frac{{v_\theta}^2}{r} + v_z\frac{\partial v_r}{\partial z}\right) = -\frac{\partial P}{\partial r} - \left[\frac{1}{r}\frac{\partial}{\partial r}(r\tau_{rr}) - \frac{\tau_{\theta\theta}}{r} + \frac{\partial \tau_{zr}}{\partial z}\right], \tag{5-2}$$

and

$$\rho\left(v_r\frac{\partial v_\theta}{\partial r} - \frac{v_r v_\theta}{r} + v_z\frac{\partial v_\theta}{\partial z}\right) = -\left[\frac{1}{r^2}\frac{\partial}{\partial r}(r^2\tau_{r\theta}) + \frac{\tau_{\theta r}-\tau_{r\theta}}{r} + \frac{\partial \tau_{z\theta}}{\partial z}\right], \tag{5-3}$$

and

$$\rho\left(v_r\frac{\partial v_z}{\partial r} + v_z\frac{\partial v_z}{\partial z}\right) = -\frac{\partial P}{\partial z} - \left[\frac{1}{r}\frac{\partial}{\partial r}(r\tau_{rz}) + \frac{\partial \tau_{zz}}{\partial z}\right], \tag{5-4}$$

where P is pressure, ρ is the density of the polymer, τ is the component of the shear stress tensor, and r, z, θ refer to the three major directions in a cylindrical coordinate system as shown in Figure 5-1C. Equations 5-1 to 5-4 may be obtained from the more general Navier-Stokes equations [73] for steady flows having no inertia or gravity, and setting all derivatives with respect to θ to zero. Particularly, the non-trivial solution of v_θ alters the

streamlines of the fluid flow of interest from their surface projections, where the later is usually employed in the computation of fiber orientation.

In addition to the swirling flow defined above, a straight flow model is also considered for comparison. The straight flow model shares the same nozzle geometry, flow rate and melt flow rheology with the swirling flow, except that no rotational kinematics are assigned to $\mathbf{\Gamma_3}$ (cf. Figure 5-2), i.e.,

$$v_\theta = 0, \tag{5-5}$$

with a no-slip wall boundary condition. Evaluating the polymer melt flow and fiber orientation in the straight flow models provides a means to directly assess the effects of swirling kinematics on predicted outcomes. Both swirling flow and straight flow models are created in 2D, where all partial derivatives with respect to θ direction are zero. The v_θ component in the swirling flow is a computed non-zero solution variable. In the straight flow model, v_θ and all derivative with respect to θ are set to zero, such that Equation 5-2 reduce to

$$\rho\left(v_r\frac{\partial v_r}{\partial r}+v_z\frac{\partial v_r}{\partial z}\right)=-\frac{\partial P}{\partial r}-\left[\frac{1}{r}\frac{\partial}{\partial r}(r\tau_{rr})+\frac{\partial \tau_{zr}}{\partial z}\right], \tag{5-6}$$

In this formulation (i.e., straight flow model), Equation 5-3 no longer applies, such that flow domain velocities are computed using Equations 5-1, 5-4, and 5-6 in the usual manner. Also, the extrudate swell of the free extrudate boundary surface is evaluated using the methods of spines through ANSYS Polyflow, as did in Chapter Four.

Note, both the swirling flow and straight flow models assume all partial derivatives with respect to theta are zero. The swirling flow model imposes the boundary condition along the surface of the screw tip to simulate steady rotating motion as described above. While the flow simulation for both models is performed within the *r-z*

plane (cf. Figure 5-3), the swirling flow model requires streamlines and fiber orientation tensors be computed in three-dimensional space. With the exception of the detail around the screw tip, both the swirling flow and straight flow model share the same nozzle geometry, flow rate, and polymer melt flow properties.

5.3 Results and Discussion

Computed values of flow velocity, fiber orientation tensors, and associated elastic properties obtained from the LAAM nozzle simulation approach describe above are given in this section.

5.3.1 Swirling and Straight Flow Models Streamlines

The weakly coupled formulation adopted in our study solves the fiber orientation tensor equation of motion from velocity and velocity gradient values along streamlines in the flow domain. Melt flow streamlines computed in our swirling flow and straight flow simulations appear in Figures 5-4 and 5-5. Streamlines computed with the swirling flow model appear in Figure 5-4 where the out-of-plane coordinates of the 3D streamline are obtained by computing the angle of rotation θ from

$$\theta = \int_0^t \dot{\theta} dt, \tag{5-7}$$

where $\dot{\theta} = \frac{v_\theta}{r}$, and v_θ and r are obtained along surface projection streamline (i.e., computed results from Polyflow). Equation 5-7 is calculated through a trapezoidal rule numerical integration approach [102]. Figure 5-5 shows the surface projection streamlines as computed by Polyflow for both the straight flow and swirling flow simulations. It can be seen from Figure 5-5 that the swirling flow model yields much different path through the flow domain than that of 2D straight flow. Note that the

swirling flow streamlines appear closer to the center of the flow than those of straight flow in the region between the screw tip and nozzle entrance. In a steady state flow problem such as the simulations involved in our study, the streamlines are the same as the pathlines that particles would follow throughout the flow domain. We would, therefore, expect a distinguishable difference between the straight flow and swirling flow fiber orientation tensors near the screw tip, and downstream from the screw tip as well.

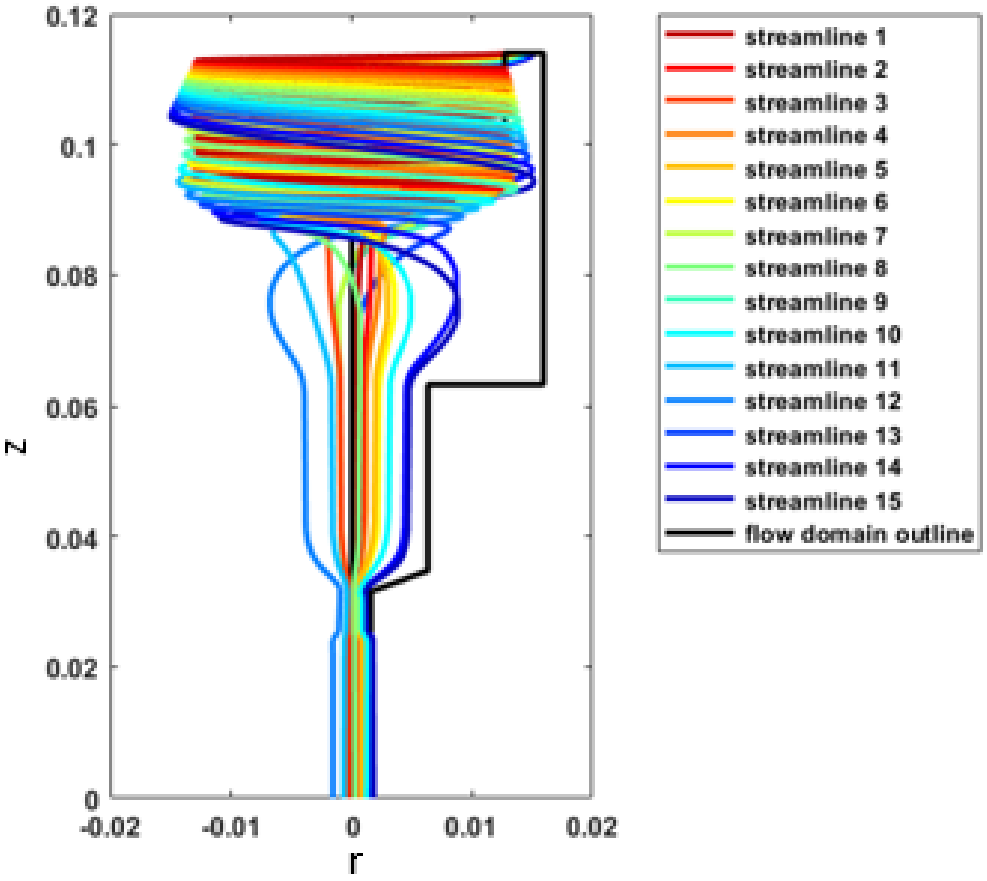

Figure 5-4. 3D streamlines of the melt flow computed with the swirling flow model (length values in meters).

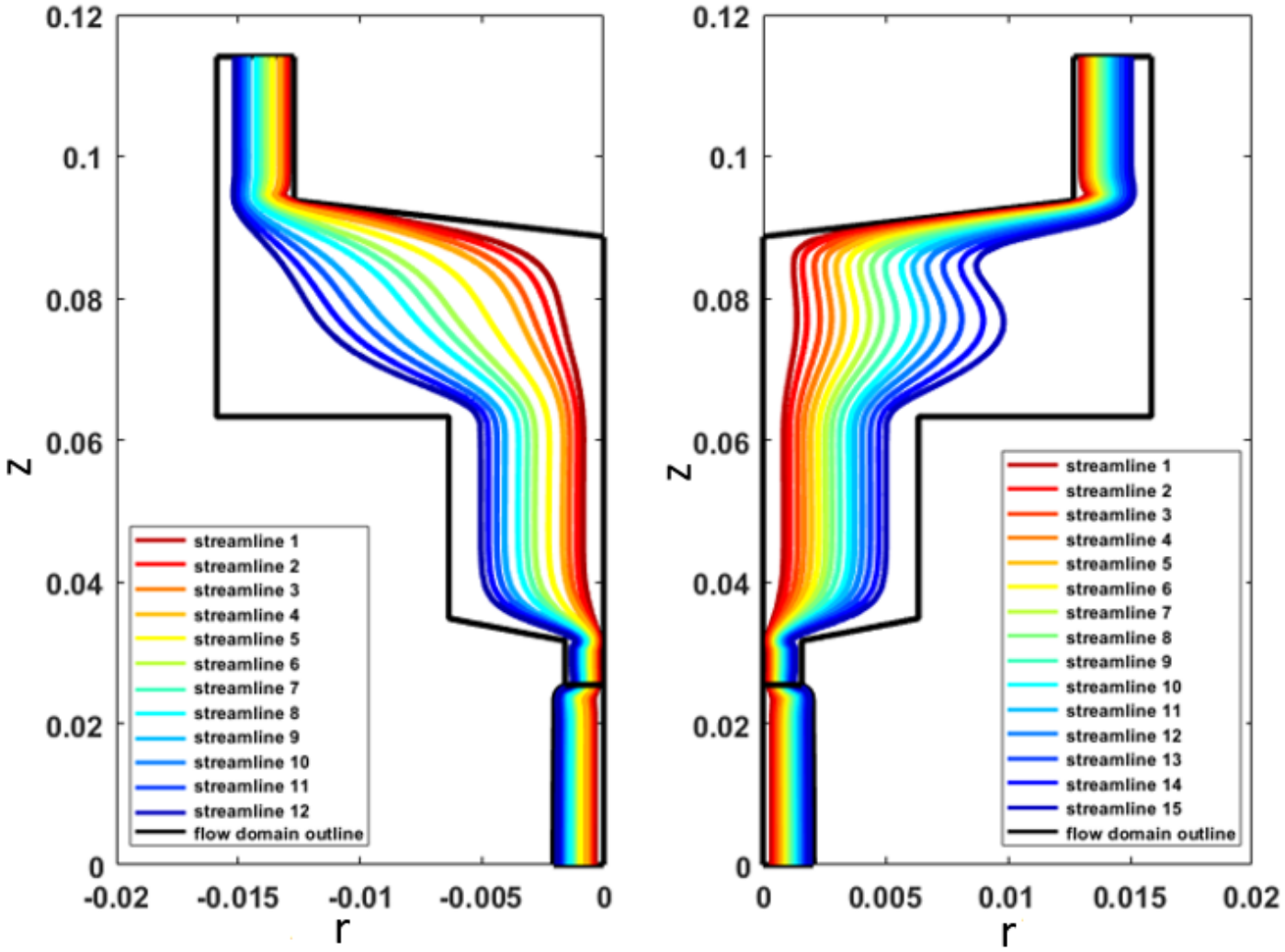

(A) (B)

Figure 5-5. Surface projections of the flow streamlines: (A) straight flow and (B) swirling flow simulation.

5.3.2 Fiber Orientation Tensors

Results of fiber orientation tensors are computed by integrating Equation 3-17 (i.e., RSC fiber orientation model) along a streamline using an adaptive fourth-order Runga-Kutta scheme [102], where a steady-state initial condition is required at the flow inlet (i.e., $\mathbf{\Gamma_1}$ in Figure 5-3). Heller, et al. [19] assumed the fiber orientation state upstream of the flow inlet reaches steady state based on the upstream homogeneous flow field. We adopt the same assumption by first computing the fiber orientation of a sufficiently long extruder tube (not shown here) for the same flow rate Q evaluated above starting with a random alignment at its inlet. Computed orientation tensor values at the exit of this tubular flow domain are used to define the inlet initial condition in the following fiber orientation computations. The inner and outer radii of the tubular geometry used to obtain these initial conditions are the same as those appearing in Figure 5-3 for the nozzle at z = 4.491 inch (i.e., at $\mathbf{\Gamma_1}$ in Figure 5-3). We set v_θ = 0 in the steady flow initial conditions simulation for the straight flow, and define v_θ based on the extruder screw diameter and RPM for the swirling flow in a similar manner as that described above for our nozzle flow simulations. Selection of the RSC modeling parameters is the same as did in Chapter Four, such that C_I=0.01, κ=0.1, and λ_{a_r}=1 [56].

Results appearing in Figures 5-6 through 5-9 are the A_{11} and A_{33} components of computed fiber orientation tensors along the flow domain streamlines of the straight flow and swirling flow models. In this section, “Nozzle CZS” and “Nozzle CZE” refer to Nozzle Convergent Zone Start and Nozzle Convergent Zone End. Our results show that the initial steady orientation state of the straight flow has more fibers that align along the

principal flow direction (e.g., z direction), while that of the swirling flow align normal to the flow direction due to the swirling effects.

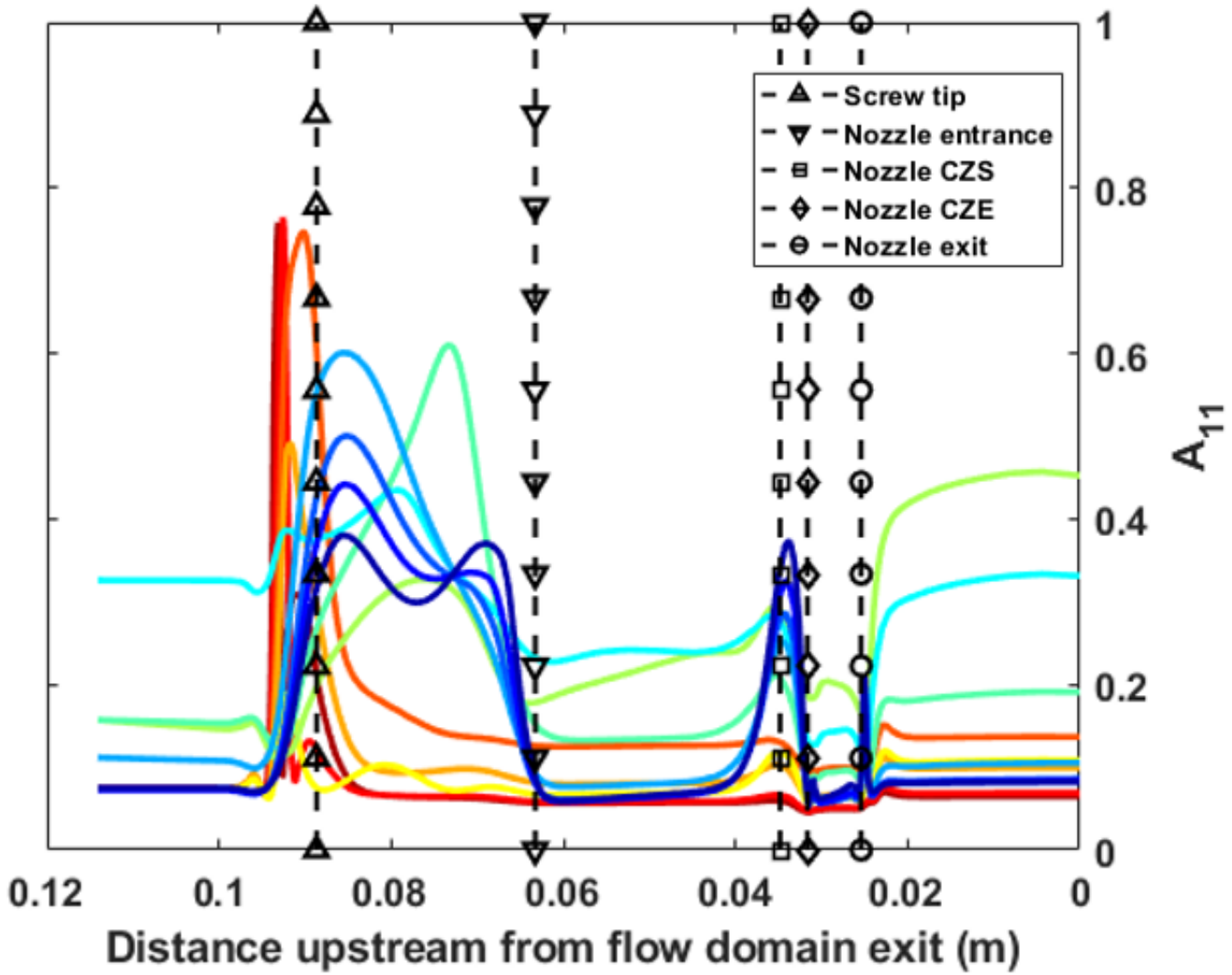

Figure 5-6. Fiber Orientation Tensor A_{11} Component through the Straight Flow Domain (color indicates streamline as defined in Figure 5-5A).

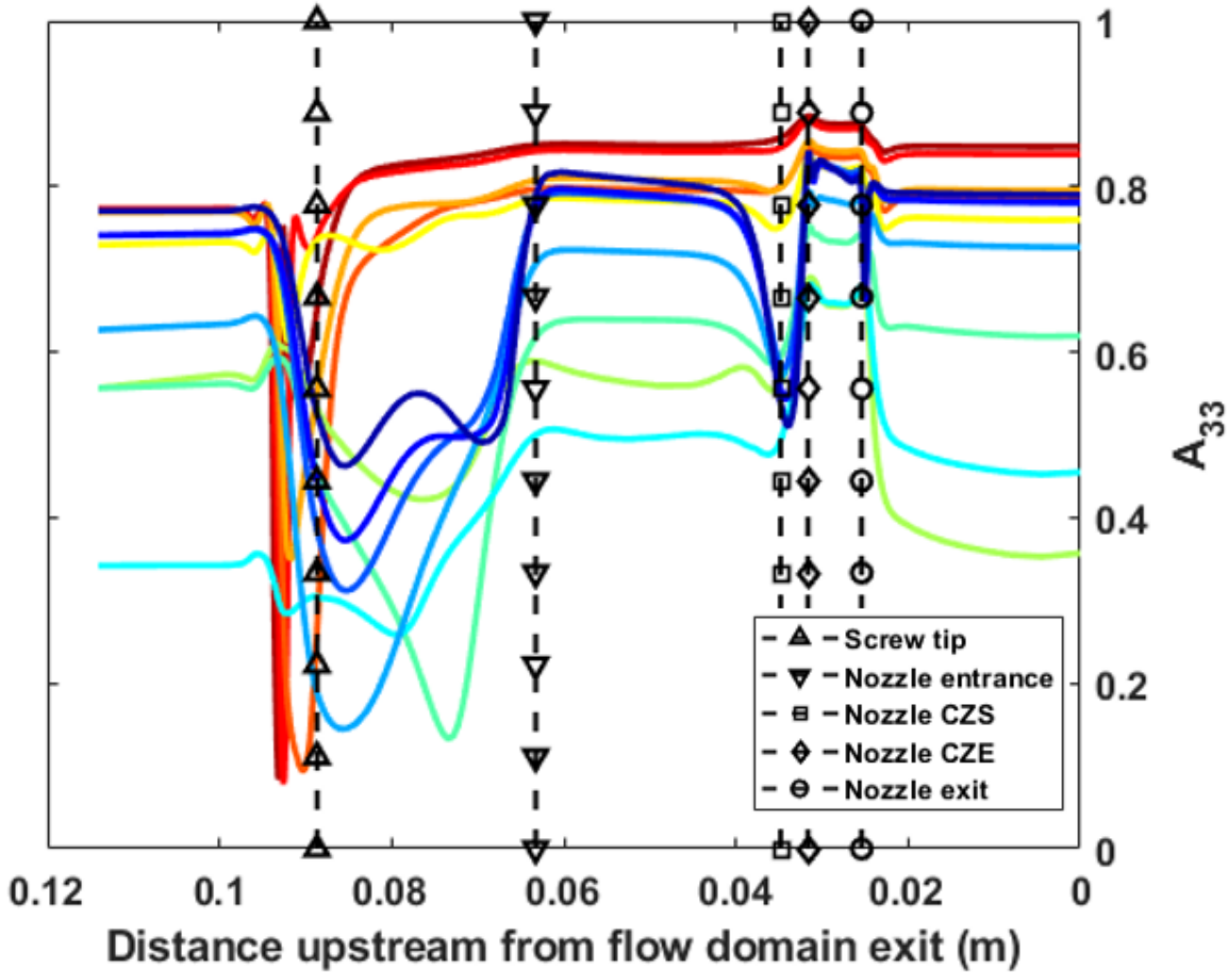

Figure 5-7. Fiber Orientation Tensor A_{33} Component through the Straight Flow Domain (color indicates streamline as defined in Figure 5-5A).

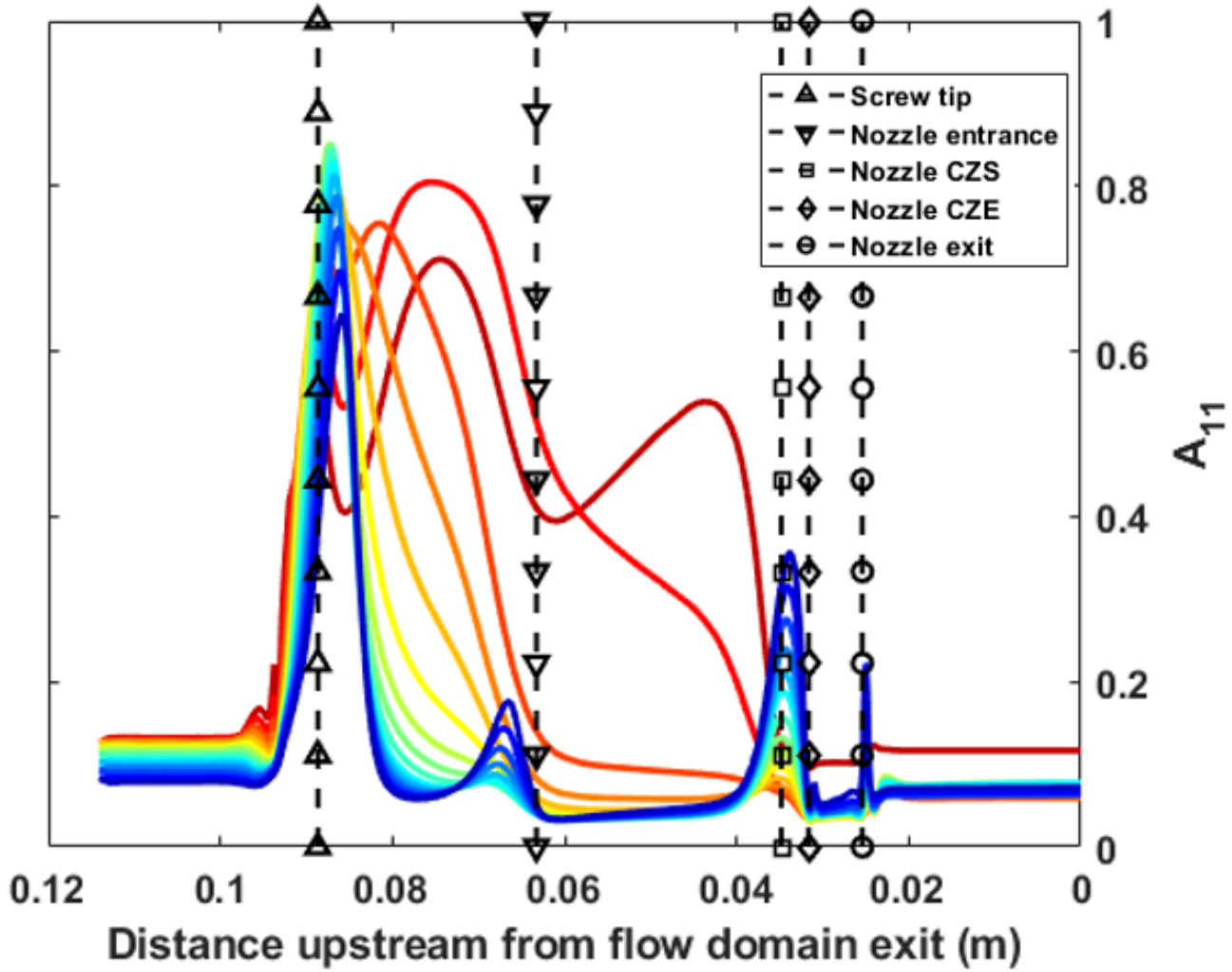

Figure 5-8. Fiber Orientation Tensor A_{11} Component through the Swirling Flow Domain (color indicates streamline as defined in Figure 5-5B).

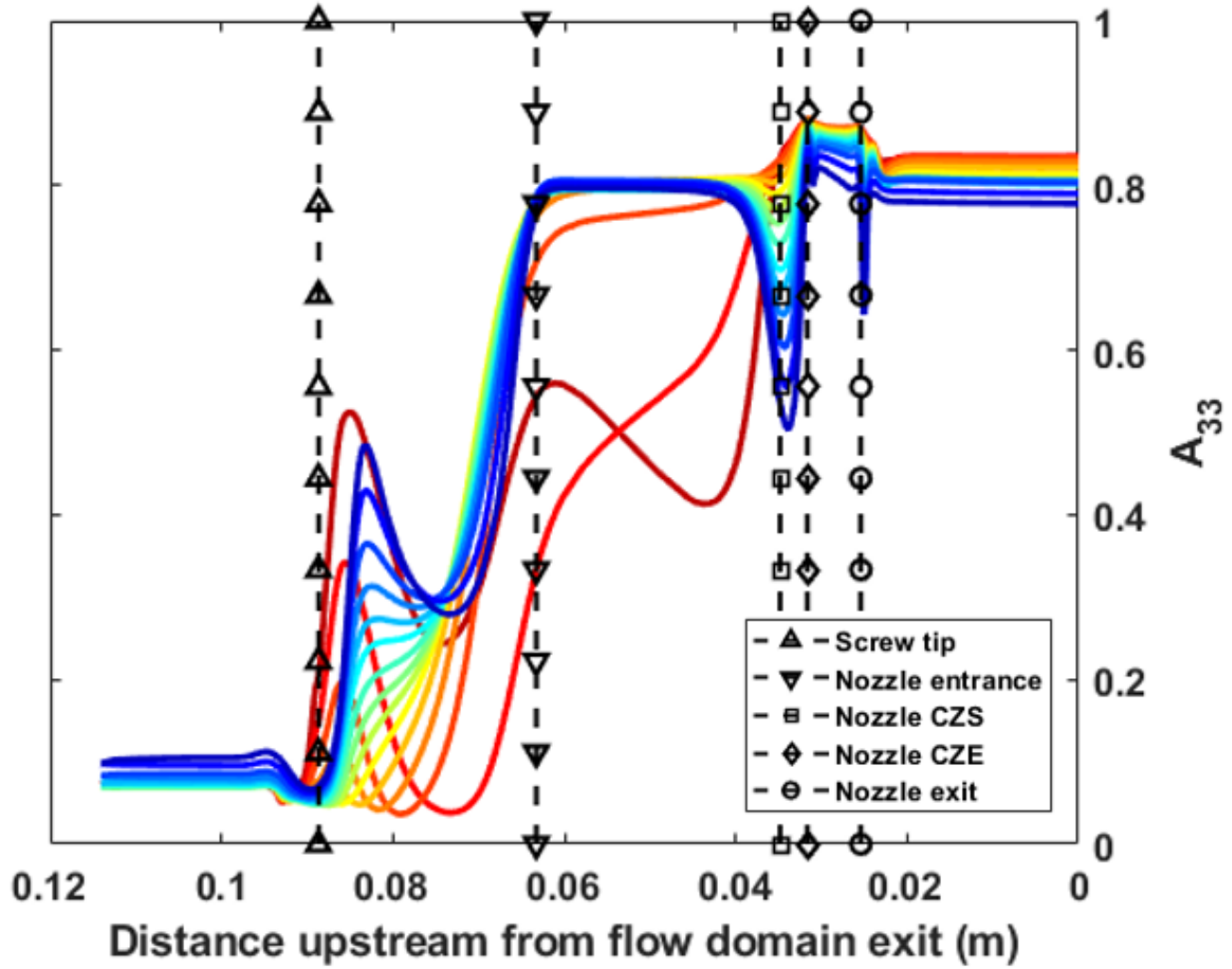

Figure 5-9. Fiber Orientation Tensor A_{33} Component through the Swirling Flow Domain (color indicates streamline as defined in Figure 5-5B).

5.3.3 Effects of Swirling Kinematics in Fiber Orientation Solution

It is generally known that shear dominated flows tend to align fibers along flow direction while elongational flows promote fiber alignment in the principle stretching direction. Heller, et al. [19] illustrates the correlation between the strain rate fields and the resulting orientation tensors for 2D axial extrusion nozzle flow, which is similar to the straight flow considered in this study (cf. Figure 5-5A). To better illustrate the effect of the velocity gradient fields on the fiber orientation kinetics in 3D swirling streamlines (cf. Figure 5-4), we rotate computed velocity gradients into a tangential-normal coordinate system for each point along swirling streamline, as shown in Figure 5-10.

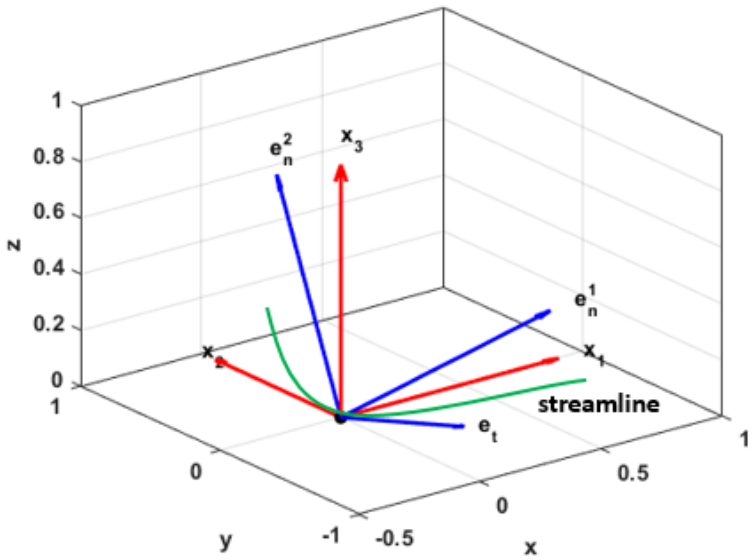

Figure 5-10. Tangential-Normal Coordinates of a Point on Streamline 15 of the Swirling Flow Simulation.

We define the tangential-normal coordinate system at each point along a streamline by first computing the tangential unit vector (e_t) of the point as

$$e_t = \frac{\boldsymbol{v}}{||v||} = [e_t^1, e_t^2, e_t^3], \tag{5-8}$$

where $\boldsymbol{v}$ is the velocity vector at the point of interest given in global Cartesian coordinates and $||\boldsymbol{v}||$ indicates the magnitude of the velocity vector. In this calculation procedure, velocity gradients $\nabla\boldsymbol{v}$ are first computed in cylindrical coordinates in Polyflow which are transformed to global Cartesian coordinates using Equation 4-14 (cf. Chapter Four). These transformed velocity gradients are further rotated to the tangential-normal coordinates of the streamlines using the rotation matrix

$$\boldsymbol{R^c} = \begin{bmatrix} 1 & 0 & 0 \\ 0 & \cos(\beta_1) & -\sin(\beta_1) \\ 0 & \sin(\beta_1) & \cos(\beta_1) \end{bmatrix} \begin{bmatrix} \cos(\beta_2) & -\sin(\beta_2) & 0 \\ \sin(\beta_2) & \cos(\beta_2) & 0 \\ 0 & 0 & 1 \end{bmatrix}, \tag{5-9}$$

where

$$\beta_1 = \cos^{-1}(e_t^3),\ \beta_2 = \pi/2\ - \sin^{-1}\left[\frac{e_t^2}{\sin(\beta_1)}\right], \tag{5-10}$$

Then final rotated $\nabla\boldsymbol{v}$ is evaluated in the tangential-normal coordinate at each point from

$$\nabla\boldsymbol{v}^{e_t - e_n^1 - e_n^2} = (\boldsymbol{R^c})^T(\nabla\boldsymbol{v})(\boldsymbol{R^c}) = \begin{bmatrix} \frac{dv_t}{de_t} & \frac{dv_t}{de_n^1} & \frac{dv_t}{de_n^2} \\ \frac{dv_n^1}{de_t} & \frac{dv_n^1}{de_n^1} & \frac{dv_n^1}{de_n^2} \\ \frac{dv_n^2}{de_t} & \frac{dv_n^2}{de_n^1} & \frac{dv_n^2}{de_n^2} \end{bmatrix}, \tag{5-11}$$

The x_1 axis in the Cartesian coordinates is rotated to the direction of e_t, and then the x_2, x_3 axes represent the directions of e_n. Here, $\frac{dv_t}{de_t}$ refers to the normal strain rate field. In addition, it is important to note that the choice of e_n is not unique but must remain in the plane normal to e_t. We use the magnitude of $\frac{dv_t}{de_n}$ which is computed as

$$||\frac{dv_t}{de_n}|| = \sqrt{(\frac{dv_t}{de_n^1})^2 + (\frac{dv_t}{de_n^2})^2}, \tag{5-12}$$

to represent the variance of the shear strain field along the flow domain. Following Equations 5-8 to 5-12, the strain rate tensors components along streamlines 1, 8 and 15 (cf. Figure 5-5B) of the swirling flow results are computed and plotted in Figures 5-11 to

5-13. These streamlines are chosen as examples since they represent the core (streamline 1), intermediate (streamline 8) and boundary (streamline 15) regions of the flow domain. It is seen that the strain rate fields initially experience variations in the flow upstream of the screw tip. At this point, the shear strain rate for all three streamlines is much higher than that of the normal strain rate. Hence, the resulting shear-dominate flow directs the principle orientation direction near the screw ending position as shown in Figures 5-8 and 5-9. In addition, it can be seen that the A_{33} component of the swirling flow in Figure 5-9 decreases considerably and then recovers to a high value as polymer melt passes through the shear dominated nozzle convergent zone. Specifically, the larger the shear strain rate is, the more significant changes the diagonal components of the orientation tensor experiences. For instance, the magnitude of the shear strain rate of streamline 15 is higher than that of streamline 8, and thus the change (e.g. decreasing) of A_{33} component along streamline 15 is much more significant than that along streamline 8, as shown in Figure 5-9. Alternatively, the normal strain rate of streamline 1 is higher than its shear strain rate magnitude, and thus the relatively higher elongational effects of the flow increases the A_{33} component of streamline 1. Finally, as the flow exits the nozzle, the normal strain rate of streamline 1 and 8 increase significantly while that of streamline 15 decreases. The positive elongation flows in streamline 1 and 8 increase the fiber alignment along flow direction while the negative elongation decreases the A_{33} component in streamline 15. As the melt flow exits the nozzle, the shear strain rate fields (e.g., $||\frac{dv_t}{de_n}||$) of all three selected streamlines experience a significant decrease and then vanish to zero, which causes the diagonal components of the orientation tensor become constant. This variation causes the A_{33} component of the swirling flow at the nozzle exit decreases greatly and

then recovers somewhat. In detail, the change of the A_{33} component along streamline 15 is most significant among the three selected streamlines due to its relatively high magnitude of strain rate as seen through Figures 5-11B, 5-12B, and 5-13B.

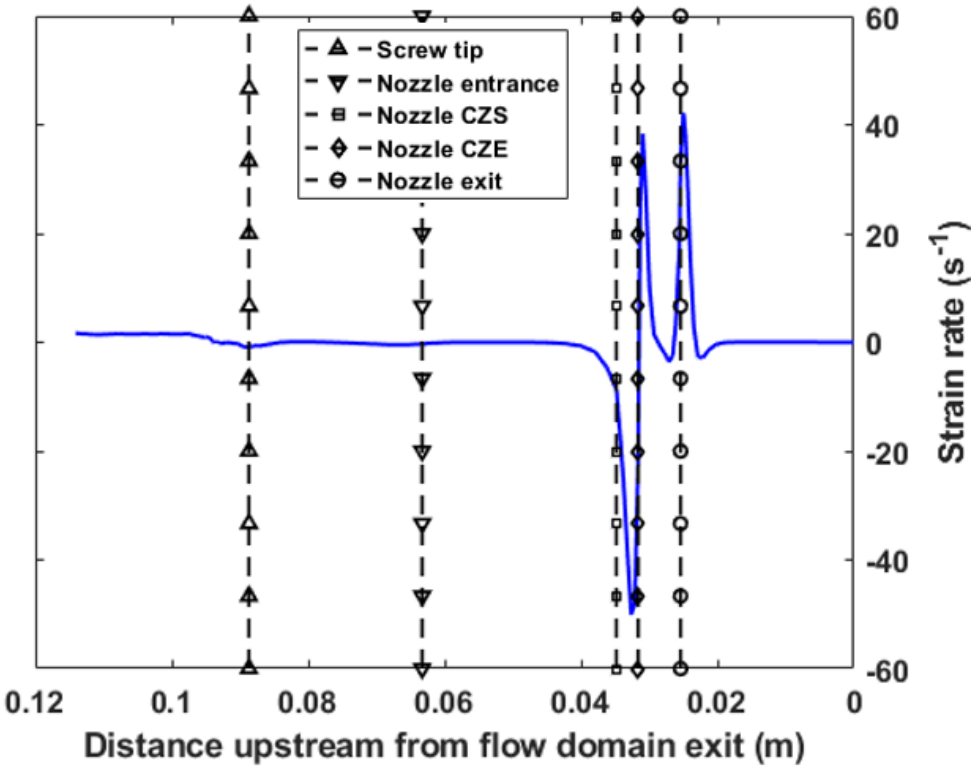

(A)

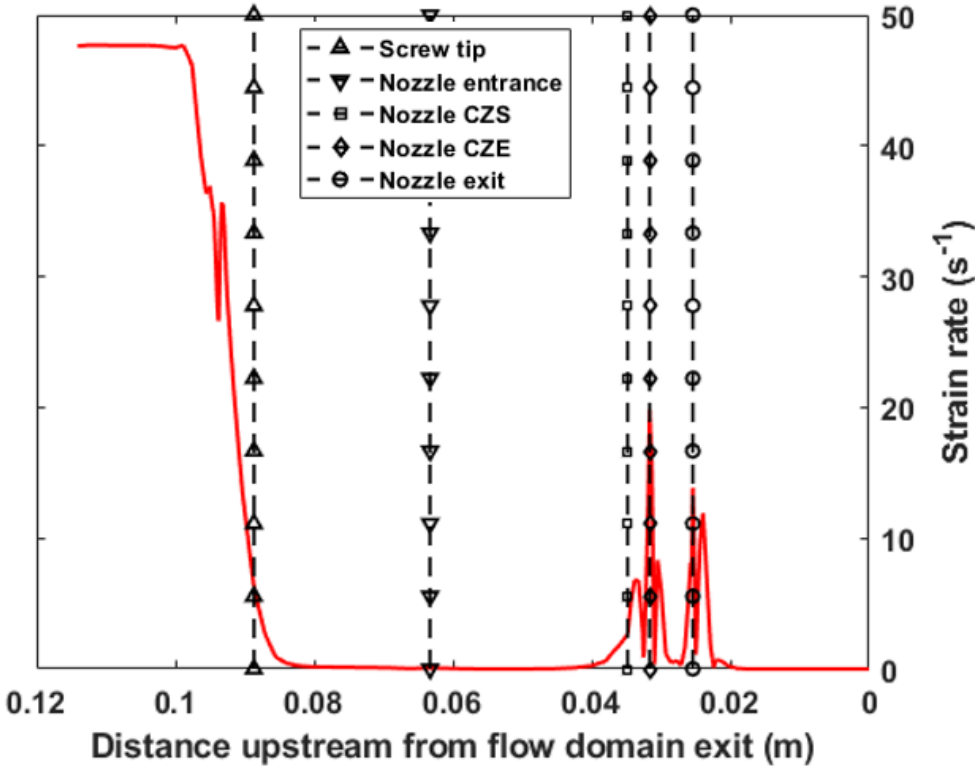

(B)

Figure 5-11. Swirling Flow Strain Rate Fields in Tangential-Normal Frame for Streamline 1: (A) Normal Strain Rate; (B) Magnitude of Shear Strain Rate.

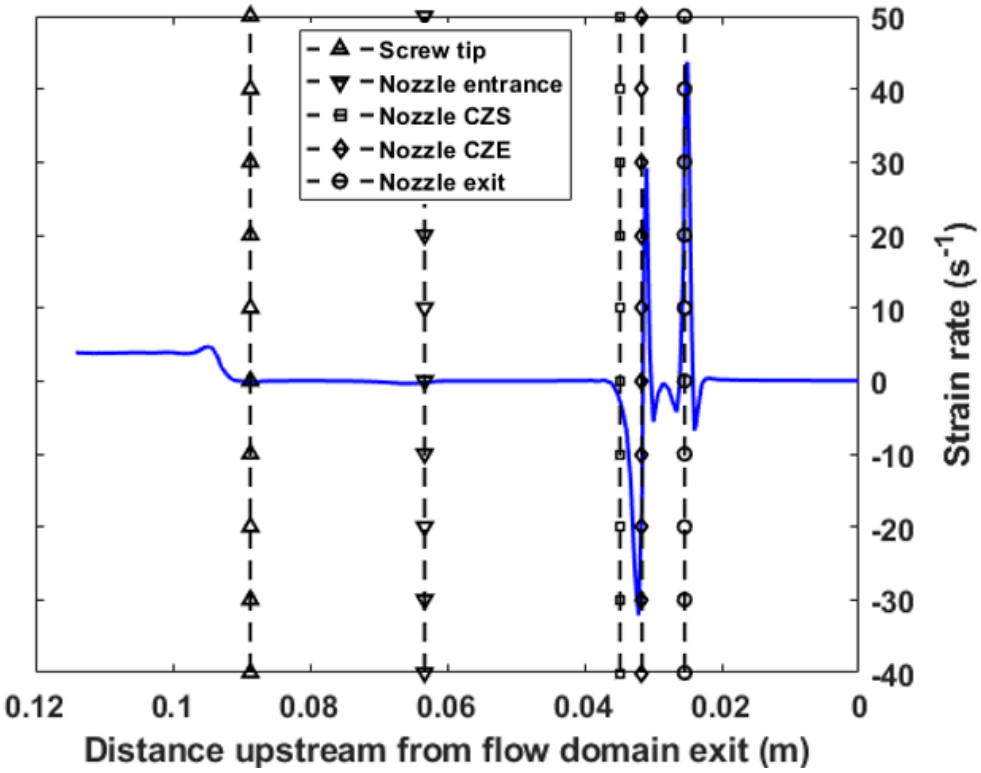

(A)

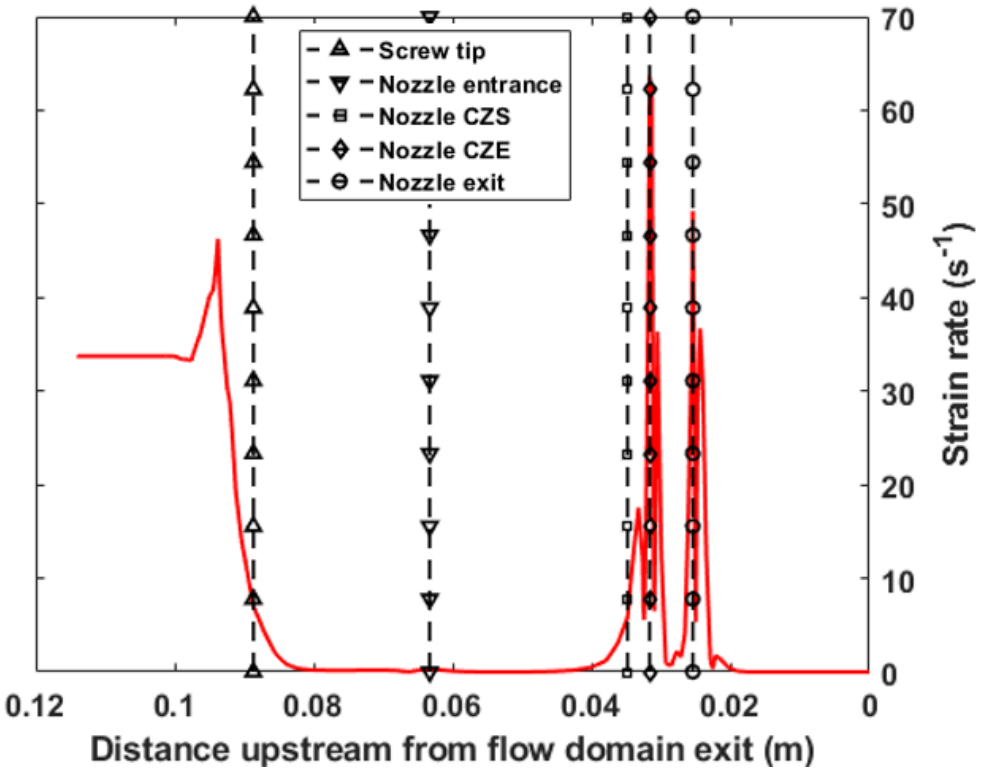

(B)

Figure 5-12. Swirling Flow Strain Rate Fields in Tangential-Normal Frame for Streamline 8: (A) Normal Strain Rate; (B) Magnitude of Shear Strain Rate.

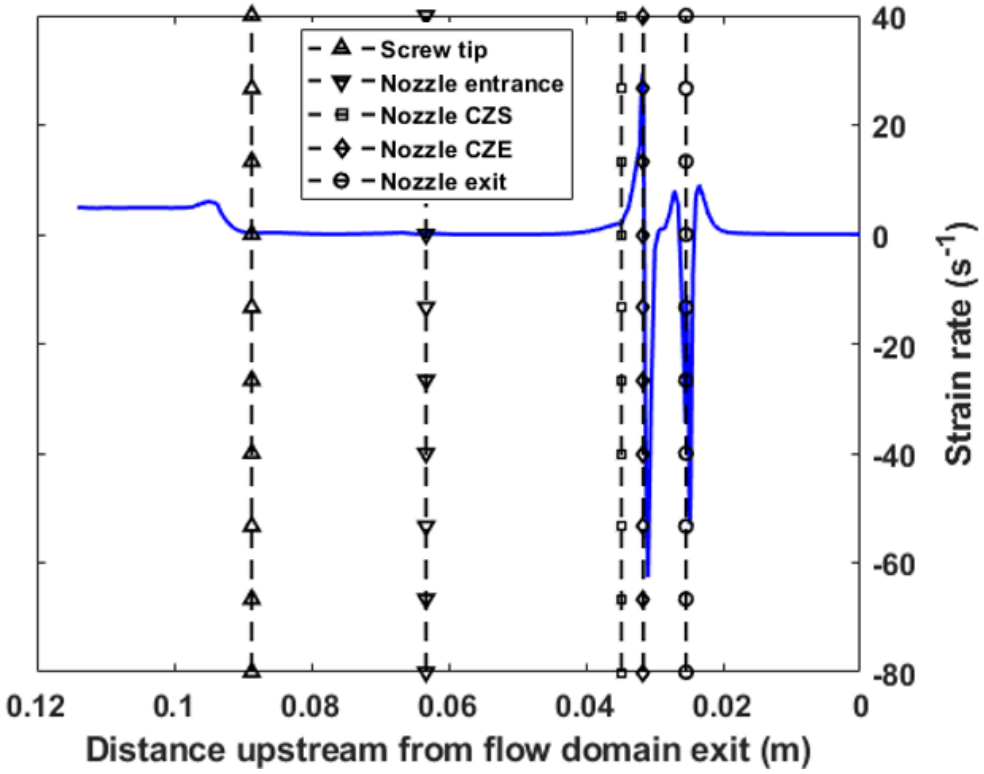

(A)

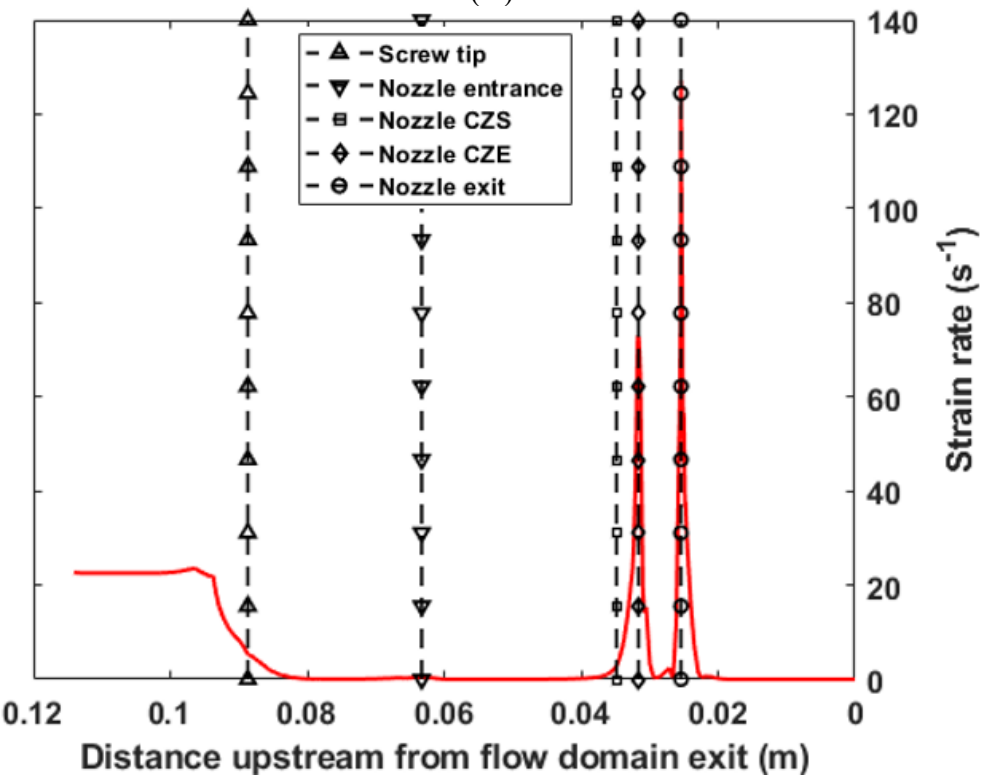

(B)

Figure 5-13. Swirling Flow Strain Rate Fields in Tangential-Normal Frame for Streamline 15: (A) Normal Strain Rate; (B) Magnitude of Shear Strain Rate.

5.3.4 Predicted Effective Elastic Constants

Once fiber orientation values are computed downstream of the nozzle at the flow exit, steady state fiber orientation tensors may be computed for both the straight and swirling flow models to better understand the effect of swirling kinematics on bead elastic properties. Figure 5-14 shows computed values of the orientation tensor diagonal components for each streamline at the flow end. It is expected that the fiber orientation will attain a steady state orientation prior to reaching the flow end which is, therefore, assumed to represent the fiber orientation within the solidified extruded polymer composite as in Chapter Four examples. From the data appearing in Figure 5-14, it can be seen that the fiber alignment along the flow direction is higher than those along transverse directions for both the straight flow and swirling flow. which agrees with trends seen in prior experimental [12, 103] and numerical studies [19, 55]. However, the fiber orientation pattern differs along the radial direction of the bead when comparing the swirling flow and the straight flow results. For the swirling flow results, it is seen that the A_{33} component increases slowly from the outer boundary toward the core of the flow, and the results of the straight flow decreases initially after leaving the outer boundary and then increases after the intermediate region of the flow. In addition, the A_{33} component of the swirling flow is higher than that of the straight flow, over the entire flow exit.

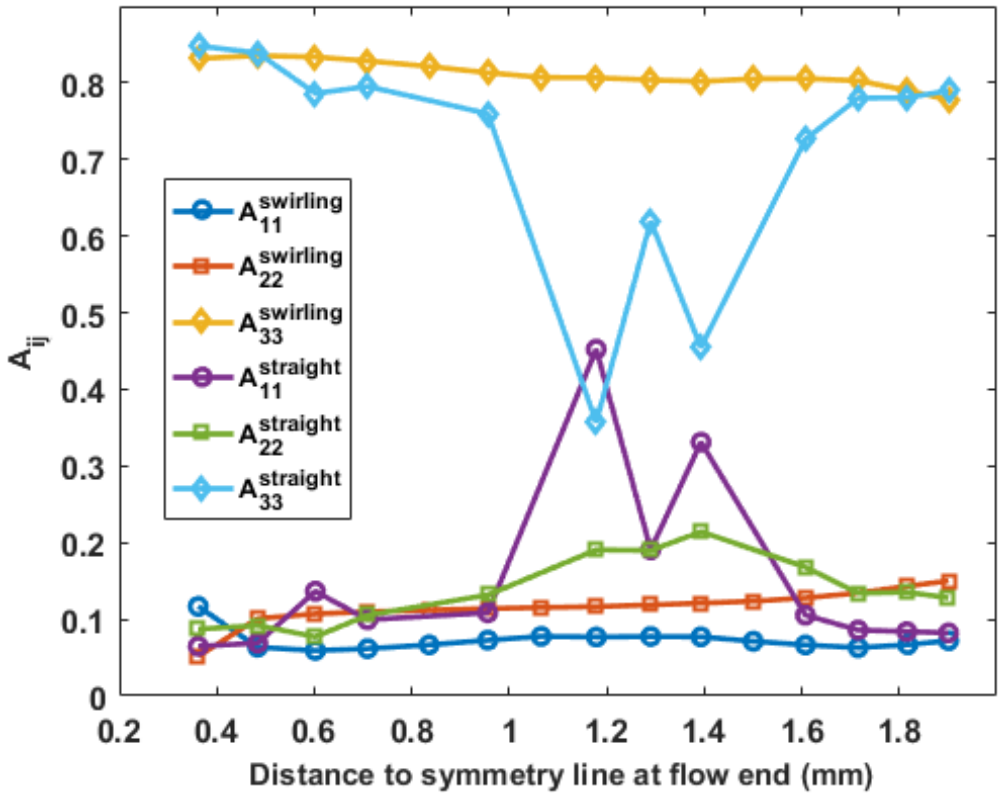

Figure 5-14. Steady State Orientation Tensor Diagonal Components at Streamlines Ends.

The effect of the swirling flow on the material properties of an extruded bead may be considered by computing elastic properties with the orientation homogenization method describe in Section 3.4. The material stiffness of a 13% CF-ABS composite is evaluated based on the steady-state orientation tensor components appearing in Figure 5-14. For the material model of 13 % wt. CF-ABS (supplied by PolyOne Corp.), in which the fiber volume faction of the composite is assumed to be 8.4 % and the fiber aspect ratio used in the stiffness computation is 40, as did in Chapter Four. The constituents material properties of the composite is given in Table 4-5. Ultimately, computed mean elastic properties are given through Table 5-2. From the given results, it is seen that the mean elastic constant $\bar{E}_{33}$ in the flow direction is much higher than those along transverse directions for both the swirling flow and the straight flow simulation cases, as expected,

which is due to the high principal fiber alignment along the flow direction. Specifically, the $\bar{E}_{33}$ value predicted by applying a swirling flow exhibits a significant increase of 24.5% comparing to the same property predicted by using a straight flow, which demonstrates that the screw swirling has a considerable effect on fiber alignment pattern within an extruded polymer composite bead.

Table 5-2. Computed Mean Elastic Constants of a 13% CF-ABS Extrudate.

Flow model	$\bar{E}_{11}$ (GPa)	$\bar{E}_{22}$ (GPa)	$\bar{E}_{33}$ (GPa)	$\bar{G}_{12}$ (GPa)	$\bar{G}_{13}$ (GPa)
Swirling Flow	3.10	3.50	9.98	1.11	1.66
Straight Flow	3.47	3.59	8.02	1.25	1.59

Table 5-2. Computed Mean Elastic Constants of a 13% CF-ABS Extrudate (continued).

Flow model	$\bar{G}_{23}$ (GPa)	$\bar{\nu}_{12}$	$\bar{\nu}_{13}$	$\bar{\nu}_{23}$
Swirling Flow	1.29	0.45	0.37	0.40
Straight Flow	1.62	0.41	0.41	0.40

In addition, prior literature experimentally reported the tensile modulus of a 13% CF-ABS in the print bead direction (e.g., $\bar{E}_{33}$ appearing in Table 4-2) is around 7-9 GPa [12, 25, 103], and our reported $\bar{E}_{33}$ value from the two flow models are 8-9 GPa which shows a favorable agreement with the above experimental measurements. Considering that our numerical method does not match the entire experimental procedure and sampled materials in referred literature [12, 25, 103] exactly, the overall favorable comparison with prior corresponding experimental work supports our proposed algorithm.

Finally, our finite element swirling flow model is meshed in 2100 4-node quadrilateral elements with 2217 nodes. Additional models having two different meshes of the same flow domain (not shown here) were also studied. These alternate models included a finer mesh (4745 nodes and 4567 elements) and a coarser mesh (1347 nodes

and 1240 elements) as compared to our intermediate mesh that was used to compute all of the results given above. It is found that the computed results of mean elastic constants $\bar{E}_{11}$, $\bar{E}_{22}$, and $\bar{E}_{33}$ using the flow kinematics solved with the intermediate mesh and the fine mesh are within 1% absolute relative difference [42]. Therefore, we consider the intermediate mesh, that we are currently using, is computationally efficient and reliable for our study, such that a finer mesh will not increase much accuracy but yield considerate computational cost and numerical instability.

CHAPTER SIX

Influences of Fiber Attrition

Properly assessing the material stiffness of polymer composites deposited by the LAAM process is a vital component of establishing the process-structure-property relations for the LAAM technology. While the unique screw extrusion material feeding mechanism of the LAAM yields an uneven distribution of fiber aspect ratio within deposited composites, most conventional micromechanical models assume a single value of fiber aspect ratio in evaluating the elastic properties of composite materials, as was presented in previous chapters of this dissertation. Here, we present a statistics-based method which includes the fiber aspect ratio distribution of an extruded polymer composite into the prediction of extrudate elastic properties hereinafter.

This chapter investigates the effect of fiber aspect ratio distribution on the prediction of effective elastic properties of a composite extrudate processed through the LAAM system. To facilitate the methodology demonstration, we measure the fiber length distribution of a printed bead made of 13% CF-ABS feedstock that has been commonly used for LAAM applications. By assuming the variation of fiber diameter is negligible (e.g. see [104]), the fiber aspect ratio distribution is obtained by diving the measured fiber length values by a constant value of fiber diameter. The Weibull probability distribution function is applied to model the variability in the experimental aspect ratio data. The fiber aspect ratio distribution function is incorporated into a fiber orientation homogenization method to calculate the mean elastic properties of an extruded composite material for a

given fiber orientation state within the extruded composite material, where the fiber orientation state applied in this chapter is the same as that computed in Chapter Five.

The methodology of predicting the elastic properties of extruded polymer composites presented herein is based on the orientation homogenization theory (see e.g., [22, 89]) with the addition of unevenly distributed fiber aspect ratio. This differs from prior work where micromechanics models typically only consider a single value of the fiber aspect ratio as input (e.g., [19, 55]). The following includes the description of the flow domain of interest and the method developed here to compute the fiber orientation state of the flow, the data acquisition procedure of measuring the fiber length distribution of the material samples, and the orientation homogenization method with specific modifications.

6.1 Flow Domain of Interest and Fiber Orientation

Chapter Five shows that the unique swirling kinematics generated from a LAAM single screw extruder may significantly affect the resulting fiber orientation. This chapter includes the screw swirling flow model results of Chapter Five. The geometry of the flow domain includes a short section of the extruder that connects the screw tip, the nozzle portion, and a short strand of a vertical extrudate downstream of the nozzle exit. Due to the axisymmetry of the nozzle geometry and assumed flow, the flow domain is simplified with a 2D axisymmetric model, which saves significant computational expense. The resulting flow domain appears in Figure 5-3. The polymer melt flow modeled in this chapter is simulated using the 5-mode PTT model with parameter values given in Table 5.1 of Chapter Five. The polymer melt flow velocity fields are computed through the finite element suite, ANSYS-Polyflow, where the presence of fibers is not included in the

flow simulation. Applying the weakly coupled formulation, the second order fiber orientation tensors through the flow domain are computed through the RSC model (cf. Equation 3-17) and the orientation tensor values at the flow exit (i.e., orientation tensor values appearing in Figure 5-14) are used this chapter for further evaluation of the effect of fiber length variation on mean elastic properties of the extruded composites.

6.2 Fiber Length Attrition

Previous literature shows that fiber length attrition occurs in LAAM applications (e.g., [37, 38]) while related experimental studies on the fiber length attrition are still limited. To facilitate our study on the effect of fiber aspect ratio distribution on the predicted elastic constants, we quantify the fiber aspect ratio distribution of a 13% CF-ABS material supplied by PolyOne Corporation (Avon Lake, Ohio, USA) following the procedure described below.

Polymer feedstock having 13% CF-ABS is chosen for this research since it is commonly used in large-scale polymer composites deposition additive manufacturing (e.g., see [12, 25, 103]). As described above, several studies have considered fiber breakage during polymer composite injection molding and other screw extrusion processes. Unfortunately, little attention has been given to the material deposition additive manufacturing processes. Jiang and Smith [105] measured the fiber length distribution within a filament and a deposited part, separately, for several commercial feedstock materials of a conventional Fused Filament Fabrication (FFF) printer. Their results (cf. Fig. 20 in [105]) indicated that the FFF filament-based material deposition process has minor effect on fiber length. However, it has been shown that the single screw extrusion process in LAAM reduces fiber length within the reinforced polymers

(see e.g., [37, 38]). Therefore, we first measure the fiber length of short carbon fibers suspended within the CF-ABS material in the pellet feedstock and also in the deposited bead to assess the effect of the single screw extrusion process on fiber length attrition. Our polymer composite material deposition system includes a Strangpresse (Youngstown, OH, USA) Model 19 large-scale single screw extruder, which has a maximum material feed rate up to 20 lbs. per hour. Bead samples in this study are obtained by depositing the composite material with the single screw extruder operating at 80 RPM (which equates to a mass flow rate of ~8-9 lbs./hour for 13% CF-ABS) at 215℃. To measure the dimensions of fibers, we remove the ABS resin from samples through a TA Instruments (New Castle, DE, USA) Q50 Series Thermogravimetric Analyzer (TGA) burn-off procedure, where details appear in Table 6-1.

Table 6-1. Customized TGA burn-off test procedure.

Step Number	Procedure
1	Preparing pellet sample (or deposited bead sample)
2	Ramp 10.00 °C/min to 600.00 °C
3	Isothermal for 60.00 min
4	Finish test and cool down the chamber

Following the burn-off process in Table 6-1, each test sample is mixed with purified water solvent, and then fibers are dispersed without damage using a Branson Ultrasonic (Danbury, CT, USA) 250 Digital Sonifier. The treated fiber suspension solution is then dried in a 3 inch diameter by 0.5 inch high petri dish in a Thermo Scientific (Waltham, MA, USA) BlueM oven at 60 ℃ for 8 hours. Finally, the dried sample contained inside the petri dish is imaged with a Keyence (

Prefecture, Japan) VR-3000 digital optical microscope to measure the length of individual fibers. The complete experimental procedure flowchart appears in Figure 6-1.

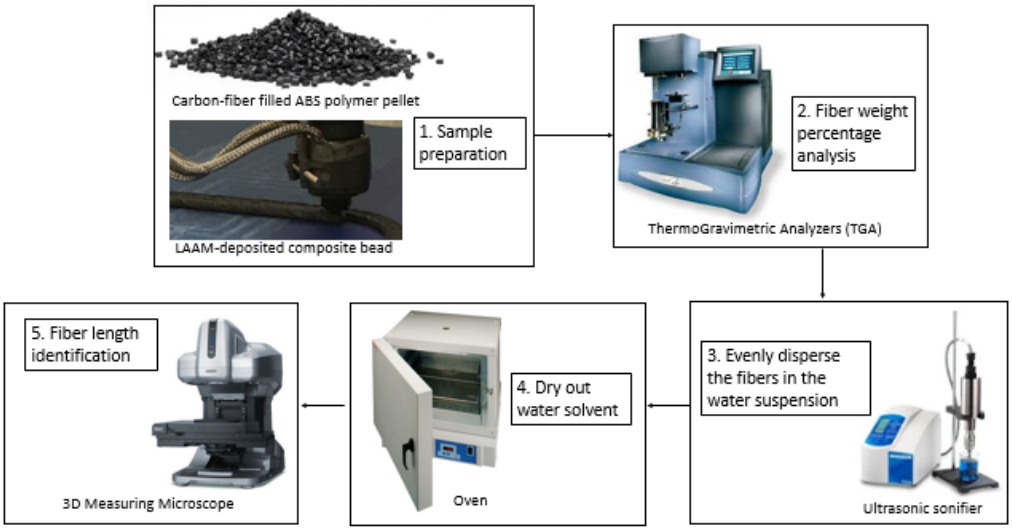

Figure 6-1. Schematic Fiber Length Measurement Procedure.

6.3 Statistical Modelling

Suspended fibers within the thermoplastic polymer composite break during extrusion due to shear stresses produced by the extruder screw which reduces the mean fiber length. The resulting fiber length distribution has been shown to be asymmetric where a tail in the distribution propagates towards high fiber lengths [106]. Ularych, et al. [107] described the fiber length distribution for a glass fiber polypropylene using a two-parameter Weibull probability distribution function (i.e., $\mathcal{F}(x)$, with x as the independent variable) which can be written as (also see Fu, et al. [108])

$$\mathcal{F}(x|k^w,\lambda^w) = \frac{k^w}{\lambda^w}\left(\frac{x}{\lambda^w}\right)^{k^w-1} exp\left[-\left(\frac{x}{\lambda^w}\right)^{k^w}\right], \tag{6-1}$$

where k^w and λ^w are shape and scale parameters for the Weibull distribution function, respectively. Fu, et al. [108] proposed a set of formula to calculate the most probable

length (mode length, or $\tilde{x}$) and the number average fiber length (mean length, or $\bar{x}$) from a set of fiber lengths as

$$\bar{x} = \int_0^{\infty} x\, \mathcal{F}(x) dx = \lambda^w\, \Gamma\left(\frac{1}{k^w} + 1\right), \tag{6-2}$$

and

$$\tilde{x} = \left[(\lambda^w)^{k^w} - \frac{1}{(\lambda^w)^{-k^w}\,(k^w)}\right]^{1/k^w}, \tag{6-3}$$

where Γ refers to the gamma function. In this study, we use the "wblpdf" function provided by MATLAB 2018a [109] (The Mathworks, Natick, Massachusetts, USA) to compute the parameters of a Weibull distribution function for set of measured fiber length data obtained through the experimental procedure described above.

6.4 Orientation Homogenization Evaluation of Stiffness of Composite Materials

Numerical predictions of mechanical performances of a composite material have been shown to be very useful for researchers and engineers in the design of composite structures and tooling. Unfortunately, all prior studies employ a single value of fiber aspect ratio when calculating the elastic properties of LAAM-printed composite material (e.g., see [19, 55], and our previous studies in Chapter Four and Five). To better understand the influence of fibers having variable length, we develop a new approach that incorporates the fiber aspect ratio distribution into the orientation homogenization approach (e.g., see [22, 89]) to estimate the material stiffness of the extruded polymer composite, where the effects of flow-induced fiber orientation and extrusion-influenced fiber attrition aspect ratio distribution are both considered. Specifically, the distribution of fiber aspect ratio is obtained by dividing measured fiber length distribution by a

constant fiber diameter, which assumes the fiber diameter is not significantly affected by the fiber length attrition and it is constant prior to extruder processing.

6.4.1 Unidirectional Aligned Fiber Reinforced Composites

Micromechanical models of unidirectional fiber reinforced composites have been developed over the past few decades as composite materials make up an increasing share of engineering material market. Mori and Tanaka [110] proposed a method to evaluate the stiffness for non-dilute composite materials and Laws and McLaughlin [111] extended the self-consistent method initiated by Hill [112] and Budiansky [113] for evaluating aligned short fiber reinforced composite stiffness. The Halpin-Tsai equations [114], which are derived from continuous fiber filled composite models [112, 115], have seen much application (e.g., [116, 117]) for predicting elastic properties of discontinuous short fiber composites. Tandon and Weng [87] extended the Mori-Tanaka method to obtain a set of equations for computing the stiffness of unidirectional short fiber composites. Tucker and Liang [88] assessed several micromechanics theories with the finite element method and concluded that predictions using Mori-Tanaka's approach are most applicable to short perfectly aligned fibers in regular arrangements. In a manner similar to earlier related works [89], unidirectional composite stiffness predictions are used as a basis in the orientation averaging approach described below. To this end, we employ the Tandon-Weng [87] formulas to first evaluate the stiffness of a unidirectional aligned fiber filled composite. The detail of the formula is presented in Appendix Part A and is not given explicitly here for conciseness.

6.4.2 Fiber Reinforced Composite with Specific Fiber Orientation

As shown in Figure 6-2, the orientation homogenization approach (e.g., see [22, 89, 118]) is used here to predict the mean stiffness of a short fiber polymer composite that has a known fiber orientation distribution (e.g., that which has resulted from a LAAM process simulation). The homogenization approach decomposes the composite into a set of subdomains of uniaxially aligned fibers with the same concentration of fibers as the representative volume. Following the Voigt procedure (where the mean strain is assumed constant over a subdomain), Jack and Smith [89] write the sample mean material stiffness tensor $\tilde{Y}_{ijkl}$ of each subdomain from the corresponding fiber stress field as

$$\tilde{Y}_{ijkl} = \frac{1}{N}\sum_{n=1}^{N}\left[Q_{qi}^{c}(\varphi_n,\phi_n)Q_{rj}^{c}(\varphi_n,\phi_n)Q_{sk}^{c}(\varphi_n,\phi_n)Q_{tl}^{c}(\varphi_n,\phi_n)\bar{C}_{qrst}^{uni}\psi(\varphi_n,\phi_n)\right], \quad (6\text{-}4)$$

In the above, $i,j,k,l,q,r,s,t \in \{1,2,3\}$. In Equation 6-4, $Q_{ij}^{c}(\varphi,\phi)$ is the rotation tensor that can be written as

$$Q_{ij}^{c}(\varphi,\phi) = \begin{bmatrix} sin\varphi\ cos\phi & sin\varphi\ sin\phi & cos\varphi \\ -sin\phi & cos\phi & 0 \\ cos\varphi\ cos\phi & cos\varphi\ sin\phi & sin\varphi \end{bmatrix}, \quad (6\text{-}5)$$

In the above, the fourth-order tensor $\bar{C}_{qrst}^{uni}$ is the material stiffness tensor of a reference unidirectional composite computed using the Tandon-Weng equations as described above [87] and in Appendix Part A. The Q_{ij}^{c} is used to rotate a sample fiber from its local coordinates where the $\bar{C}_{qrst}^{uni}$ is computed to the global coordinate system (cf. first homogenization appears in Figure 6-2). Note, the sample mean material stiffness tensor $\tilde{Y}_{ijkl}$ is an unbiased estimator (see, e.g., [119]) of the population mean for a given distribution [89]. For a specific set of angles (e.g., $\{\varphi,\phi\}$), as $N \to \infty$, the sample mean

stiffness tensor approaches to the expected value, or the point-wise mean stiffness tensor of a subdomain, $\check{C}_{ijkl}$, such that

$$\check{C}_{ijkl} = \oint_{\mathbb{S}^2} Q^c_{qi}(\varphi,\phi) Q^c_{rj}(\varphi,\phi) Q^c_{sk}(\varphi,\phi) Q^c_{tl}(\varphi,\phi) \bar{C}^{uni}_{qrst} \psi(\varphi,\phi)\, d\mathbb{S}, \tag{6-6}$$

Aside from the above derivation, Jack and Smith [89] showed that the mean stiffness $\check{C}_{ijkl}$ appearing in Equation 6-6 can be evaluated using the second and fourth order orientation tensor of A_{ij} and A_{ijkl} (also given in Advani and Tucker [22]) as

$$\begin{aligned}\check{C}_{ijkl} = M_1 A_{ijkl} + M_2\left(A_{ij}\delta_{kl} + A_{kl}\delta_{ij}\right) + M_3\left(A_{ik}\delta_{jl} + A_{il}\delta_{jk} + A_{jl}\delta_{ik} + \right. \\ \left. A_{jk}\delta_{il}\right) + M_4 A_{ij}\delta_{kl} + M_5\left(A_{ik}\delta_{jl} + A_{il}\delta_{jk}\right),\end{aligned} \tag{6-7}$$

where material constants M_I, I = 1,…,5 are computed from

$$M_I = \begin{Bmatrix} C_{11} + C_{22} - 2C_{12} - 4C_{66}, & \text{for } I = 1 \\ C_{12} - C_{23}, & \text{for } I = 2 \\ C_{66} + (C_{23} - C_{22})/2, & \text{for } I = 3 \\ C_{23}, & \text{for } I = 4 \\ (C_{22} - C_{23})/2, & \text{for } I = 5 \end{Bmatrix}, \tag{6-8}$$

In the above, C_{ij} are components of the stiffness tensor for the associated unidirectional fiber filled composite (i.e., $\bar{C}^{uni}_{qrst}$) written in contracted notation, which we compute using the Tandon-Weng micromechanics model as did in previous chapters [87].

It is common to assume a constant value for the fiber aspect ratio in the numerical evaluation of $\bar{C}^{uni}_{qrst}$ when applying the Tandon-Weng model (cf. Appendix A) to short fiber composite materials which neglects any variation in geometric fiber aspect ratio. In contrast, we include the effect of fiber aspect ratio distribution within the printed composite material in the derivation below.

Notice that given a specific fiber aspect ratio, a material stiffness tensor $\bar{C}^{uni}_{qrst}$ may be computed. Then, the mean stiffness tensor is evaluated as

$$\check{C}_{ijkl}^{a_r} = \oint_{\mathbb{S}^2} Q_{qi}^{c}(\varphi,\phi) Q_{rj}^{c}(\varphi,\phi) Q_{sk}^{c}(\varphi,\phi) Q_{tl}^{c}(\varphi,\phi) \bar{C}_{qrst}^{uni}(a_r) \psi(\varphi,\phi)\, d\mathbb{S}, \tag{6-9}$$

Recall, in polymer sciences, the number average polymer molecular weight of a polymer is computed through [120]

$$\overline{M}^{N} = \frac{\int_0^{\infty} N(M) M dM}{\int_0^{\infty} N(M) dM}, \tag{6-10}$$

where *M* is the weight of one molecule, and *N(M)* stands for the molecular-weight distribution function for *M*. Equation 6-10 indicates an approach to estimate the expected mean value of *M(M)* (e.g., in Equation 6-10, *M(M) = M*) that has a distribution function *N(M)*. Applying the a similar form as appearing in Equation 6-10, we express the number average mean stiffness tensor out of $\check{C}_{ijkl}^{a_r}$ as

$$\check{C}_{ijkl}^{\overline{a_r}^{N}} = \frac{\int_0^{\infty} \left[\mathcal{F}(a_r) \check{C}_{ijkl}^{a_r}\right] da_r}{\int_0^{\infty} [\mathcal{F}(a_r)] da_r}, \tag{6-11}$$

Furthermore, we recast Equation 6-7 as a function of the fiber aspect ratio, such that

$$\begin{aligned} \check{C}_{ijkl}^{a_r} = {} & M_1(a_r) A_{ijkl} + M_2(a_r)\left(A_{ij}\delta_{kl} + A_{kl}\delta_{ij}\right) + M_3(a_r)\left(A_{ik}\delta_{jl} + A_{il}\delta_{jk} + \right. \\ & \left. A_{jl}\delta_{ik} + A_{jk}\delta_{il}\right) + M_4(a_r) A_{ij}\delta_{kl} + M_5(a_r)\left(A_{ik}\delta_{jl} + A_{il}\delta_{jk}\right), \end{aligned} \tag{6-12}$$

where $M_i(a_r)$ are evaluated through Equation 6-8, that depending on the results of $\bar{C}_{qrst}^{uni}(a_r)$. In other words, given a value of a_r, we can compute a set of $\bar{C}_{qrst}^{uni}(a_r)$, i.e., $M_i(a_r)$ as well. We then evaluate the $\check{C}_{ijkl}^{a_r}$ appearing in Equation 6-11 through Equation 6-12. It follows that since the integral of $\int_0^{\infty} [\mathcal{F}(a_r)] da_r$ is one and we finally obtain

$$\check{C}_{ijkl}^{\overline{a_r}^{N}} = \int_0^{\infty} \left\{\mathcal{F}(a_r) [\check{C}_{ijkl}^{a_r}(a_r)]\right\} da_r\,, \tag{6-13}$$

to evaluate the number average mean stiffness tensor at a material point within the composite material with known orientation tensor values. In the above, $\mathcal{F}(a_r)$ is the

Weibull distribution function that describes the probability of a_r (cf. Equation 6-1) that we fit from experimental measures as described above.

The molecular weight computation in polymer science can be also quantified in a sense of weight-average, such that [120]

$$\bar{M}^N = \frac{\int_0^\infty N(M)M^2\,dM}{\int_0^\infty N(M)M\,dM}, \tag{6-14}$$

It is reasonable that the longer fibers within a composite material (e.g., the highest 20% of the Weibull distribution function) play a more important role in defining the elastic properties of the material than those with much shorter dimensions (e.g., the lowest 20% of the Weibull distribution function). To this end, we propose an additional expression of the mean stiffness tensors, where longer fibers are weighted more than the shorter ones, such that

$$\check{C}_{ijkl}^{\overline{a_r}^W} = \frac{\int_0^\infty \left\{\mathcal{F}(a_r)\left[\check{C}_{ijkl}^{a_r}(a_r)\right]^2\right\} da_r}{\int_0^\infty \left\{\mathcal{F}(a_r)\left[\check{C}_{ijkl}^{a_r}(a_r)\right]\right\} da_r} \tag{6-15}$$

where $\check{C}_{ijkl}^{\overline{a_r}^W}$ refers to a weight average mean stiffness tensor of a material point within the composite that has a fiber aspect ratio distribution of $\mathcal{F}(a_r)$ and known orientation tensor values. This concludes the derivation of our proposed orientation homogenization method with a consideration of the fiber aspect ratio distribution. To reduce the confusion, we summarize the stiffness tensor related variables that used above in Table 6-2.

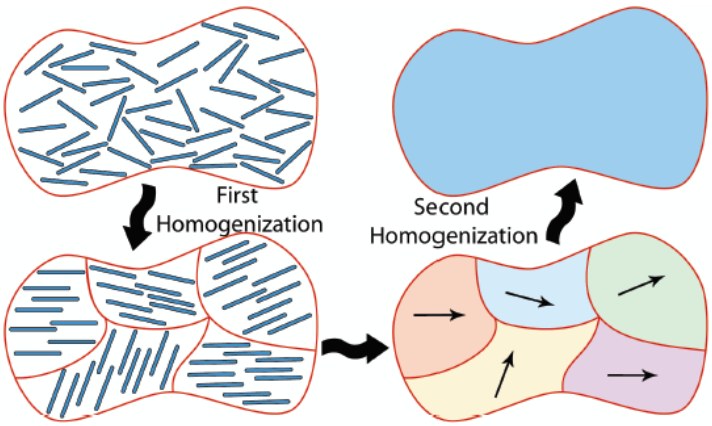

Figure 6-2. Grain Model Two Step Homogenization Procedure. Notice, the Derivation Appearing above Associated with the First Homogenization. The Second Homogenization is Applied to where Several Places with Different Orientation States Are to Be Integrated (cf. Equation 4-15).

Table 6-2. Definitions of Stiffness Tensor Appearing in This Section.

Variable	Definition
$\bar{C}^{uni}_{qrst}$	Stiffness tensor of a reference unidirectional composite
$\check{C}_{ijkl}$	Material point mean stiffness tensor of a subdomain inside a composite, that has a specific orientation distribution function
$\check{C}^{a_r}_{ijkl}$	$\check{C}_{ijkl}$ assuming a single value of a_r
$\check{C}^{\overline{a_r}^N}_{ijkl}$	Number-averaged $\check{C}^{a_r}_{ijkl}$ for a distribution function of a_r
$\check{C}^{\overline{a_r}^W}_{ijkl}$	Weight-averaged $\check{C}^{a_r}_{ijkl}$ for a distribution function of a_r
$\bar{C}_{ijkl}$	Bead-wise mean stiffness tensor of a composite with specific orientation distribution (see e.g., Equation 4-15 for evaluation method)

It is important to note that the fiber aspect ratio plays a key role in the computation in the second-order orientation tensor through the coefficient λ_{a_r} appearing in, e.g., the RSC model (cf. Equation 3-17). Fortunately, as the fiber aspect ratio approaches a value of 1, the effect of λ_{a_r} becomes somewhat trivial in determining the fiber orientation state. In this study we assume that the effect of the fiber aspect ratio distribution on computed fiber orientation with Equation 3-17 is negligible. Therefore, we assume that the solution obtained from Chapter Five, where the parameter of λ_{a_r} is fixed at unity (as in [56]) may be used here for fiber orientation tensor prediction.

Additionally, we assume that the probability of the aspect ratio distribution is independent of location within the extrudate and the entire bead shares the same fiber length distribution function, which may likely be obtained due to an efficient compound mixing from the LAAM single screw extruder feeding mechanism. With this assumption, we are to apply same fiber length distribution results on different positions locally over the end of the extrudate.

6.5 Results and Discussion

Computed values of the mean stiffness tensors for a LAAM-extruded polymer composites including the effect of a statistical distribution of fiber aspect ratio are presented below. The measured fiber attrition length distribution of our 13% CF-ABS carbon fibers appears first. Several statistical models are employed to reflect the statistical nature of the measurements. Finally, the elastic properties of a 13% CF-ABS extrudate are predicted through the orientation homogenization theory where we employ different fitted statistical data.

6.5.1 Fiber Length Attrition

The geometric aspect ratio of cylindrical fibers suspended within a thermoplastic polymer composite material is the length-to-diameter ratio (i.e., $a_r = \mathrm{L_f}/\mathrm{D_f}$, where $\mathrm{L_f}$ and $\mathrm{D_f}$ are length and diameter of a cylindrical fiber, respectively). For short rigid fibers, prior works [37, 38] considered the degradation of fiber length as a pronounced result of damage incurred while traveling through the screw-extrusion mechanism. On the other hand, we note here the applicability of the non-affected fiber diameter assumption is the prerequisite and foundation of our data acquisition for the fiber aspect ratio distribution.

Russell and Jack [104] measured the fiber diameter of 13% CF-ABS processed through a single screw extruder and found that the variation on the measured diameter data is statistically insignificant. Hence, it is assumed here that the fiber diameter is a constant in the feedstock pellets provided by the supplier and does not changed as a fiber travels through the LAAM screw extrusion. Therefore, the fiber aspect ratio data can be obtained by dividing the measured fiber length distribution of the prepared samples with a constant measured mean diameter. Specifically, we set the fiber diameter as 7 μm as given by Russell and Jack [104].

In this work, a Keyence VR-3000 Wide-Area 3D Microscopy Measurement System is used to measure fiber length. A typical image of fibers obtained with the VR-3000 microscope appears in Figure 6-3 for both a pellet sample and a bead sample separately. Note, fibers appearing in Figure 6-3 are examples of the fiber residuals that have been post-processed in a petri dish (e.g., see procedure 3,4 and 5 shown in Figure 6-1) under the VR-3000 Microscopy. Upon close inspection of the images in Figure 6-3, it is visually possible to identify that fiber length degrades from the pellet to deposited bead condition.

Fiber length distributions are obtained in this study by measuring the length of 990 fibers in ten separate trials (i.e., 99 fibers are measured in each trial, which is the maximum of VR-3000 for counting fibers in one frozen plot) in both the pellet fiber sample and the bead fiber sample. Sharma, et al. [121] measured 2000 fibers for a 30% wt. carbon fiber filled Polypropylene and validated the reliability of their fiber length distribution measurements. Hence, we count roughly 1000 (half of the measurements done in [121]) fibers' length for getting the length distribution of a 13% wt. (which is

~1/2 of the weight fraction of material used in [121]) carbon fiber filled ABS. Histograms of the measured fiber lengths appear in Figure 6-4, which shows that suspended carbon fibers experience significant breakage during processing. Jiang and Smith [105] showed that fiber length attrition was minimal in conventional filament-based FFF which implies that the FFF material deposition process does not degrade fiber length. Thus, it is reasonable to attribute the fiber length reduction appearing in Figure 6-4 as a result of the material transport mechanism of the LAAM single screw extruder.

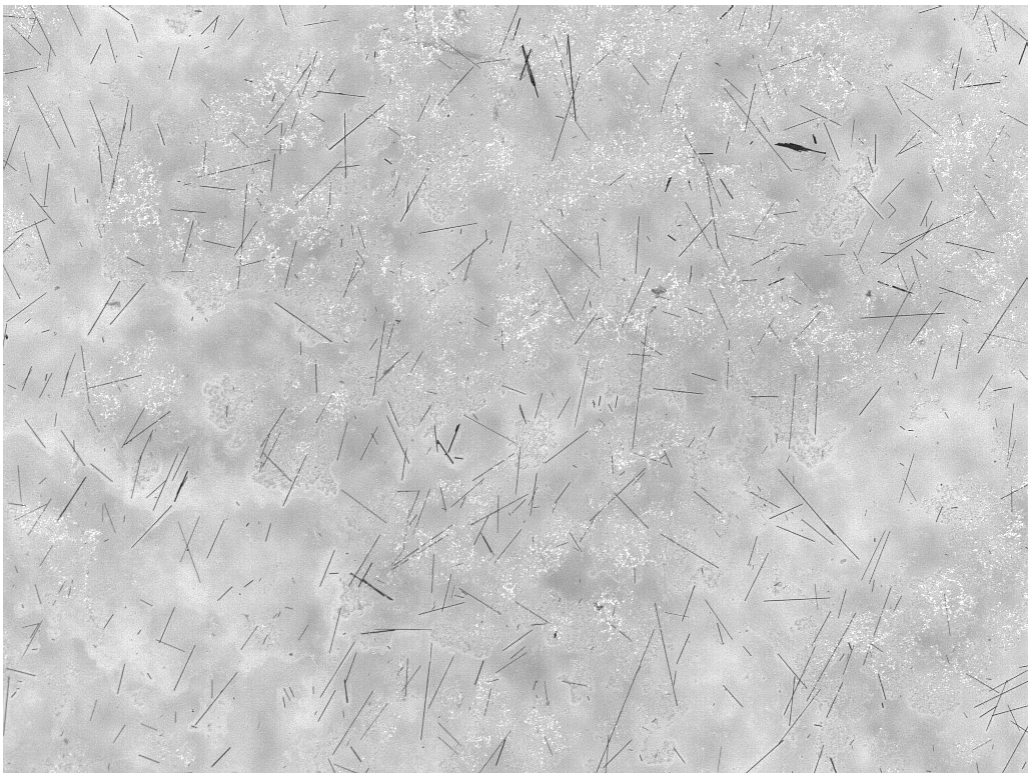

(A)

(B)

Figure 6-3. Images of Fibers Obtained Using a VR-3000 Microscopy for: (A) Pellet Sample; (B) the Bead Sample. (Resolution Specification: High Resolution Cam. ×40)

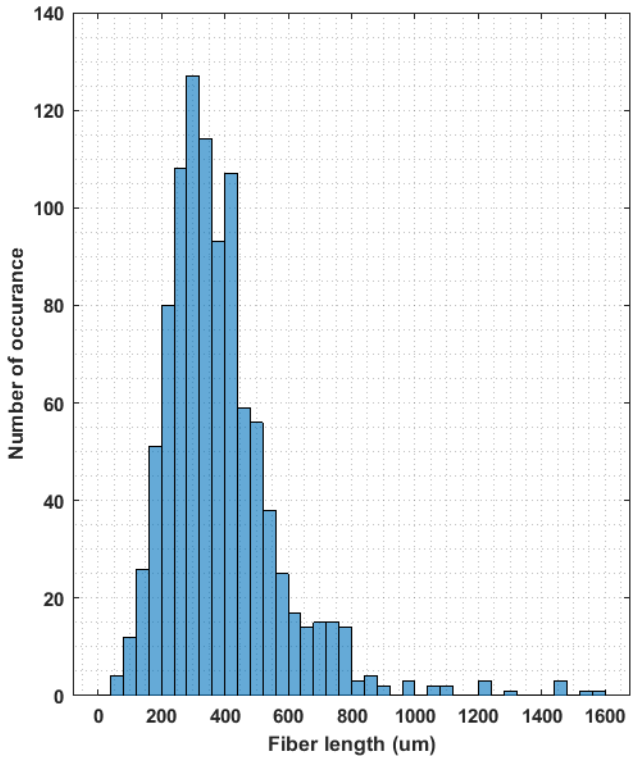

(A)

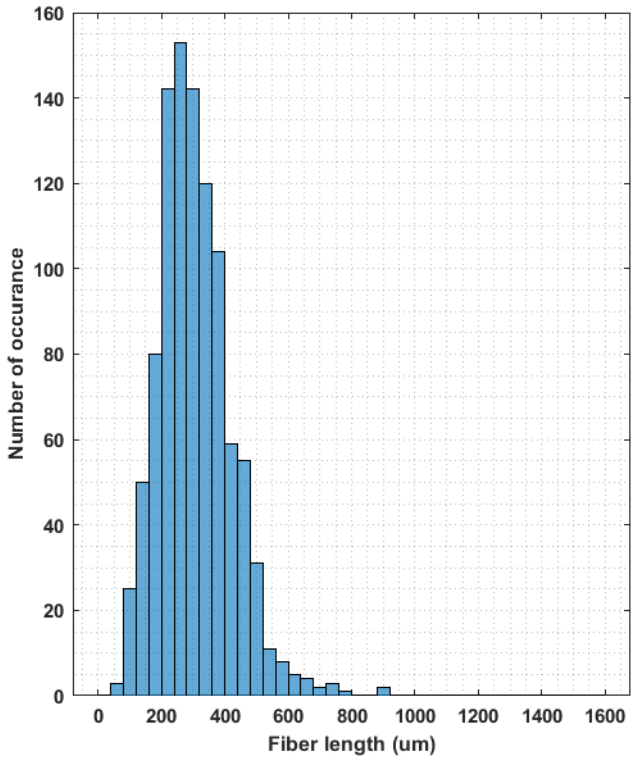

(B)

Figure 6-4. Histograms of Fiber Length Data Measured for Fibers from: (A) Pellet Sample; (B) Bead Samples.

Note that the size of the view (i.e., picture size appearing in Figure 6-3) for fiber length measurements can yield significant bias into the resulting distribution data. As shown in Figure 6-5A, if the sampling view is very large, the longer fibers (labelled in red) are typically chosen more than the smaller alternatives since the larger pieces are easier to be identified by nature. On the contrary, if a small observation region is adopted, the short fibers can be easily chosen while longer fibers may be cut off by a significant amount and ultimately ignored as shown in Figure 6-5B. Consequently, the final resulting length distribution measurement may exhibit a bias as compared to the "true" measurement (i.e., unbiased measurement) if size of a sample region is unproperly chosen. Admittedly, we acknowledged that the size of sampling images adopted in our experimental procedure may yield some bias in measuring the fiber length distribution. Nevertheless, as the main scope of this chapter is to quantify the difference in predicting elastic properties of the LAAM-deposited composites by using a single fiber aspect ratio and a distribution function of fiber aspect ratio values, it can be expected that the data trend generated by our proposed approach (cf. Section 6.4) with current fiber length distribution data would be similar as compared to the event where a potentially less-biased fiber length measurement was performed. The appropriate size of observation region should be specified in a separate in-depth study of fiber length distribution in our future work.

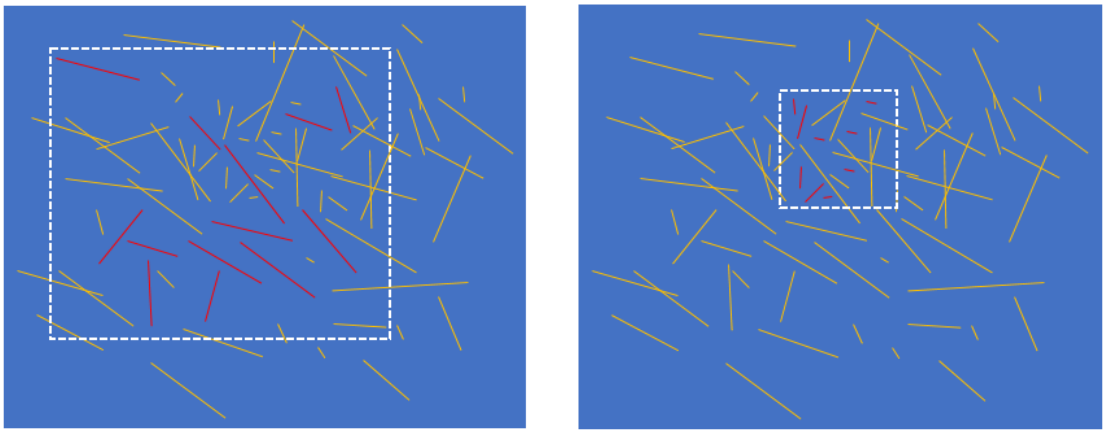

(A) (B)

Figure 6-5. Conceptual Diagram Showing the Bias Generation during Fiber Length Measurements: (A) in Large View; (B) in Small View. Note, the blue region indicates where all fibers are, the white dash-line block is the sampling region. And the red fibers are identified (i.e., counted in a measurement) and the yellow ones are left out.

6.5.2 Fiber Aspect Ratio Distribution

Histograms of fiber aspect ratio of both pellet and bead samples appear in Figure 6-6, where the fiber length data is the same as that given in Figure 6-4 and the fiber diameter of the pellets and beads samples is assumed constant at 7 μm [104]. Employing the Weibull distribution function (cf. Equation 6-1), parameters that define the two sets of measurements are obtained through a curve fitting process (cf. function "fitdist" in MATLAB [109]), where results appear in Figure 6-7 and parameters fitted for the Weibull distribution function are given in Table 6-3. The statistics models appearing in Figure 6-7 make it possible to include the effect of the distributed values of the fiber aspect ratio into the prediction of elastic properties of an extruded polymer composite through the proposed homogenization method in Equations 6-13 and 6-15.

Furthermore, characteristic values of the distributed measurements (i.e., $\overline{a_r}$ and $\widetilde{a_r}$, which are the mean and mode values of the fiber aspect ratio distributions) are evaluated through Equations 6-2 and 6-3 and the results are given in Table 6-4. The

Percent Relative Difference (PRD) [55] (i.e., showing a relative error between two data without bias on either) is employed to assess differences, such that

$$PRD = |x_a - x_b|/(|x_a + x_b|/2) \times 100\% \quad (6\text{-}16)$$

where x_a and x_b are the two data points to be compared. From the measured data, it can be seen that the fiber length attrition is pronounced such that the PRD between the $\overline{a_r}$ values of the pellet and bead results is 23.7%. Moreover, it is seen that the PRD between $\overline{a_r}$ and $\widetilde{a_r}$ values of the fiber aspect ratio distribution of pellet-results is 16.4%, while that of the bead values is only 4.7%. In other words, the skewness of the fiber aspect ratio distributions (i.e., absolute difference between mean and mode values of a distribution) in the bead results is much smaller than that of the pellet results.

In spite of statistical methods, prior studies often employed the direct algebra-averaging schemes to estimate the mean characters of the measurements such that [122]

$$\overline{a_r}^N = \sum n_i \widehat{a_{r_i}} / \sum n_i \text{ , and } \overline{a_r}^W = \sum n_i \left(\widehat{a_{r_i}}\right)^2 / \sum n_i \widehat{a_{r_i}}, \quad (6\text{-}17)$$

where n_i and $\widehat{a_{r_i}}$ denote the number of fibers counted in an individual measurement trial (recall that we performed 10 trials in total) and the mean aspect ratio of that measurement (i.e., sum of the measured fiber length divided by the number of fibers measured), respectively. In the above, $\overline{a_r}^N$, and $\overline{a_r}^W$ refer to the number weighted average and weighted average fiber aspect ratios, respectively. Mean values evaluated through Equation 6-17 are also summarized in Table 6-4, from where it can be seen that the two discrete sample computed results give characteristic fiber aspect ratio values are similar to each other, which fails to provide additional description on the feature of the fiber aspect ratio distribution. Alternatively, statistically obtained characteristic values (i.e., $\overline{a_r}$ and $\widetilde{a_r}$) exhibit a larger difference, especially for the pellet results, which potentially

provides differing results in describing the fiber aspect ratio distribution. Additionally, it is seen that the mean values evaluated through Equation 6-17 are similar to the statistically computed $\overline{a_r}$ through Equation 6-2, which indicates that the statistical fitting is of good quality, in a sense to provide a similar estimation to the mean of a distributed values of fiber aspect ratio. In the following elastic prediction, only the $\overline{a_r}$ and $\widetilde{a_r}$ will be implemented, since the results predicted by $\overline{a_r}^N$, $\overline{a_r}^W$ should be very close to those predicted by applying $\overline{a_r}$ values (cf. Table 6-4).

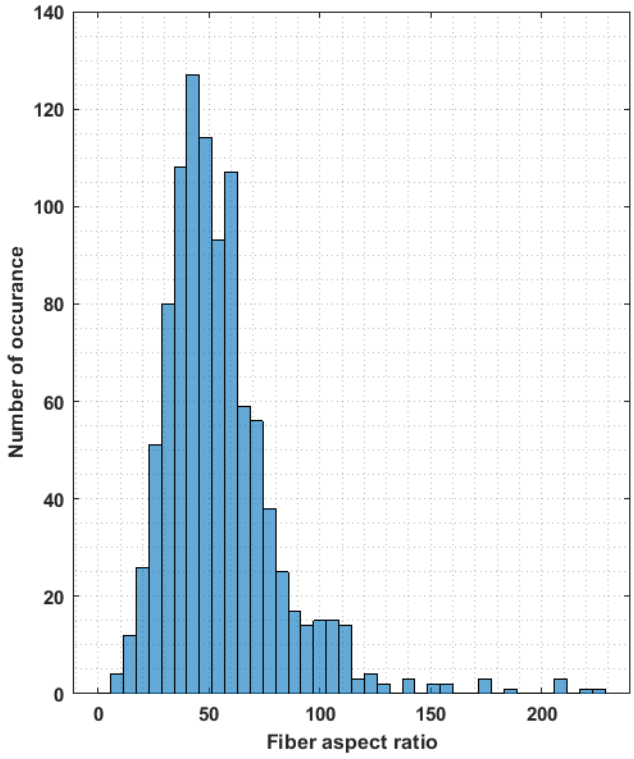

(A)

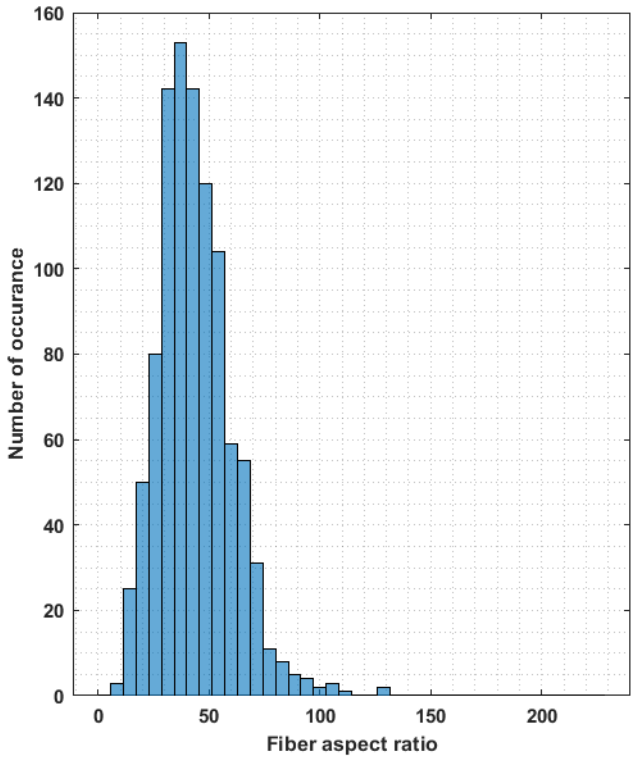

(B)

Figure 6-6. Histograms of Fiber Aspect Ratio Data Measured for Fibers from: (A) Pellet Sample; (B) Bead Samples.

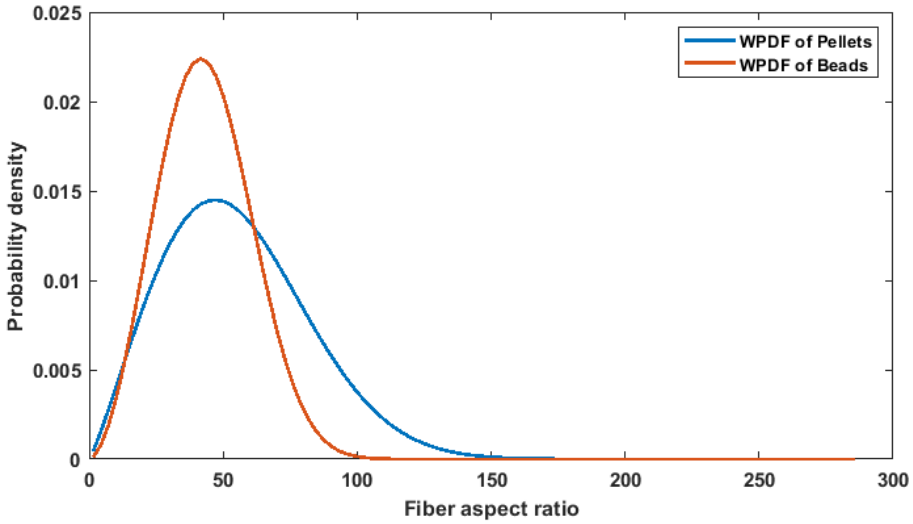

Figure 6-7. Statistical Models of Fiber Aspect Ratio Data for Fibers Obtained from the Pellet sample and the Bead Sample. "WPDF" refers to the Weibull distribution density function.

Table 6-3. Parameters Fitted for the Weibull Distribution Functions.

Sample	λ^w	k^w
Pellet	62.47	2.17
Bead	49.00	2.77

Table 6-4. Mean and Mode Values of the Fiber Aspect Ratio Distribution Functions.

Sample	$\overline{a_r}$	$\overline{a_r}^N$	$\overline{a_r}^W$	$\widetilde{a_r}$
Pellet	55.3	55.3	55.3	46.9
Bead	43.6	43.7	43.7	41.6

Note, $\overline{a_r}$ is the number average mean value of the statistical distribution function results (cf. Equation 6-2, which is similar to that appearing in Equation 6-10 and thus the resulting value is considered as the number average mean).

6.5.3 Elastic Properties Estimation

Prior work in Chapters Four and Five assume a constant value of fiber aspect ratio to evaluate the mean material stiffness of extruded composite materials processed with LAAM. Alternatively, in this chapter, we employ Equations 6-1 (i.e., the Weibull distribution function) to account for the variation in fiber aspect ratio as shown by the

distributions appearing in Figure 6-7. To understand the significance of computing the mean elastic properties using the fiber length distribution, additional computations are performed using a single value of aspect ratio, which are values of $\overline{a_r}$ and $\widetilde{a_r}$ as appearing in Table 6-4. The fiber orientation state of the free extrudate composite end is taken from Figure 5-14 (cf. Chapter Five). The elastic properties of the constitutions for the 13% wt. CF-ABS (v_{frac}=8.4%) considered here are given in Table 4-5 (cf. Chapter Four).

Computed results appearing in Figures 6-8 to 6-10 are mean elastic constants across the extrudate bead of the polymer composite. Note that in the plots, "Pellet results" and "Bead results" imply that the fiber aspect ratio input is obtained from the pellet fiber length distribution results and the bead fiber length attrition distribution results (cf. Figure 6-4), respectively. By comparing the elastic properties predicted from the two sets of measurements, the effects of geometric change of fiber reinforcement during the single screw extrusion process on a printed bead of composite materials can be exposed. In particular, the results of $\overline{a_r}^{N}_{wblpdf}$ and $\overline{a_r}^{W}_{wblpdf}$ are evaluated through Equations 6-13 and 6-15, respectively. And those labelled with $\overline{a_r}$ and $\widetilde{a_r}$ are evaluated through Equation 6-11 in a usual manner as in Chapters Four and Five. From Figures 6-8 to 6-10, it is seen that the properties show local variances across the bead. Among the predicted properties, the most notable difference is seen in the values of E_{33} (i.e., the tensile modulus along the direction of extrusion). Specifically, employing pellet sample measurements and bead sample measurements yields a difference of ~1 GPa in the resulting E_{33} (e.g., $\overline{a_r}^{W}_{wblpdf}$ results predicted using pellet and bead samples separately). In addition, implementing a single mode value of fiber aspect ratio also yields noticeable bias as compared to that predicted using the Weibull distribution function (e.g., bead results of E_{33} between

$\overline{a_r}^{W}_{wblpdf}$ and $\widetilde{a_r}$ is in about ~1 GPa difference). This implies the importance of assessing the fiber aspect ratio on predicting the elastic properties of a LAAM-processed composite bead. It shall be seen more directly in the mean elastic properties estimation in the following.

In addition, we numerically integrate the mean elastic stiffness tensors of an extrudate bead over the cross-sectional area of the extrudate through Equation 4-15 to obtain the mean elastic tensor of the bulk extruded composites. Herein, we employ the trapezoidal rule [102] in a similar manner as in previous chapters. Computed results of the mean elastic properties appear in Tables 6-5 and 6-6, where the presented results are evaluated by employing a single value of fiber aspect ratio and a Weibull distribution function, respectively. Note, the "Source" column indicates from which measurements the stiffness tensor (i.e. "Stiffness" as appearing in the second column of the tables) is computed, which is similar to the legends "Pellet results" and "Bead results" appearing in Figures 6-8 to 6-10. Specifically, $\check{C}_{ijkl}(\sim)$ indicates the tensor is evaluated by implementing a single value of fiber aspect ratio (e.g., $\overline{a_r}$ and $\widetilde{a_r}$). Additionally, $\check{C}_{ijkl}^{\overline{a_r}^{N}}$, $\check{C}_{ijkl}^{\overline{a_r}^{W}}$ are computed separately through Equations 6-13 and 6-15 by implementing the fiber aspect ratio Weibull distribution function. Then the elastic constants results are obtained from the computed mean stiffness tensors as in Equation 4-16.

From the given data, it is clearly seen that predicted mean elastic properties exhibit notable variation by applying different approaches in the evaluation, especially in the properties of $\bar{E}_{33}$. Firstly, it can be seen that the fiber length attrition does yield a bias in the predicted $\bar{E}_{33}$, where the results of $\check{C}_{ijkl}^{\overline{a_r}^{W}}$ evaluated using the pellet and bead

measurements separately yields a *PRD* of 6%. Furthermore, the single value fiber aspect ratio approach and the distribution function approach also yields a bias in the computed $\bar{E}_{33}$, such that the values predicted by the bead measurements of $\check{C}_{ijkl}^{\overline{a_r}^N}$, and $\check{C}_{ijkl}(\overline{a_r})$ has a *PRD* of 5%. In combination, if the fiber length attrition between the pellet and bead samples are ignored and the fiber aspect ratio distribution in the deposited bead is also neglected, then the *PRD* between the predicted $\bar{E}_{33}$ can be as high as 12%, i.e., comparing predicted $\bar{E}_{33}$ values by using {pellet measurement: $\check{C}_{ijkl}(\overline{a_r})$} and {bead measurement: $\check{C}_{ijkl}^{\overline{a_r}^N}$} approaches, respectively. Additionally, the $\bar{E}_{33}$ properties computed from $\check{C}_{ijkl}^{\overline{a_r}^N}$ and $\check{C}_{ijkl}^{\overline{a_r}^W}$ using the bead measurements exhibit a *PRD* of 3%, where the weight-averaged property is higher than the number-averaged. It is important to note that the probability density distribution of $\check{C}_{ijkl}^{a_r}$ may not be the Weibull distribution $\mathcal{F}(x)$ for a_r as we assumed since the elastic constants are a nonlinear function of a_r the Tandon-Weng theory (cf. Appendix Part A).

In addition, our numerical estimated equivalent mean property $\bar{E}_{33}$ is approximately 9 to 11 GPa, which generally matches the experimental reported values (e.g., tensile modulus parallel to the printing direction of a printed bead made of 13% CF-ABS [25, 103] (i.e., 7 to 9 GPa). As mentioned, the difference of our prediction and the experimental measurements may be caused by neglecting the voids in the microstructures of a deposited bead (cf. Figure 1-1). We note that a further in-depth study should include experimental validation using tensile test samples of the same material as that used to obtain fiber length data.

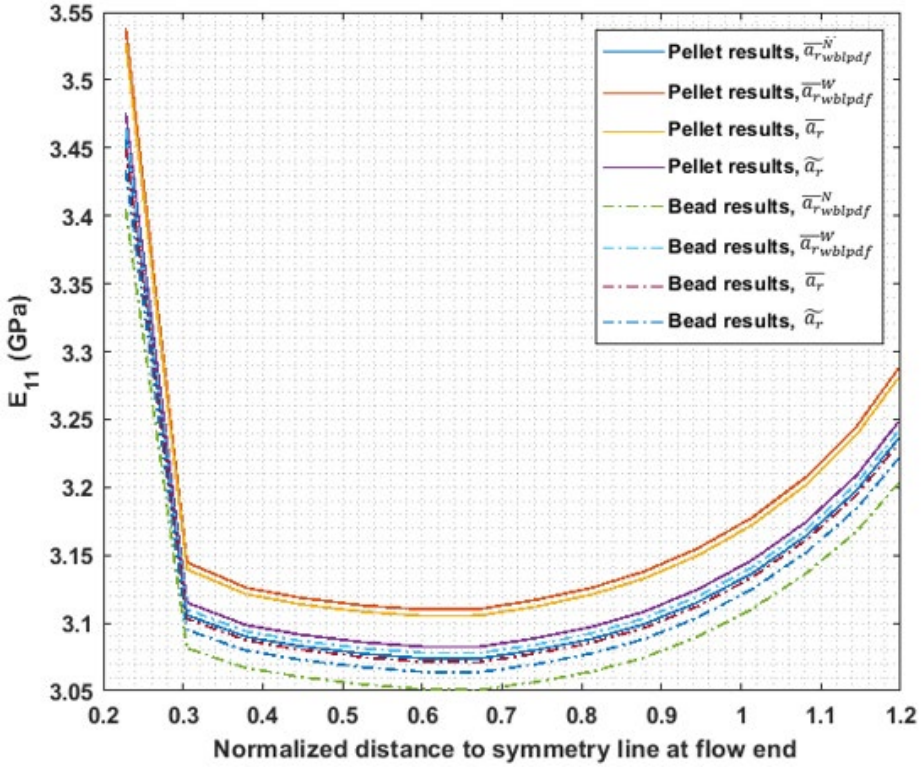

(A)

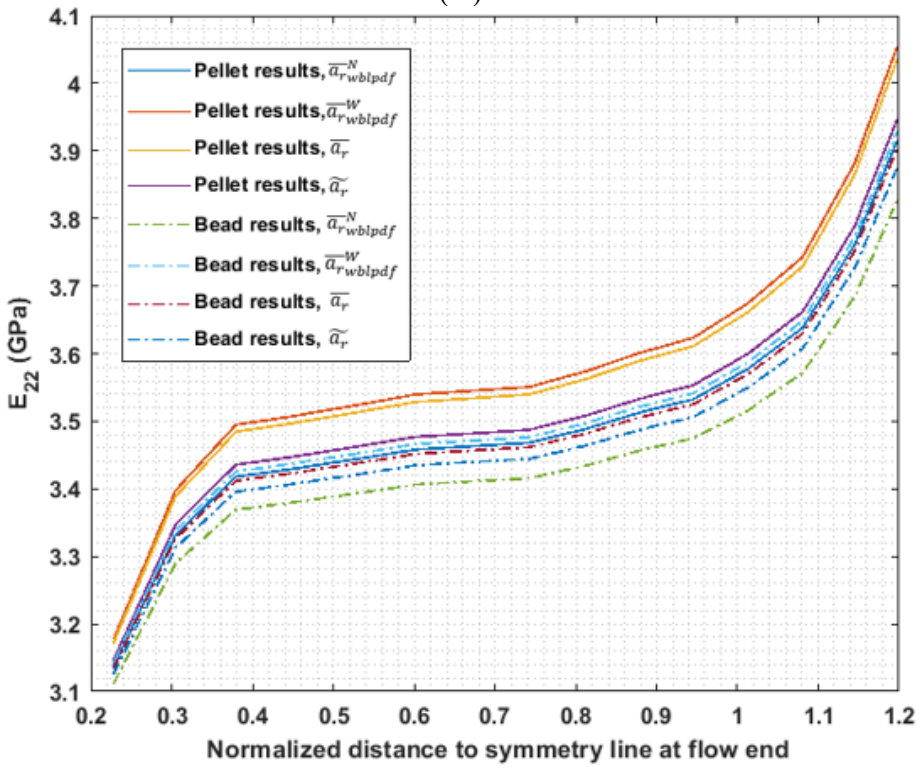

(B)

Figure 6-8. Predicted Properties across the Printed Extrudate: (A) E_{11}; (B) E_{22}.

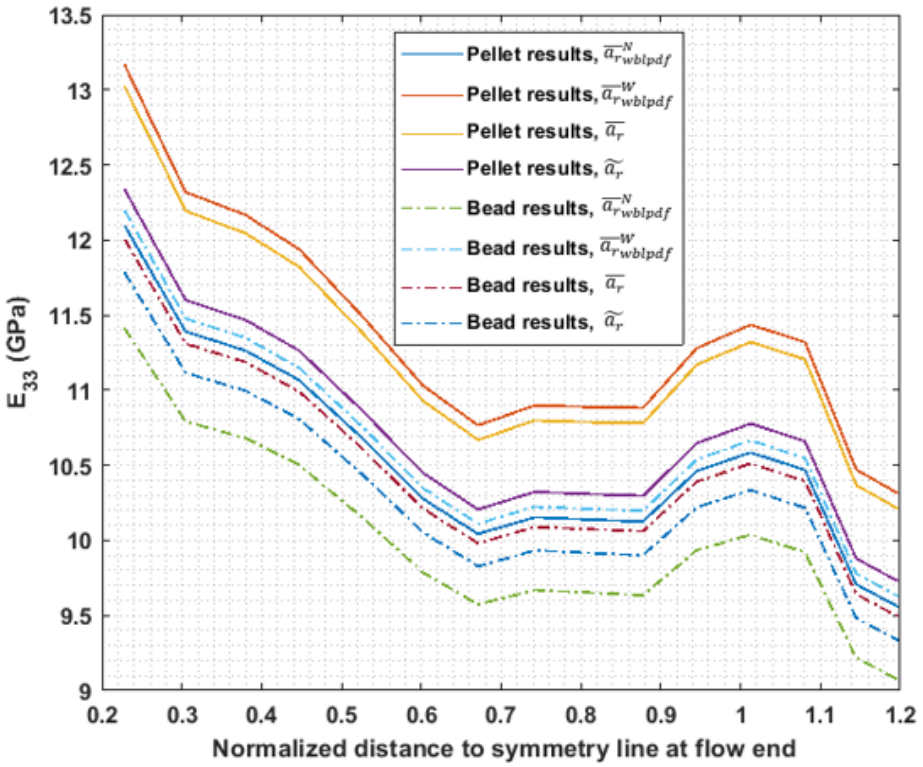

(A)

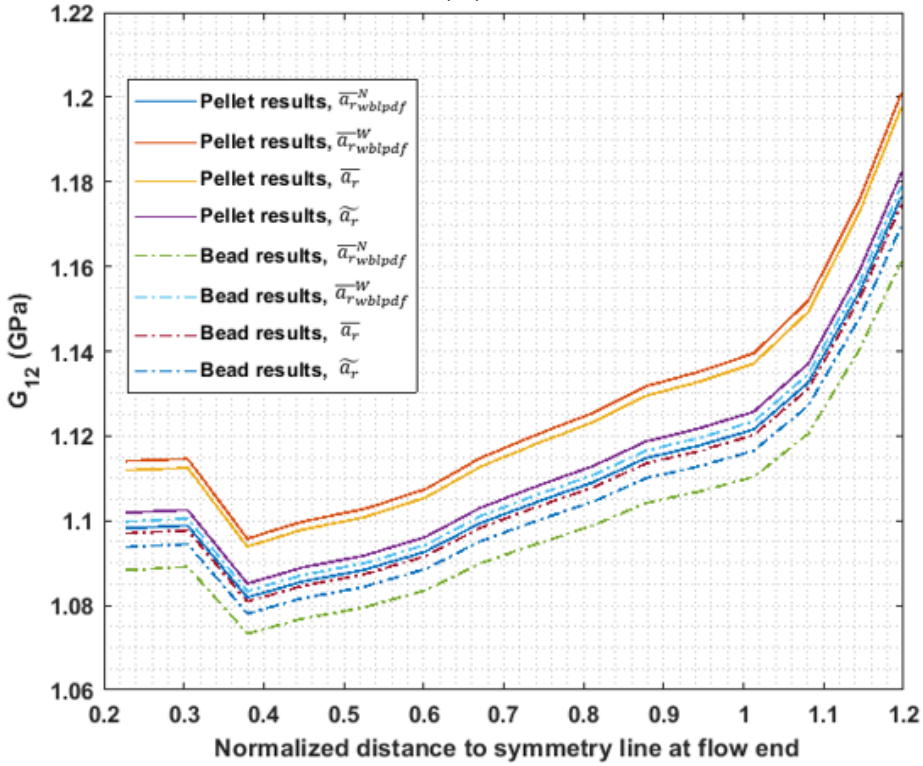

(B)

Figure 6-9. Predicted Elastic Properties across the Printed Extrudate: (A) E_{33}; (B) G_{12}.

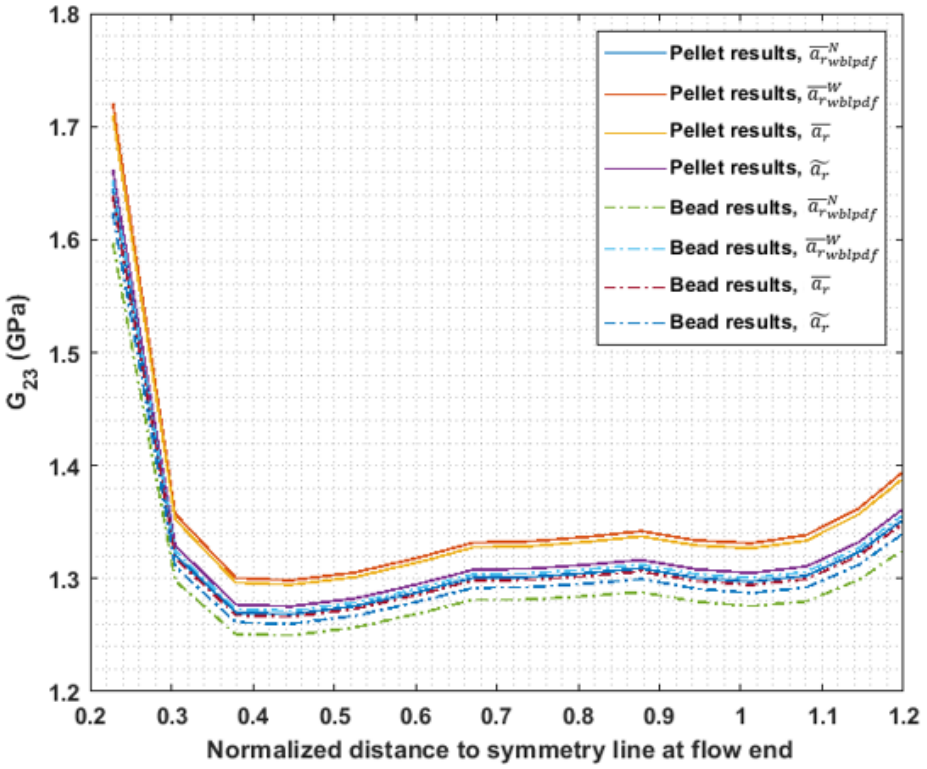

(A)

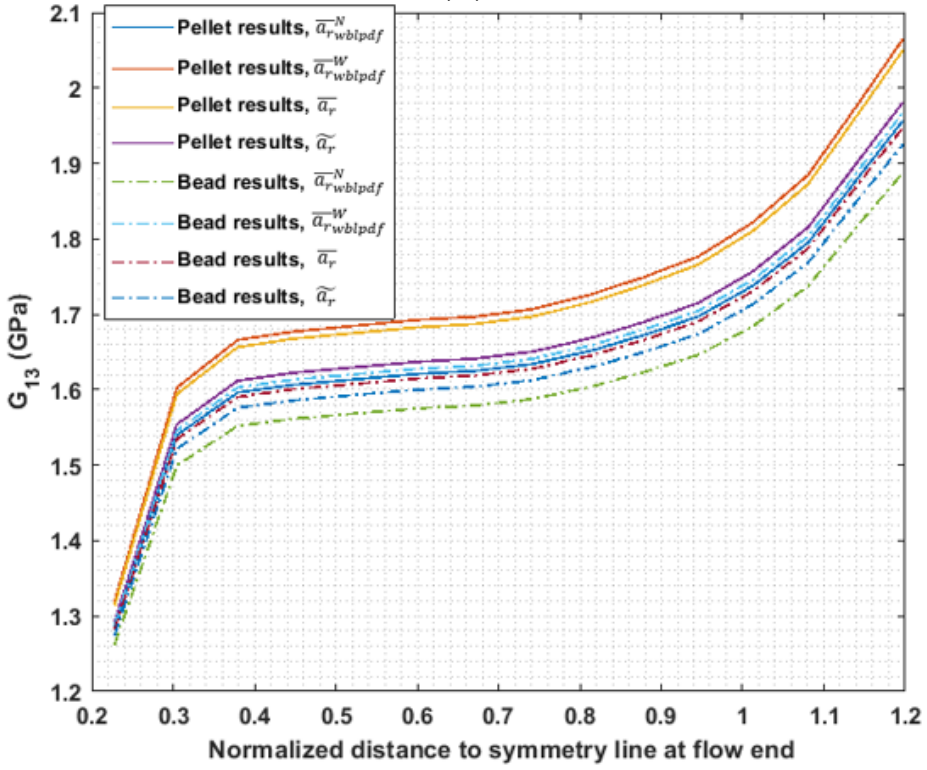

(B)

Figure 6-10. Predicted Elastic Properties across the Printed Extrudate: (A) G_{23}; (B) G_{13}. Note, x_3 direction refers to the direction of extrudate bead (cf. Equation 4-14), and x_1, and x_2 are the transverse directions to the printing direction.

Table 6-5. Mean Elastic Constants of a CF-ABS Extrudate Evaluated with a Constant Fiber Aspect Ratio.

Distribution Source	Stiffness	$\bar{E}_{11}$ (GPa)	$\bar{E}_{22}$ (GPa)	$\bar{E}_{33}$ (GPa)	$\bar{G}_{12}$ (GPa)	$\bar{G}_{23}$ (GPa)	$\bar{G}_{13}$ (GPa)
Pellet	$\check{C}_{ijkl}(\overline{a_r})$	3.16	3.62	11.06	1.13	1.77	1.34
Pellet	$\check{C}_{ijkl}(\widetilde{a_r})$	3.13	3.56	10.55	1.12	1.72	1.31
Bead	$\check{C}_{ijkl}(\overline{a_r})$	3.10	3.53	10.30	1.11	1.69	1.30
Bead	$\check{C}_{ijkl}(\widetilde{a_r})$	3.11	3.51	10.13	1.11	1.67	1.30

Note, x_3 direction refers to the direction of extrudate bead (cf. Equation 3-7), and x_1, and x_2 are the transverse directions to the printing direction. $\bar{C}_{ijkl}(\overline{a_r})$ is the mean stiffness evaluated by implementing the $\overline{a_r}$ resulted from the Weibull distribution function and $\bar{C}_{ijkl}(\widetilde{a_r})$ is the mean stiffness computed by using the $\widetilde{a_r}$ value.

Table 6-6. Mean Elastic Constants of a CF-ABS Extrudate Evaluated through with a Fiber Aspect Ratio Distribution Function.

Distribution Source	Stiffness	$\bar{E}_{11}$ (GPa)	$\bar{E}_{22}$ (GPa)	$\bar{E}_{33}$ (GPa)	$\bar{G}_{12}$ (GPa)	$\bar{G}_{23}$ (GPa)	$\bar{G}_{13}$ (GPa)
Pellet	$\check{C}_{ijkl}^{\overline{a_r}^N}$	3.12	3.54	10.37	1.12	1.70	1.31
Pellet	$\check{C}_{ijkl}^{\overline{a_r}^W}$	3.13	3.56	10.68	1.12	1.72	1.30
Bead	$\check{C}_{ijkl}^{\overline{a_r}^N}$	3.10	3.48	9.84	1.10	1.65	1.28
Bead	$\check{C}_{ijkl}^{\overline{a_r}^W}$	3.10	3.49	10.10	1.11	1.66	1.28

Note, x_3 direction refers to the direction of extrudate bead (cf. Equation 3-7), and x_1, and x_2 are the transverse directions to the printing direction. $\tilde{C}_{ijkl}^{\overline{a_r}^N}$ and $\tilde{C}_{ijkl}^{\overline{a_r}^W}$ are the number average mean stiffness tensor and weight average mean stiffness tensor, respectively, that are evaluated with the Weibull distribution function of fiber aspect ratios through Equations 6-14 and 6-16, respectively.

CHAPTER SEVEN

Mutually Dependent Relations between Melt Flow and Fiber Reinforced

Polymer composite melt flow kinematics evaluated in the prior chapters assumed that the presence of fibers is negligible in the flow computation and the fiber orientation state is solved through the uncoupled flow fields solution. This approach is also referred as the weakly-coupled flow-fiber formulation, which has been proved to be sufficiently accurate and computationally economical in shear dominate narrow gap involved flows applications such as injection molding thin cavity flows [24, 70]. Recently, Brenken, et al. [51] showed that the alignment of fiber reinforcements can significantly alternate the flow behavior of the filled polymer feedstock in FFF-type applications, which indicates the importance of the coupling effects between the polymer melt flow and the reinforced fibers in LAAM polymer deposition applications. Bertevas, et al. [123] simulated the flow behavior of extrusion-based AM deposition process through the mesh-free Smooth Particle Hydrodynamics (SPH) method, where the flow and fiber orientation results were interpolated to five streamlines for further detailed analysis. In contrast, the finite element method places no restrictions on the fiber orientation governing equations (e.g., Equations 3-15) [53] and can be formulated to provide nodal solutions for the flow fields and the second order fiber orientation tensor fields. In addition, nodal values of fiber orientation tensor components offer a convenient form for future design sensitivity analyses, optimization, and inverse analyses of polymer composite melt flow problems. While previous literature (e.g., VerWeyst and Tucker [50] and Dinh and Armstrong [82])

may have addressed the nodal solutions of fiber orientation in polymer processing applications, our investigation herein is more tailored for nozzle-extrudate scenarios occurring in LAAM applications, which can be further implemented into inverse analysis on mechanical properties of extruded materials, inverse die design in terms of the nozzle geometries.

Hereinafter, we present a finite-element-based algorithm to quantify the mutually dependent relationship between the polymer melt flow and the reinforced fiber orientation in a melt extrusion nozzle flow with a short section of post-nozzle extrudate, where the simulation of die swell phenomena is included. There are advantages for solving the coupled flow-fiber problem through a commercial code, like ANSYS-Polyflow used in previous chapters, by which we would be able to take advantages of its built-in computational functions to explain in-depth sciences for polymer composite flow. Unfortunately, the user-defined functions provided by ANSYS-Polyflow does not enable us to incorporate the effects of fiber orientation into the flow computation using anisotropic viscosity constitutive laws (cf. Section 3.3). Alternatively, we employ the Galerkin Finite Element Method (GFEM) to recast the governing equations of the flow fields and the fiber orientation tensor due in part to its concise form and since there are no additional restrictions on the parameters of the fiber orientation equation (e.g., see Equation 3-15) [53]. To reduce the difficulty of convergence of the coupled algorithm, the system is decomposed into separate parts where the flow and fiber orientation are computed individually in an iterative manner. The coupling scheme is introduced in a separately section after the formulation of the flow and fiber orientation solutions.

7.1 Computation of Flow Fields

The general 2-D domain in Figure 7-1 is considered to facilitate the derivation of the finite element formulation for the melt flow and fiber orientation where Ω is an integrable continuum, and Γ_v and Γ_σ are mutually exclusive boundaries subjected to imposed velocity (i.e., $\boldsymbol{v}$) and stress (i.e., $\boldsymbol{\sigma}$), respectively.

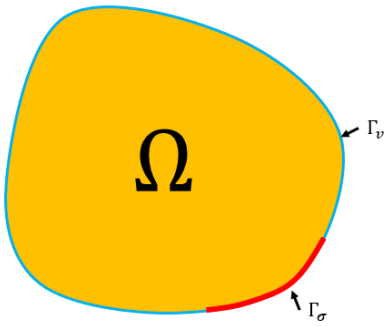

Figure 7-1. Finite Element Domain and Associated Boundaries for Flow Problems.

Following a standard GFEM approach (e.g., see [124]), the weak forms of the mass the momentum conservation equations (cf. Equations 3-1 and 3-2) can be written as

$$\int_\Omega \boldsymbol{w}^T(\nabla \cdot \boldsymbol{v})\, d\Omega = 0, \tag{7-1}$$

and,

$$\int_\Omega \boldsymbol{w}^T(\nabla \cdot \boldsymbol{\sigma} + \rho \boldsymbol{f})\, d\Omega = 0, \tag{7-2}$$

where $\boldsymbol{w}$ is an arbitrary weight function and other terms are as defined in Section 3.1 above. Following the GFEM theory, the arbitrary weight function is set to be the same as the interpolation function, such that $\boldsymbol{w} = \boldsymbol{N^e}$. Expanding the term of $\boldsymbol{\sigma}$ as in Equation 3-3, and then applying integration by parts, we obtain

$$\int_\Omega [(\boldsymbol{\nabla_s w})^T \boldsymbol{V}\, \boldsymbol{\nabla_s v}] d\Omega - \int_\Omega P(\boldsymbol{\nabla_s^T w})^T\, d\Omega = \int_\Omega \boldsymbol{w}^T \rho \boldsymbol{f}\, d\Omega + \int_{\Gamma_\sigma} \boldsymbol{w}^T \vec{\boldsymbol{t}} d\Gamma, \tag{7-3}$$

where $\vec{\boldsymbol{t}}$ is the stress trajectory applied to Γ_σ boundary (cf. Figure 7-1). In the above, $\boldsymbol{\nabla_s}$ is symmetric gradient operator for a 2-dimensional axisymmetric coordinate system [124] which is written as

$$\boldsymbol{\nabla_s} = \begin{bmatrix} \frac{\partial}{\partial r} & 0 & \frac{\partial}{\partial z} & \frac{1}{r} \\ 0 & \frac{\partial}{\partial z} & \frac{\partial}{\partial r} & 0 \end{bmatrix}^T, \tag{7-4}$$

and $\boldsymbol{V}$ appearing in Equation 7-3 is an integrated form of viscosity matrix for axisymmetric flow written as

$$\boldsymbol{V} = \eta \begin{bmatrix} 2 & 0 & 0 & 0 \\ 0 & 2 & 0 & 0 \\ 0 & 0 & 1 & 0 \\ 0 & 0 & 0 & 2 \end{bmatrix}, \tag{7-5}$$

The implementation of $\boldsymbol{\nabla_s}$ and $\boldsymbol{V}$ simplifies the expression appearing Equation 7-2 to the more concise format appearing in Equation 7-3, which better facilitates the FEM matrix calculations below. Additionally, the fiber orientation is incorporated into the viscosity matrix based on Equation 3-27, such that [125]

$$\widetilde{\boldsymbol{V}} = \eta \begin{bmatrix} 2 & 0 & 0 & 0 \\ 0 & 2 & 0 & 0 \\ 0 & 0 & 1 & 0 \\ 0 & 0 & 0 & 2 \end{bmatrix} + 2\eta N_p \begin{bmatrix} \mathcal{A}_{1111} & \mathcal{A}_{1133} & \mathcal{A}_{1113} & \mathcal{A}_{1122} \\ \mathcal{A}_{3311} & \mathcal{A}_{3333} & \mathcal{A}_{3313} & \mathcal{A}_{3322} \\ \mathcal{A}_{1311} & \mathcal{A}_{1333} & \mathcal{A}_{1313} & \mathcal{A}_{1322} \\ \mathcal{A}_{2211} & \mathcal{A}_{2233} & \mathcal{A}_{2213} & \mathcal{A}_{2222} \end{bmatrix}, \tag{7-6}$$

where the $\mathcal{A}_{ijkl}$ refer to the components of the fourth order orientation tensor $\mathbb{A}$. Hereinafter, the viscosity matrix $\boldsymbol{V}$ appearing in Equation 7-3 is replaced by $\widetilde{\boldsymbol{V}}$, which is an anisotropic viscosity tensor that is a function of the fourth order orientation tensor (cf. Equation 3-27). Note, derivations shown above are designated particularly for an axisymmetric flow model such as the melt extrusion nozzle flow interested in this study.

The discretization of the unknown velocity and orientation tensor components may be written in terms of nodal values, such that the velocity vector $\boldsymbol{v}$ can be written as

$$\boldsymbol{v} = \boldsymbol{N^e d^e}, \tag{7-7}$$

where $\boldsymbol{d^e}$ is the nodal velocity vector and $\boldsymbol{N^e}$ is the 2-dimensional Lagrangian bi-linear interpolation function [124]. The superscript e shown in here and after refers to the elemental terms for a single finite element.

In this study, the flow domain will be meshed with 2-dimensional quadrilateral elements where $\boldsymbol{d^e}$ and $\boldsymbol{N^e}$ are given, respectively, for 4-node quadrilateral element as

$$\boldsymbol{d^e} = [v_r^1 \quad v_z^1 \quad v_r^2 \quad v_z^2 \quad v_r^3 \quad v_z^3 \quad v_r^4 \quad v_z^4], \tag{7-8}$$

and

$$\boldsymbol{N^e} = \begin{bmatrix} N_1 & 0 & N_2 & 0 & N_3 & 0 & N_4 & 0 \\ 0 & N_1 & 0 & N_2 & 0 & N_3 & 0 & N_4 \end{bmatrix}, \tag{7-9}$$

Here, v_i^j indicate the nodal velocity component, where j refers to the node number (i.e., $j = \{1,2,3,4\}$ for 4-node quadrilateral elements), and i refers to the degree of freedom (i.e., $i = \{r, z\}$ for 2D flow models in cylindrical coordinates). In addition, N_j is the component of a linear Lagrangian interpolation functions [124]. Other forms of Equations 7-8 and 7-9 may be employed for higher order interpolations and also for higher spatial dimension as is common in the Finite Element Method (see e.g., [124]).

Finite-element-formulated fluid flow problems are often solved by the mixed method, where the velocity and pressure are the primary unknowns; or, the penalty method, where velocity field of the flow is the primary nodal unknown and the pressure field is post-computed based on the achieved flow fields [124]. Herein, the penalty method is adopted for simplicity, as implementing the mixed method requires additional degrees of freedom for interpolating the pressure field. In the formulation of the penalty method, the pressure is written in terms of the primary variable (i.e. velocity) through the

incompressibility assumption made in the continuity equation (cf. Equation 3-1). The resulting expression of pressure is [124]

$$P = -\gamma_e \vec{\mathbf{1}}^{\,T} \boldsymbol{B}_s^e \boldsymbol{d}^e, \tag{7-10}$$

where γ_e is the penalty constant related to the degree of incompressibility of the flow, which is often select between 10^4 to 10^{12} of the kinematic viscosity of the fluid flow (i.e., $\nu_k = \eta/\rho$ [124]). In the above, $\vec{\mathbf{1}}$ is a dimension transformation vector, such that $\vec{\mathbf{1}} = [1 \quad 1 \quad 0 \quad 1]^T$ for two-dimensional axisymmetric models. Additionally, $\boldsymbol{B}_s^e$ is the strain displacement matrix, which is defined as [124]

$$\boldsymbol{B}_s^e = \boldsymbol{\nabla}_s \boldsymbol{N}^e, \tag{7-11}$$

Ultimately, the finite element form of the momentum equation (cf. Equation 3-2) can be expressed as

$$\boldsymbol{K}^e \boldsymbol{d}^e = \boldsymbol{F}^e \tag{7-12}$$

where the stiffness matrix $\boldsymbol{K}^e$ is written as

$$\boldsymbol{K}^e = \int_\Omega [(\boldsymbol{B}_s^e)^T \, \boldsymbol{C} \, \boldsymbol{B}_s^e] \, d\Omega + \gamma_e \int_\Omega [(\boldsymbol{B}_s^e)^T \, \mathbf{1} \, \mathbf{1}^T \, \boldsymbol{B}_s^e] \, d\Omega, \tag{7-13}$$

and the nodal force vector $\boldsymbol{F}^e$ is written as

$$\boldsymbol{F}^e = \int_\Omega [\, \rho \, (\boldsymbol{N}^e)^T \boldsymbol{f}] \, d\Omega + \int_{\Gamma_\sigma} [\, (\boldsymbol{N}^e)^T \, \vec{\boldsymbol{t}} \,] \, d\Gamma, \tag{7-14}$$

The elemental matrices in Equations 7-12 through 7-14 are assembled into the global finite element matrix equation in the usual manner, such that

$$\boldsymbol{K}\boldsymbol{d} = \boldsymbol{F}, \tag{7-15}$$

The above concludes the finite element formulation of an incompressible and isothermal creeping flow governing equations in 2D cylindrical coordinates (e.g., flow model appears in Chapter Four).

7.1.1 Newton-Raphson Iteration Method

When shearing thinning fluid flow models are employed, Equation 7-12 becomes nonlinear since the viscosity is a function of shear rate which makes the stiffness matrix $\boldsymbol{K^e}$ a function of nodal velocity $\boldsymbol{d^e}$. Recall that shear rate also refers to the scalar magnitude of the rate-of-deformation tensor $\boldsymbol{D}$, which is the symmetric part of the velocity gradient. Herein, the nonlinear solution Newton-Raphson (N-R) iterative method is applied to solve the nonlinear system in Equation 7-15. The basic procedure of the N-R iteration is abbreviated here for conciseness and readers of interest can find a detailed instruction in multiple literatures such as [126, 127]. Implementing the N-R method requires the information of the gradient of the system with respective to the primary unknown. Herein, we first recast our GFEM-formulated system (i.e., Equation 7-15) in the form of residual ($\boldsymbol{H}$) as

$$\boldsymbol{H} = \boldsymbol{K}(\boldsymbol{d})\boldsymbol{d} - \boldsymbol{F}, \tag{7-16}$$

Note, our goal is to zero the $\boldsymbol{H}$ matrix which is performed in the Newton-Raphson method with the tangent stiffness matrix (designated as $\boldsymbol{U}$) of the system which is written as

$$\boldsymbol{U} = \frac{d[\boldsymbol{H}(\boldsymbol{d})]}{d(\boldsymbol{d})} = \frac{d[\boldsymbol{K}(\boldsymbol{d})\boldsymbol{d}-\boldsymbol{F}]}{d(\boldsymbol{d})} = \frac{d(\boldsymbol{K}(\boldsymbol{d}))}{d(\boldsymbol{d})}\boldsymbol{d} + \boldsymbol{K}\frac{d(\boldsymbol{d})}{d(\boldsymbol{d})} - \frac{d(\boldsymbol{F})}{d(\boldsymbol{d})}, \tag{7-17}$$

For consistency, the further extension of Equation 7-17 is given in Appendix Part B. Following the N-R method procedure (e.g., see [126]), the nodal solution of the system can be update by

$$_{p+1}\boldsymbol{d} = {}_{p}\boldsymbol{d} - inv\left[\boldsymbol{U}\left({}_{p}\boldsymbol{d}\right)\right]\boldsymbol{H}\left({}_{p}\boldsymbol{d}\right), \tag{7-18}$$

In the above, "*inv*" refers to the inverse of a matrix. The left subscript (i.e., $p+1$) of $\boldsymbol{d}$ counts the iterative steps of the N-R iteration. Prior literature (e.g., [74]) suggests that

convergence of the N-R method using Equations 7-17 and 7-18 when solving the shear thinning fluid flows is often difficult. We, therefore, use the relaxed form of the N-R iteration

$$ {}_{p+1}\boldsymbol{d} = {}_{p}\boldsymbol{d} - s_{nr}\{inv[\boldsymbol{U}({}_{p}\boldsymbol{d})]\,\boldsymbol{H}({}_{p}\boldsymbol{d})\}, \tag{7-19} $$

where s_{nr} a relaxation coefficient that is in the interval between 0 to 1. The implementation of the scalar factor reduces the convergence speed but the radius of convergence of the N-R iteration is enhanced which increases the probability of convergence [74]. In the simulations given below, it is found that s_{nr} = 0.2 works well for solving the coupled flow fields using a power law fluid. Note that the Polyflow user-guide [74] identifies that the Picard scheme for solving nonlinear equations (e.g., fix-point iteration method [102]) may be a more effective alternative to the N-R method for solving the non-Newtonian shear thinning flow fields. While implementing additional numerical methods for faster convergence is beyond our main scope of characterizing the coupling effects of flow-fiber in an open flow of polymer composite extrusion.

7.1.2 Mesh Relocation for Free Extrudate

Identifying the location of the free surface boundary location for an external flow application requires remeshing the flow domain of the free extrudate. The finite element suite ANSYS Polyflow [74] provides powerful remeshing techniques to simulate the polymer processing applications involving with free surface boundaries. A few publications related to the polymer deposition process modelled the melt extrusion and/or material deposition process through the advanced functions provided by Polyflow (e.g., see [47, 67, 68, 99]). In other work, Heller, et al. [19, 30] developed a customized MATLAB (Natick, MA, USA) code to compute the optimum free surface location by

minimizing the integrated normal stress over the free boundary nodes. The code is used as a subroutine in conjunction with the commercial finite element suite COMSOL (Burlington, MA, USA) to simulate extrudate swell in melt extrusion [19] and material deposition [30] for the LAAM technology.

The ANSYS-Polyflow code is currently not suitable for the flow-fiber coupled analysis described above, to the best of our knowledge. Also, the optimization methodology proposed by Heller, et al. [19, 30] requires additional iterations to solve for the free surface. Alternatively, Tanner, et al. [128] computed the location of the free surface boundary for an axisymmetric flow by considering the free surface as a streamline such that the position of successive points that define the flow boundary may be computed from

$$r_{i+1}^{(j)} = r_i^{(j)} + \int_{z_i}^{z_{i+1}} \frac{v_r}{v_z} dz, \tag{7-20}$$

where r_i is the radial coordinates of nodes on the free surface, and z_i are coordinates of nodes parallel to the flow. This approach is a computationally economic approach for flow domain of the interest. Herein, we compute the radii of surface nodes through Equation 7-20 as shown in Figure 7-2, where the subscript i indicates successive node numbers starting at 0 with a known r_0 referring to the fixed intersecting node of the no-slip wall and free extrudate surface. The integration of Equation 7-20 is evaluated through the 1/3 Simpson's rule as in [58, 129]. In this implementation, nodal coordinates along z axis are fixed. Once the locations of surface nodes are identified, the internal nodes of the free extrudate can be achieved through a linear 1-D interpolation in the r-direction.

It is important to note that the location of the free surface boundary cannot be obtained in a single step but instead requires an iterative scheme. We found that four to eight iterations are typically sufficient in the problems considered here to yield a converged free surface boundary location depending on the quality of the mesh-size of the domain. Convergence of free surface iterations is assumed based on the relative steady state die swell ratio of the extrudate (e.g., $B^{(j)}$, where j refers to the j-th iteration of the flow computation, and B is defined through Equation 4-13). Additionally, it should also be noted that this methodology ignores the effect of the surface tension. The extrusion distance between the nozzle tip and the print-substrate in the polymer deposition manufacturing process is typically small, within a few millimeters, thus supporting the assumption that surface tension factor is negligible.

One computational issue that must be addressed relates to the singularity occurring in the identification of the free surface location. The GFEM formulation requires stress continuity along the flow boundary while the stress field at the nozzle exit corner of an extrusion flow between the no-slip wall boundary and no-limit free surface boundary is disconnected [58, 129]. As a result, a too-fine mesh enhances the singularity issue and the resulting free surface oscillates significantly while a too-coarse mesh yields less reliable prediction. Consequently, a compromise is needed for the mesh quality near the extrusion lip such that an ideal moderate size elements reduce the peak values and smooth the solution [58, 129] (cf. Section 7.5 for the detail of the finite element mesh for the flow domain of interest).

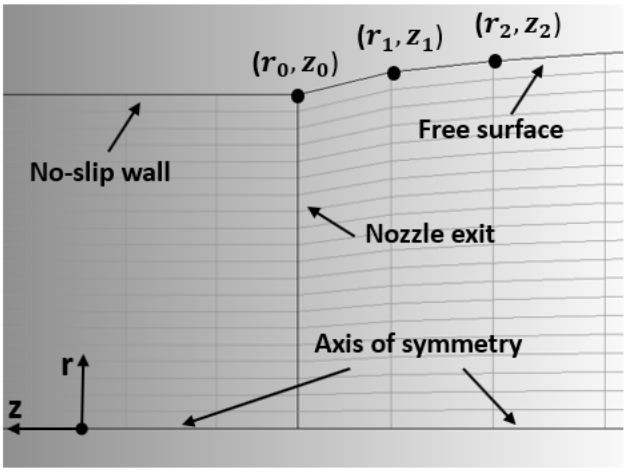

Figure 7-2. Schematic Diagram of the Streamline-Wise Remeshing Approach.

7.2 Computation of Fiber Orientation States

In this chapter, the fiber orientation state is represented by the second order orientation tensor solved through the Advani-Tucker tensor approach Folgar-Tucker IRD model [22] rather than the RSC model (cf. Equation 3-17) as applied in Chapters Four and Five to reduce the computational complexity. The advanced RSC model may yield more accuracy to the predicted orientation results but is beyond our main scope in this chapter.

To simulate fiber orientation, we first consider a simplification made in VerWeyst and Tucker [53], where the right-hand side of Advani-Tucker equation (cf. Equation 3-15) is defined as the vector $\boldsymbol{m}$ where m_k, and k refers to the k-th component of vector $\boldsymbol{m}$ [53]. It follows that the weak form of Equation 3-15 can be written as

$$\int_{\Omega} \boldsymbol{w}^T \left[\frac{\partial \boldsymbol{a}}{\partial t} + \boldsymbol{v} \cdot \nabla \boldsymbol{a} - \boldsymbol{m}\right] d\Omega = 0, \tag{7-21}$$

In the above, $\boldsymbol{a}$ is the primary unknown in the fiber orientation problem, which is a vector of the five independent components of the $\boldsymbol{A}$ tensor written as

$$\boldsymbol{a} = a_k = [a_1 \quad a_2 \quad a_3 \quad a_4 \quad a_5] = [A_{11} \quad A_{12} \quad A_{13} \quad A_{22} \quad A_{23}]. \tag{7-22}$$

Similarly, $\boldsymbol{m}$ contains of five components $\frac{DA_{ij}}{Dt}$ corresponding to the A_{ij} in Equation 7-22.

We employ a 4-node quadrilateral element to discretize $\boldsymbol{a}$, in a manner similar to that in flow problem shown above to obtain

$$\boldsymbol{a} = \boldsymbol{N_a^e d_a^e}, \tag{7-23}$$

Herein and after, the subscript "*a*" is applied on related variables (e.g., $\boldsymbol{d_a^e}$, $\boldsymbol{N_a^e}$) to identify their association with the orientation tensor **A** in a manner similar to that used in the flow problem.

The nodal orientation tensor variable vector and its associated shape function matrix can be expressed as

$$\boldsymbol{d_a^e} = [a_1^1 \quad a_2^1 \quad a_3^1 \quad a_4^1 \quad a_5^1 \quad \ldots \quad a_1^4 \quad a_2^4 \quad a_3^4 \quad a_4^4 \quad a_5^4], \tag{7-24}$$

and

$$\boldsymbol{N_a^e} = \begin{bmatrix} N_1 & 0 & 0 & 0 & 0 & & N_4 & 0 & 0 & 0 & 0 \\ 0 & N_1 & 0 & 0 & 0 & & 0 & N_4 & 0 & 0 & 0 \\ 0 & 0 & N_1 & 0 & 0 & \ldots & 0 & 0 & N_4 & 0 & 0 \\ 0 & 0 & 0 & N_1 & 0 & & 0 & 0 & 0 & N_4 & 0 \\ 0 & 0 & 0 & 0 & N_1 & & 0 & 0 & 0 & 0 & N_4 \end{bmatrix}, \tag{7-25}$$

The notation "..." refers to an abbreviation of expressions associated with two intermediate nodes of a 4-node quadrilateral element. Note, the dimensions of $\boldsymbol{d_a^e}$ and $\boldsymbol{N_a^e}$ are 20-by-1 and 5-by-20, respectively. Upon substitution of Equations 7-24 and 7-25 into Equation 7-21 and also enforcing $\boldsymbol{w} = \boldsymbol{N_a^e}$ (i.e., based on GFEM theory), we obtain

$$\int_\Omega (\boldsymbol{N_a^e})^T \left[\frac{d(\boldsymbol{N_a^e d_a^e})}{dt} + \boldsymbol{v} \cdot \nabla(\boldsymbol{N_a^e d_a^e}) - \boldsymbol{m}\right] d\Omega = 0, \tag{7-26}$$

Herein, we assume that the nodal variable $\boldsymbol{d_a^e}$ is exclusively a spatial-based function and thus the partial derivative of the primary variable with respect to time is zero. However, VerWeyst and Tucker [53] found that a steady state fiber orientation state for flows in

relatively complex geometries can seldom be achieved in one step (i.e., ignoring the time derivative term appearing in Equation 7-26). Hence, a time-marching frame has to be applied to Equation 7-26, where the flow fields is fixed during the fibers orientation evaluation and a forward Euler approach [102] is applied in a transient simulation that is used to reach the steady state solution. Therefore, the steady state solution is evolved from an initial approximation of the isotropic fiber alignment among the entire flow domain through delicately managed small perturbations of time steps. Consequently, Equation 7-26 can be rewritten as

$$\int_{\Omega} (\boldsymbol{N_a^e})^T \left[\frac{\boldsymbol{N_a^e}(\boldsymbol{d_a^e}|^q - \boldsymbol{d_a^e}|^{q-1})}{\Delta t} + \boldsymbol{v} \cdot \nabla(\boldsymbol{N_a^e}(\boldsymbol{d_a^e}|^q) - \boldsymbol{m}^{q-1}\right] d\Omega = 0, \tag{7-27}$$

or

$$\boldsymbol{K_a^e d_a^e} = \boldsymbol{F_a^e}, \tag{7-28}$$

where the stiffness matrix $\boldsymbol{K_a^e}$ is

$$\boldsymbol{K_a^e} = \int_{\Omega} \left[\frac{(\boldsymbol{N_a^e})^T \boldsymbol{N_a^e}}{\Delta t} + \boldsymbol{v} \cdot \nabla(\boldsymbol{N_a^e})\right] d\Omega, \tag{7-29}$$

and the nodal force vector $\boldsymbol{F_a^e}$ is

$$\boldsymbol{F_a^e} = \int_{\Omega} \left[\frac{(\boldsymbol{N_a^e})^T \boldsymbol{N_a^e}}{\Delta t} \boldsymbol{d_a^e}|^{q-1} + \boldsymbol{m}^{q-1}\right] d\Omega, \tag{7-30}$$

Ultimately, the elemental equations shown above are assembled in the global format as appearing in Equation 7-15. Note, $\boldsymbol{d_a^e}|^q$ and $\boldsymbol{d_a^e}|^{q-1}$ appearing in Equation 7-30 indicate the fiber orientation solution at $t = t_q$ and $t = t_{q-1}$, where $\Delta t = t_q - t_{q-1}$. In addition, $\boldsymbol{m}^{q-1}$ is computed from the right-hand side of Equation 3-15 (i.e., Advani-Tucker orientation tensor evaluation equation) using the second order orientation tensor solution obtained at $t = t_{q-1}$. In addition, the step size of time-marching scheme (i.e., Δt) in solving the fiber orientation tensor field is fixed as a constant and the value of the step

size is dependent on the dimensions of flow fields. Herein, the time-marching scheme utilizes a step size of 0.01, and a steady-state within each fiber orientation computation can be achieved within 30 time-steps.

It should be noted that the GFEM formulated form of the fiber orientation governing equation is a nonlinear problem as well and thus the implementation of the N-R method is required again for solving the nonlinear system. The derivation of the tangent stiffness matrix is included in Appendix Part B. Nevertheless, we found that $s_{nr} = 1$ (cf. Equation 7-19) worked well when iteratively solving the fiber orientation problem.

The GFEM solution was found to yield non-physical results of fiber orientation tensors in some simulations such that the diagonal terms of a solved second order orientation tensor would exceed unity. Herein, we adopt the strategy proposed by VerWeyst and Tucker [53] (e.g., see [53] for more detail).

7.2.1 Streamline Upwind Petrov Galerkin Method for Spatial Instability of the Solution

Fiber orientation solutions obtained through the GFEM formulation described above may yield spatially instability (e.g., wiggles appearing in the resulting contours over neighbouring nodes) due to the lack of a diffusion term in the Advani-Tucker fiber orientation tensor equation (cf. Equation 3-15) [53]. The Streamline Upwind Petrov Galerkin (SUPG) method proposed by Brooks and Hughes [130] provided a spatially stable yet physically realistic solution alternative to the standard GFEM's. The SUPG method has been implemented to multiple fluid flow studies (e.g., see [131-133]), and here we only introduce the explicit form proposed by Smith, et al. [132]. In our SUPG

implementation, the arbitrary weight function $\boldsymbol{w}$ is replaced with an augmented weight function $\widetilde{\boldsymbol{w}}$ as

$$\widetilde{\boldsymbol{w}}(\boldsymbol{d}_{\boldsymbol{a}}^{\boldsymbol{e}}, \boldsymbol{w}) = \boldsymbol{w} + \frac{\alpha h_e(v)}{2||\boldsymbol{v}||} \nabla \cdot (\boldsymbol{w}\, \boldsymbol{v}), \tag{7-31}$$

where h_e is the characteristic element length in the direction of flow velocity in an element. An expression for h_e for isoparametric elements can be found in [132]. Since flow incompressibility is assumed, $\nabla \cdot \boldsymbol{v} = 0$ as appearing in Equation 3-1, and thus Equation 7-31 can be written as

$$\widetilde{\boldsymbol{w}}(\boldsymbol{d}_{\boldsymbol{a}}^{\boldsymbol{e}}, \boldsymbol{w}) = \boldsymbol{N}_{\boldsymbol{a}}^{\boldsymbol{e}} + \frac{\alpha h_e(v)}{2||\boldsymbol{v}||} \nabla \boldsymbol{N}_{\boldsymbol{a}}^{\boldsymbol{e}} \cdot \boldsymbol{v}, \tag{7-32}$$

Here, $\boldsymbol{w}$ is the standard arbitrary weight function in GFEM such that $\boldsymbol{w} = \boldsymbol{N}_{\boldsymbol{a}}^{\boldsymbol{e}}$, and$\alpha$ is a scale factor controlling the intensity of the streamline upwinding [132].

When solving the fiber orientation problem, the standard arbitrary weight function is replaced by the form of Equation 7-32. Particularly, Smith, et al. [132] suggested that the value of α be determined by several trials to make sure that just enough numerical diffusion is added through streamline upwinding to smooth the numerical instability without yielding unrealistic computed results. Herein, we adopt a similar method as in Smith, et al. [132], where gradually increasing values of α (cf. Equation 7-32) are attempted. Among these, the ideal value of α is settle down as spatial instabilities in the computed contours of fiber orientation tensor fields are minimally seen with additional increments. For the flow domain of interest (cf. Figure 7-3C appearing in next section), the scale of SUPG is chosen as α = 0.5. For consistency, further detail appears in Appendix Part C.

7.3 Flow Domain and Material Model

This study focuses on the melt extrusion process in LAAM applications, where the flow-fiber coupling effects are of significant importance. Herein, the flow model is created based on the geometrical design of a Strangpresse large-scale additive manufacturing Model 19 single screw extruder nozzle (cf. Figure 7-3A). As the main scope of this work is to propose an effective numerical scheme for solving the fully coupled flow-fiber suspension problem, the domain of flow model is simplified as compared to that presented in previous chapters (e.g., see Figure 7-3B), such that only the exit tubular region of the nozzle is considered as shown in Figure 7-3C. This geometrical simplification saves the computational cost and reduces the difficulty of convergence of the proposed algorithm. The diameter of the straight tube that defines our flow domain is 0.003175m (i.e., 1/8 inch). Due to the symmetry of the nozzle geometry, a 2D axisymmetric flow domain is employed (i.e., we assume no flow swirling effect). Specifically, the ratio of the internal-nozzle length of to the radius of the nozzle is set to 5:1. In addition, the length of the free extrudate is set to be equal to the internal-nozzle length. The chosen lengths of the internal tube and free extrudate allow a significantly adequate distance for the flow-fiber interactions to develop to a steady-state.

The boundary conditions of the flow domain appearing in Figure 7-3C share the same definitions as defined in Chapter Four. Specifically, the fully developed velocity profile imposed in the flow inlet is computed based on a volume flow rate $Q = 8 \times 10^{-7}\mathrm{m}^3/\mathrm{s}$ (i.e., similar to the input given in Chapter Five to simulate large volume polymer deposition). And the velocity profile is computed in advance through the commercial code Polyflow [74], in a traditional uncoupled formulation (i.e., effects of

fiber presence are not counted). Note, the inlet condition is fixed as imposed apart from the flow iterative computation.

In addition, the fiber orientation equation is a hyperbolic equation and thus only an initial condition at the flow inlet is required. Herein, a fully developed fiber orientation state from previous related literature (cf. Heller [19, 93]) is imposed as the fiber orientation state at the flow inlet, assuming that the orientation state reaches somewhat a steady state at the inlet of the flow. Specifically, the fiber alignment along the no-slip wall is assumed to be aligned along the flow direction instantaneously and the fiber-wall interaction is then neglected [94]. In our experience, such assumption enhances convergence of the overall code while the accuracy of most area of the flow domain retains. Notice, the initial and boundary conditions specified for the fiber orientation calculation are fixed throughout the iterative process.

Unlike previous chapters that simulate ABS or 13% CF-ABS, the rheological shear viscosity properties of virgin Polyethylenimine (PEI) polymer at 400 °C is adopted in this chapter to model the fluid flow of interest since the non-linearity of the power law of the PEI polymer is reduced as compared to ABS polymer's (cf. Table 4-1). The shear viscosity data is obtained by curve-fitting data from Ajinjeru, et al. [134], where the applicability of the Cox-Merz rule [100] for transferring the experimental data and numerical fitting is assumed. The power-law region of the shear rate is assumed to be between 10^1 s^{-1} and 10^3 s^{-1}, which is a typical region for LAAM applications (e.g., see [92]). Ultimately, the fitted results of K and n (cf. Equation 3-8) are 950 and 0.86, respectively. And λ_c is set as unity. For the purpose of quantifying the coupling effects, we assume 20% weight percentage carbon fiber reinforcements in the PEI polymers (i.e.,

the polymer composite used in [134]), and by using Equation 4-17 and data from Ajinjeru, et al. [134], we define the volume fraction short carbon fibers as v_{frac} = 15.7%. Due to the computational divergence can occur with large fiber aspect ratio values (e.g., 40 as we used in Chapters Four and Five), we choose to fix the fiber aspect ratio at a_r = 15 to as the average for the polymer composite material. For this a_r and v_{frac}, N_p = 7.88 (cf. Equations 3-28 to 3-31). We note that the fiber aspect ratio we assumed may be lower than materials used in [134], while the numerical results obtained from aspect ratio of 15 are expected to exhibit similar trend as those obtained by applying a higher aspect ratio.

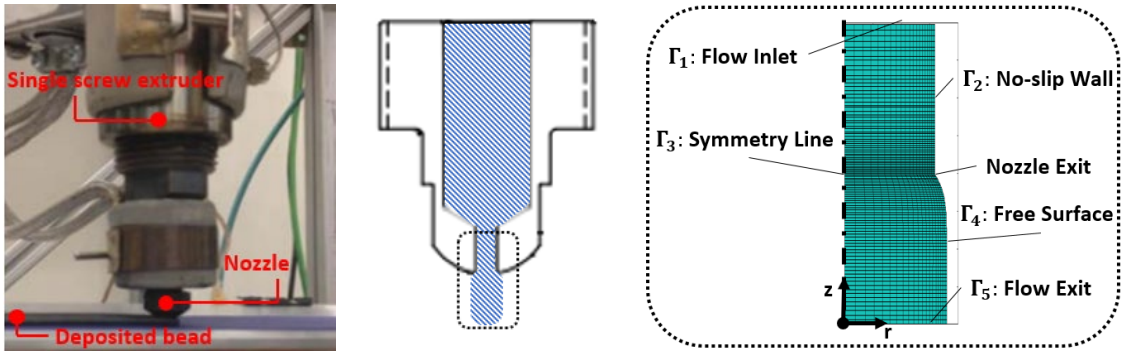

(A) (B) (C)

Figure 7-3. (A) Manufacturing Process of a LAAM Application; (B) Extruder Nozzle Geometry and Internal Flow Region; (C) Flow domain of Interest with Boundary Conditions Specified.

7.4 Convergence Criteria

As proposed, the overall coupled system is decomposed into the flow module and the fiber orientation module, iteratively computed in an alternating fashion. Both modules employ the N-R iteration method as described above. In this approach, the fiber orientation tensor field is fixed when the flow module is under computing and vice versa. Convergence is assumed when the difference of both flow and fiber orientation from one

iteration to the next fall within a predefined limit. Herein, the stopping criterion is set as 10^{-5} as in [135], i.e.,

$$\| \ {}^{h}\boldsymbol{d}^{e} - {}^{h-1}\boldsymbol{d}^{e} \ \| / \| \ {}^{h}\boldsymbol{d}^{e} \ \| \leq 10^{-5}, \tag{7-33}$$

where "‖ ‖" refers to the Frobenius norm of a vector [102], and *h* is the iterative index of the overall coupling scheme.

Additionally, the convergence criterion for the N-R iterative trials of solving the shear thinning flow fields and fiber orientation fields is set as the magnitude of the residual (e.g., ‖ $\boldsymbol{H}$ ‖ in Equation 7-16) of the final step solution is 10^{-5} of the residual solved in first integration. Specifically, the iterative procedure for identifying the free surface boundary stops till the error between the steady state die swell ratio values in two successive trials equal or less to 10^{-3} (i.e., $B^{(j)} - B^{(j-1)} \leq 10^{-3}$) which should be adequate as die swell ratio convergence often only within 0.1 in related literatures (e.g., see [19, 97, 128]).

7.5 Necessary Setup for the Algorithm

GFEM formulated equations (e.g., integral form of the $\boldsymbol{K}^{e}$ matrix appearing in Equation 7-13) are often evaluated through a numerical integration scheme [124]. As known, most of the finite element suites (e.g., ABAQUS, ANSYS-Polyflow [74]) employ numerical integration techniques in evaluating the integrals of finite element systems, which significantly reduces the cost of integral evaluations as compared to a direct integral computation (i.e., evaluating integrals in, for example, MATLAB with the corresponding command "int" [109]). Among the numerical integration methods, the Gauss-Quadrature (G-Q) approach [102] is one of the most widely used method adopted in commercial codes [124], and thus it is also employed in our developed algorithm. In

addition, it should be noted that the results of both flow fields and fiber orientation tensors shown in this section are computed exclusively by employing isoperimetric 8-node serendipity quadrilateral elements (e.g., see [124]). This is due to that the convergence performance of the flow and fiber orientation computations are much better when 8-node elements adopted than 4-node events, though a bit more computational cost is needed. Incorporate with which, the 3-point G-Q scheme is applied to yield a relatively smoother predicted profile of the free extrudate surface as compared to the fewer points involved G-Q evaluations.

Moreover, the penalty method employed in our code requires a scaling parameter γ_e. Herein, we assign $\gamma_e = 10^8$. This value is an intermediate value of the range suggested by [124] and has exhibited favorable results as compared to the results produced by commercial software, in our previous experiences.

Finally, through mesh sensitivity studies on the convergence behavior of die swell predictions of the flow domain of interest appearing in Figure 7-3C, a mesh size of "21-by-101-by-50" is identified as a sufficiently accurate yet computational effective quality for the modelled flow domain, otherwise meshes yields either less accuracy predicted results or non-convergent trials. Herein, "21-by-101-by-50" refers to a mesh design such that the nodes along radial direction is 21, and that along flow direction is 101, in which the free extrudate composes of 50 nodes longitudinally (i.e., the intersection node of the no-slip boundary and the free surface is sorted as a node of the no-slip wall boundary). We utilize Polyflow to generate the mesh of flow domain. In other words, the mesh of an uncoupled solution is applied to the flow domain in the very first iteration of the flow computation.

7.6 Results and Discussion

The developed code is first applied to a central disc thin cavity flow simulating the injection moulding scenario, which has been solved in the fully-coupled formulation in previous literature (e.g., [53, 94, 136]). Results solved from our code show a good agreement with the data published previously [53], through which it is convinced that our developed fully coupled scheme works properly. For consistency and conciseness, more detail of the verification problem is given in Appendix Part D.

In this following, computed results of a two-dimensional axisymmetric flow model simulating the polymer composite melt extrusion of a LAAM polymer deposition system are given. Specifically, to clearly show the coupling effects on the polymer composite melt in this scenario, we make two simulation events: 1) the fully-coupled simulation, which is solved with our proposed algorithm; and 2) the weakly-coupled simulation, which is also carried out through our code without iterative alternations between flow and fiber orientation solutions (i.e., solve flow fields firstly assigning the coupling factor $_p$ as zero, and then solve the fiber orientation with achieved flow fields).

7.6.1 Flow Fields Results

Flow fields contours computed by the weakly and fully coupled formulations appear in Figures 7-4 and 7-5, where results of $_r$ and $_z$ are given, respectively. Herein, $_r$ and $_z$ refer to the velocity components along r axis and θ axis of a cylindrical coordinate. Note that in Figures 7-4 and 7-5, the upper plane of the flow domain refers to the weakly-coupled solution and the rest refers to the fully coupled solution. In addition, the flow domain is shifted 90° clockwise to obtain a relatively larger view of

demonstration. To facilitate the comparison, the presented results are normalized by a factor of the averaged velocity such that [53]

$$v^{normal} = v/\bar{v}, \text{ and } \bar{v} = Q/(\pi r_o^2), \tag{7-34}$$

In the above, v refers to the computed results directly obtained from our code, Q is the volume flow rate and r_o is the radius of the nozzle tubular region (cf. Figure 7-3C). In addition, the flow domain is also normalized by a factor of r_o.

The given computed results exhibit significant differences between the weakly coupled and fully coupled solutions. In particular, the v_r contours are in a small magnitude (i.e., zero). Except that a large oscillation appears in the outer corner of the nozzle exit, where the weakly-coupled result exhibits much higher increment on v_r as compared to the fully coupled. The v_z contours appear in a similar trend in the internal nozzle tip region, while the results in the free extrudate are in notable difference, where the fully-coupled v_z contour developed for a longer distance to reach a steady-state (i.e., v_z contour in a uniform color) and the absolute magnitude of the steady-state v_z of the fully-coupled solution seems higher than that of the weakly-coupled results.

Moreover, the velocity profiles of the flow domain are specifically plotted at some characteristic positions as appearing in Figures 7-6 and 7-7, which provide a detailed view of the differences observed in the previous comparisons. Note that, $z/r_0 = 10, 5, 0$ refer to the locations of flow inlet, nozzle exit and flow exit, respectively. In the v_r-versus-r profiles appear in Figure 7-6, it can be seen that the difference within the nozzle (i.e., $z/r_0 = 6.2$) is only seen in the middle of the flow domain while that of the free extrudate (i.e., $z/r_0 = 4.4$) is notably observed across the radial direction. Particularly for the results of free extrudate , the normalized v_r at the nozzle exit outer

corner (i.e., $r/r_0 = 1$), solved by the fully coupled formulation, is 0.028, which exhibits a reduction of ~ 50% as compared to the same value solved by the weakly coupled scheme (which is 0.0576). Furthermore in Figure 7-7, the differences in the profiles of v_z-versus-r are also pronounced in the free extrudate portion of the flow domain, such that at the location of $z/r_0 = 4.4$, the v_z at the axis of symmetry (i.e., $r/r_0 = 0$), solved by the weakly-coupled formulation, is -1.035, while the same value solved by the fully-coupled scheme is -1.314, which is 27% higher of the weakly coupled solution regardless of the minus sign (i.e., only indicates the flow direction). In addition, the v_z at flow exit (i.e., $z/r_0 = 0$) are fully coupled solution of -0.808 and -0.910, solved separately by the weakly coupled and fully coupled schemes. In other words, the velocity field along the flow direction exhibits an increment of 13% by considering the flow-fiber coupling effects. Considering the velocity results are normalized by a factor of the averaged velocity (i.e., $Q/(\pi r_o^2) = 0.101\mathrm{m/s}$,herein), the variation in the material deposition rate between the virgin PEI and 20% carbon fiber filled PEI is relatively considerable, which implies the importance of quantifying the inter-relations between the polymer flow and the reinforced short fillers.

Additionally, it is seen that the extrudate free surface profiles also exhibit significant difference between the weakly coupled and fully coupled solutions. In particular, the steady state die swell ratio B (cf. Equation 4-13) of the weakly coupled solution is 1.112, while that solved by the fully coupled formulation is 1.049. It can be seen that the die swell exhibits a reduction by a factor of ~ 2×, which is in favorable agreement of prior literature experimentally investigating the die swell of filled polymer systems (e.g., see Figure 4 in [137]). It is also important to note that the reduction of die

swell also may yield significant differences in the printing resolutions of LAAM-printed parts made of neat polymers and filled polymers.

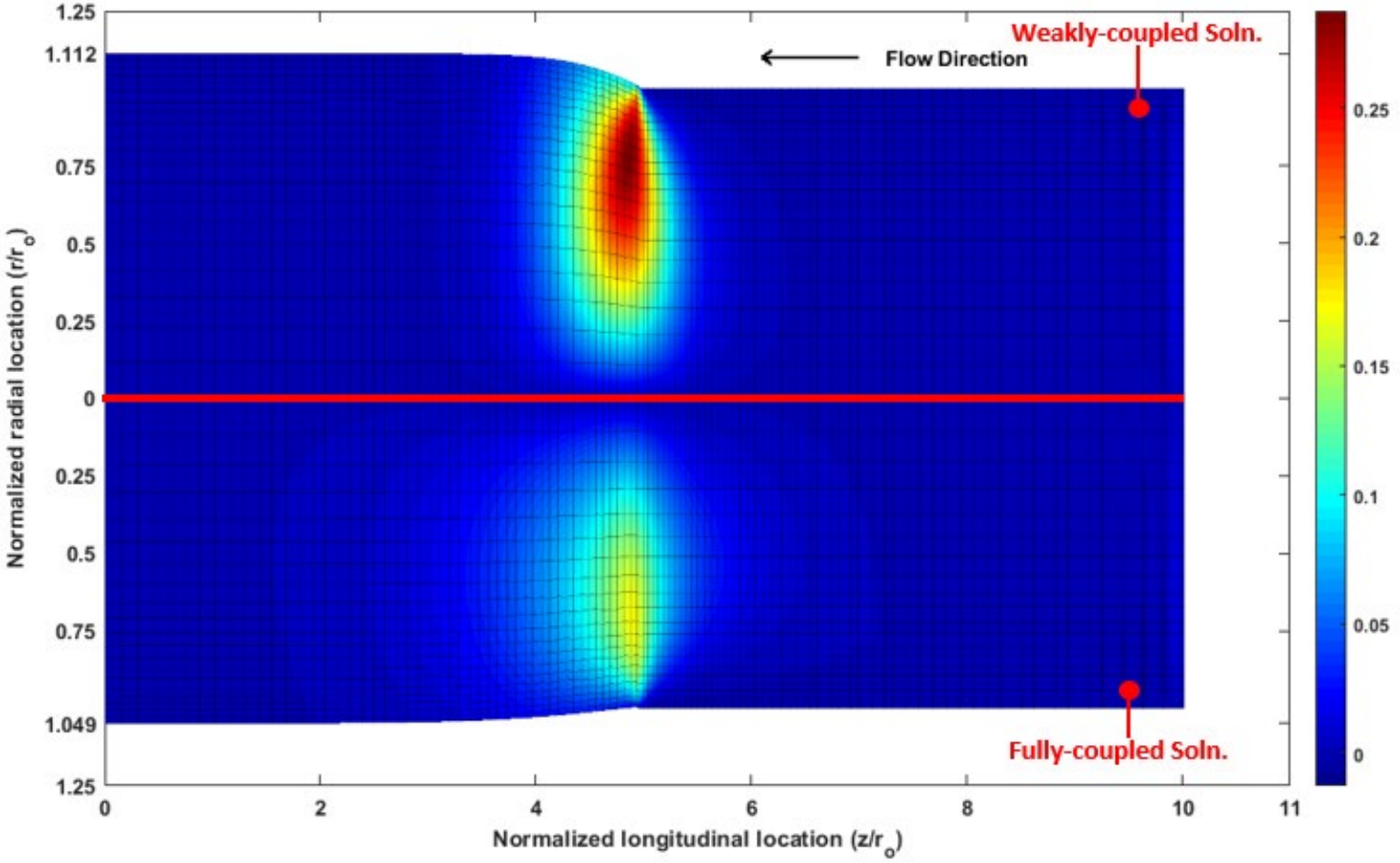

Figure 7-4. Velocity Contours of v_r Solved by Weakly Coupled and Fully Coupled Formulations.

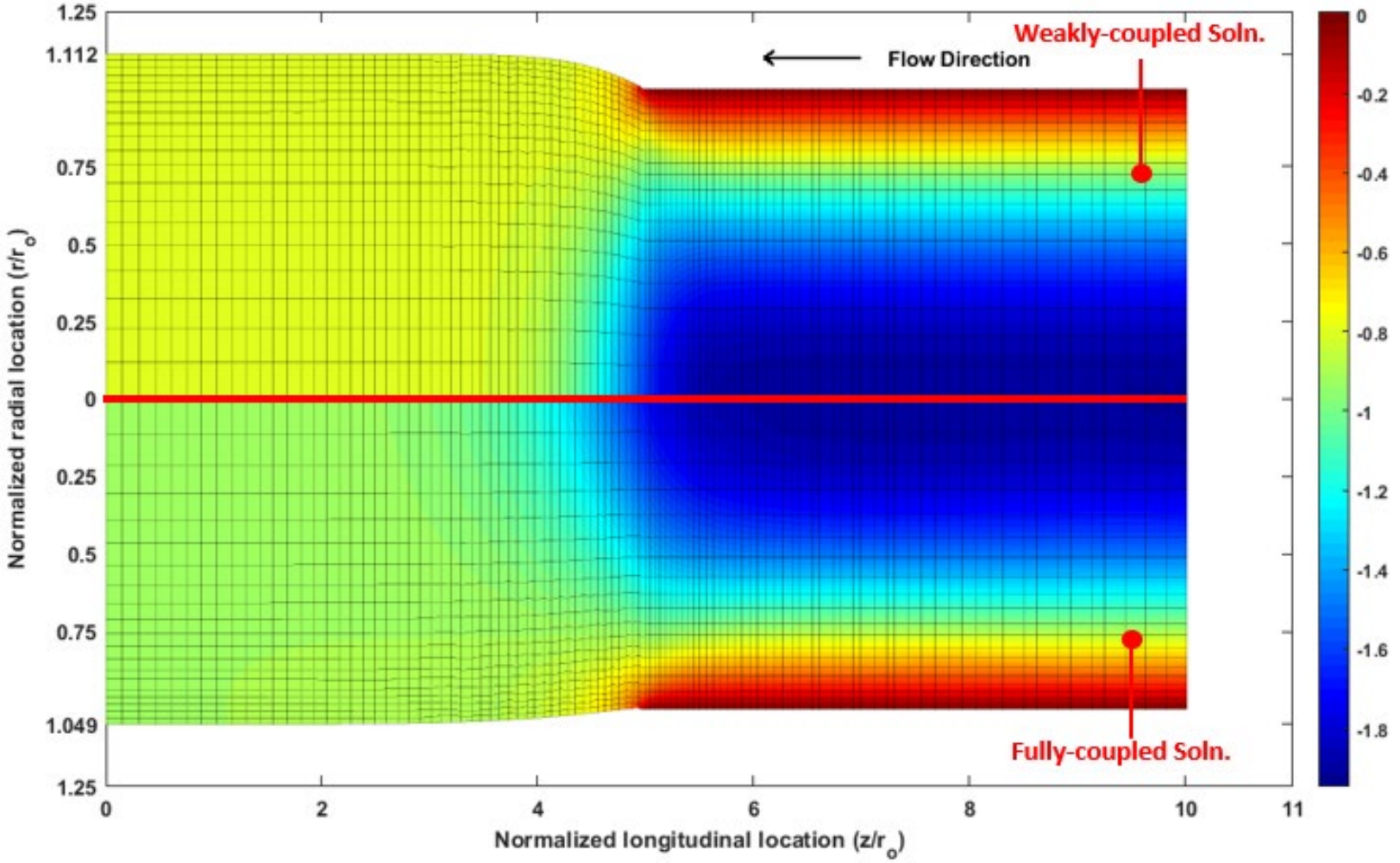

Figure 7-5. Velocity Contours of v_z Solved by Weakly Coupled and Fully Coupled Formulations.

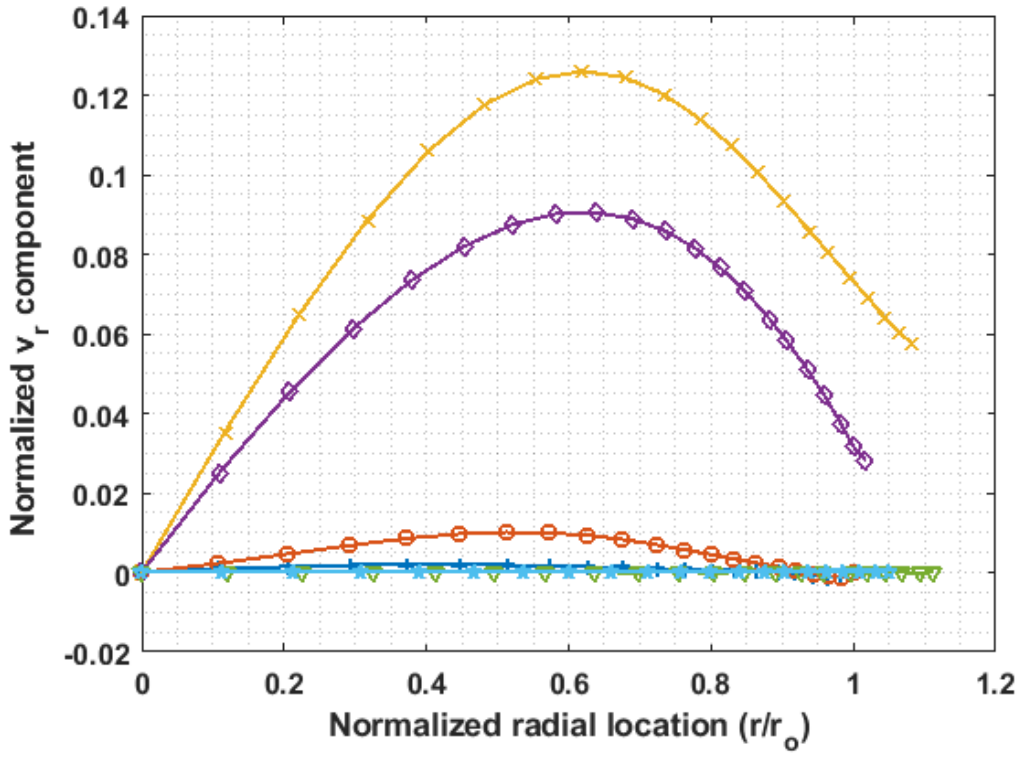

Figure 7-6. Velocity Profiles of v_r-versus-r Developing along Direction of Flow. Note, Legend Appears in Figure 6-7 Also Works in This Plot.

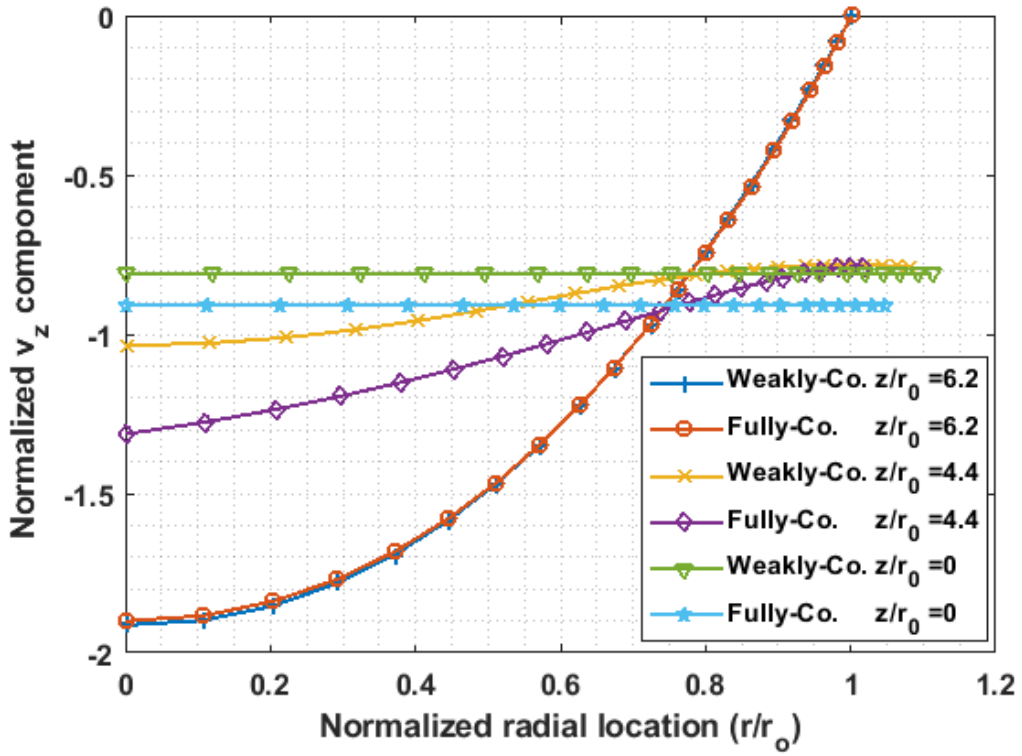

Figure 7-7. Velocity Profiles of v_z-versus-r Developing along Direction of Flow.

7.6.2 Fiber Orientation Results

Fiber orientation tensor solutions of weakly coupled and fully coupled schemes are shown in Figure 7-8 and 7-9, where results of A_{33} and A_{11} components appear, respectively. In addition to the contours, we visualize the solved second order orientation tensors through a vector field, in which the length and direction of each vector is determined by the largest eigenvalue of the tensor and the associated eigenvector, respectively [53]. It is important to note that the value of the diagonal components in a second order orientation tensor indicates how well the fibers are expected to align along that direction (e.g., A_{33} corresponds to the direction of x_3 in a 3D Cartesian coordinate system, which otherwise refers to the direction of the polymer flow).

Similar to the previous section, the upper plane of the flow domains appear in Figures 7-8 and 7-9 refers to the weakly-coupled solution and the bottom refers to the fully-coupled. From the demonstrated results, it is firstly seen that the fibers of the flow domain generally tend to align along the direction of flow, which is similar to results solved by several weakly coupled studies (e.g., see results in Chapter Four and Chapter Five). On the other hand, the fully coupled solution exhibits a higher fiber alignment along x_3 direction (i.e., flow direction) and less alignment along transverse directions (e.g., x_1) as compared to results solved by the weakly coupled scheme. In addition, the weakly coupled-solved orientation contours exhibit an obvious oscillation near the nozzle exit, which is especially seen in the outer edge of the nozzle exit in the contour of A_{11}. While this oscillatory trend is reduced by a significant amount in the results of fully-coupled solution.

Further information of the orientation tenor contours is plotted in Figures 7-10 and 7-11, where profiles of A_{33}-versus-r and A_{11}-versus-r are given at different locations of the flow domain. A first fact observed is that the results within the nozzle tip exhibit trivial bias in between the two sets of solutions, which implies the solid applicability of the weakly coupled scheme on internal narrow gap flows dominated by shear forces, as suggested by previous literature (e.g., see [22, 83]). However, the flow-fiber coupling effects cause significant deviation in the results of the free extrudate portion. For instance, at the flow exit (i.e., $z/r_0 = 0$, where the fiber orientation is assumed to reach somewhat a steady-state that can be used to represent the properties of a deposited bead), results of A_{33} component at $r/r_0 = 0$ are 0.47 and 0.55, solved by the weakly and fully coupled schemes separately. That is to say, counting the coupling effects between the flow and fiber orientation increases the principal fiber alignment (i.e., along direction of flow) of this location by 17%. Similarly to Chapters Four to Six, we estimate the elastic properties of the CF-PEI composites with our obtained fiber orientation tensor results at the flow exit. E and ν of PEI matrix material is set at 3 GPa and 0.4 [138], and the properties of carbon fiber constituent is the same as appearing in Table 4-5. The predicted elastic constants are given through Table 7-1, where the results of $\bar{E}_{33}$ component exhibit most notable difference. In detail, it is found that the bias between the fully-coupled solution and the weakly-coupled solution is about 7%. Note that, our current results does not include any upstream flow fields that can be significantly affected by the nozzle geometry. It can be expected that the bias between the weakly-coupled analysis and fully-coupled analysis on understanding the material properties of LAAM-deposited composites may be even higher.

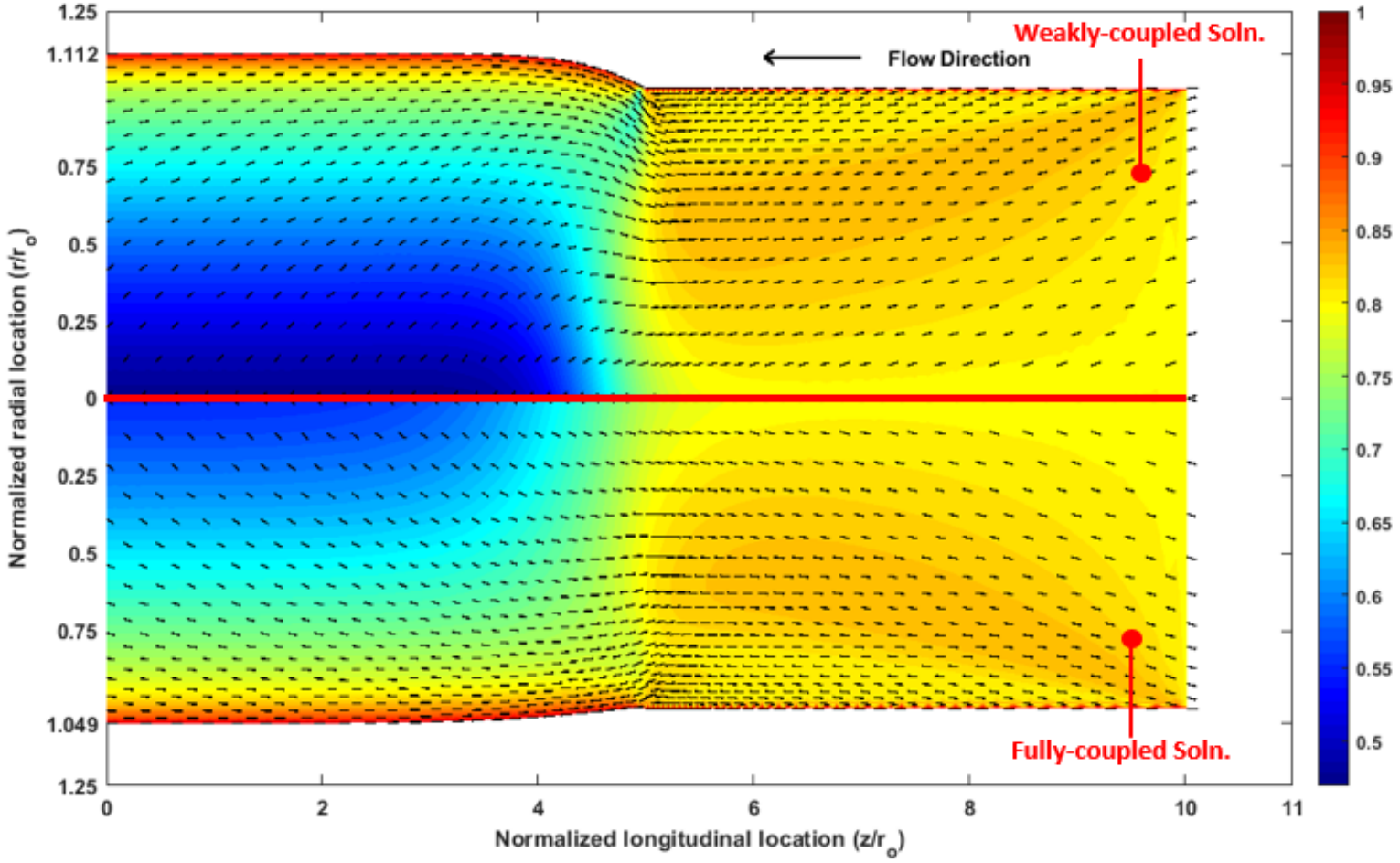

Figure 7-8. Fiber Orientation Contours of A_{33} (i.e., Third Diagonal of the Second Order Orientation Tensor Results) Solved by Weakly Coupled and Fully Coupled Formulations.

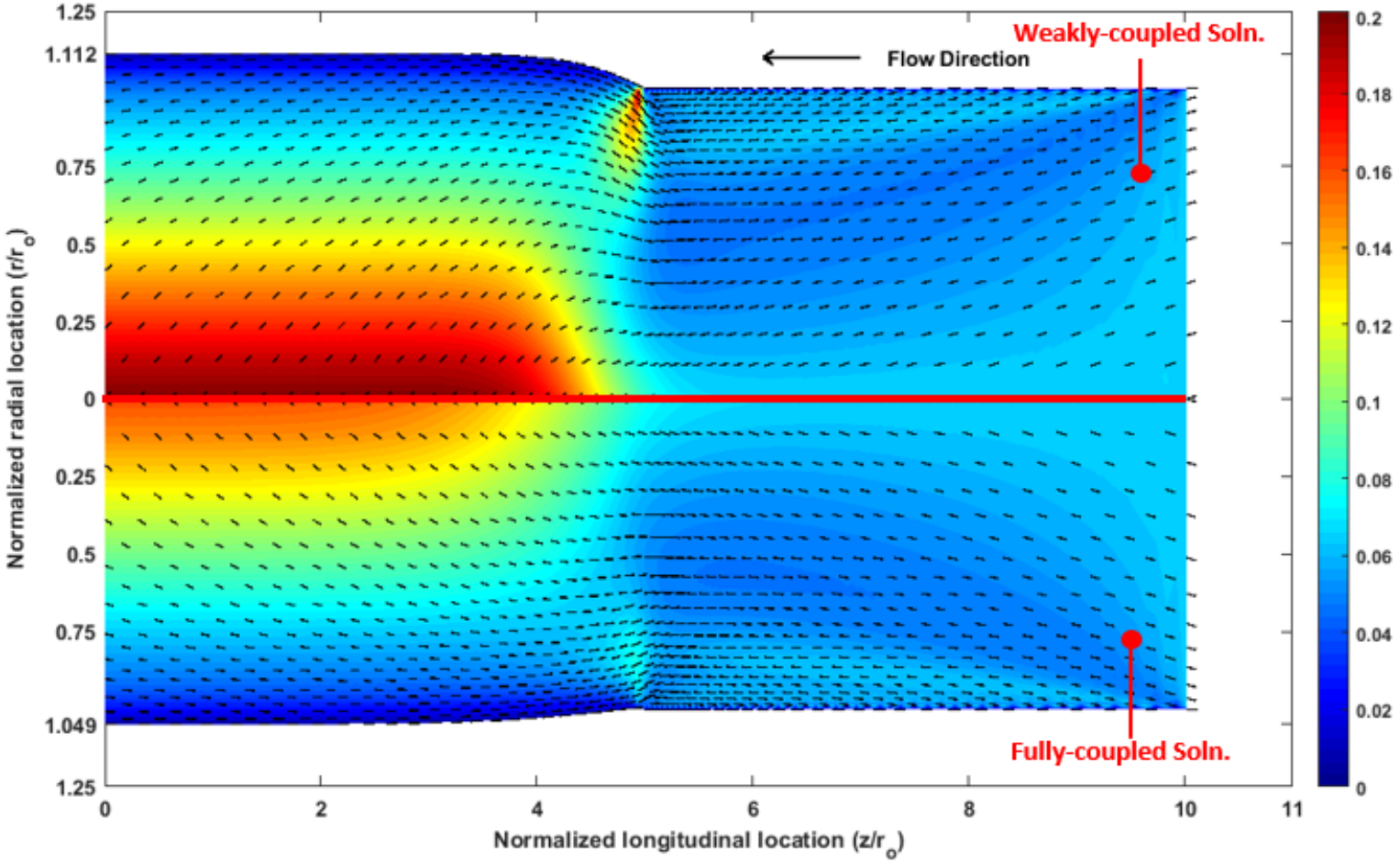

Figure 7-9. Fiber Orientation Contours of A_{11} (i.e., Third Diagonal of the Second Order Orientation Tensor Results) Solved by Weakly Coupled and Fully Coupled Formulations.

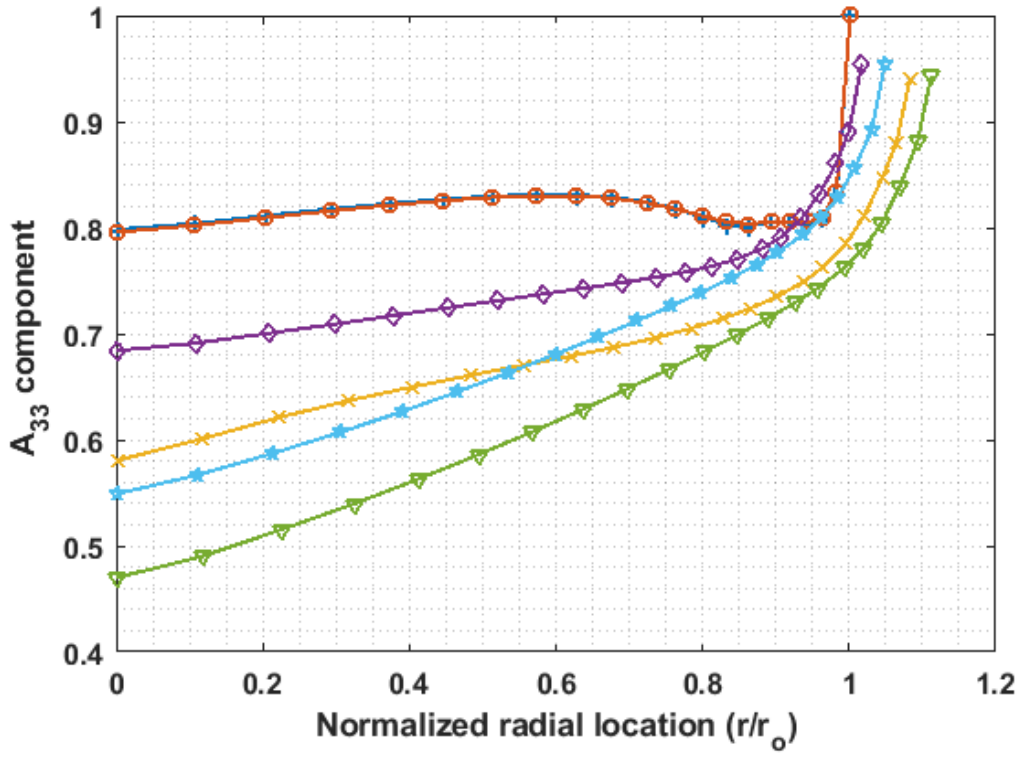

Figure 7-10. Profiles of A_{33}-versus-r Developing along Direction of Flow. Note, Legend Appears in Figure 6-11 Also Works in This Plot.

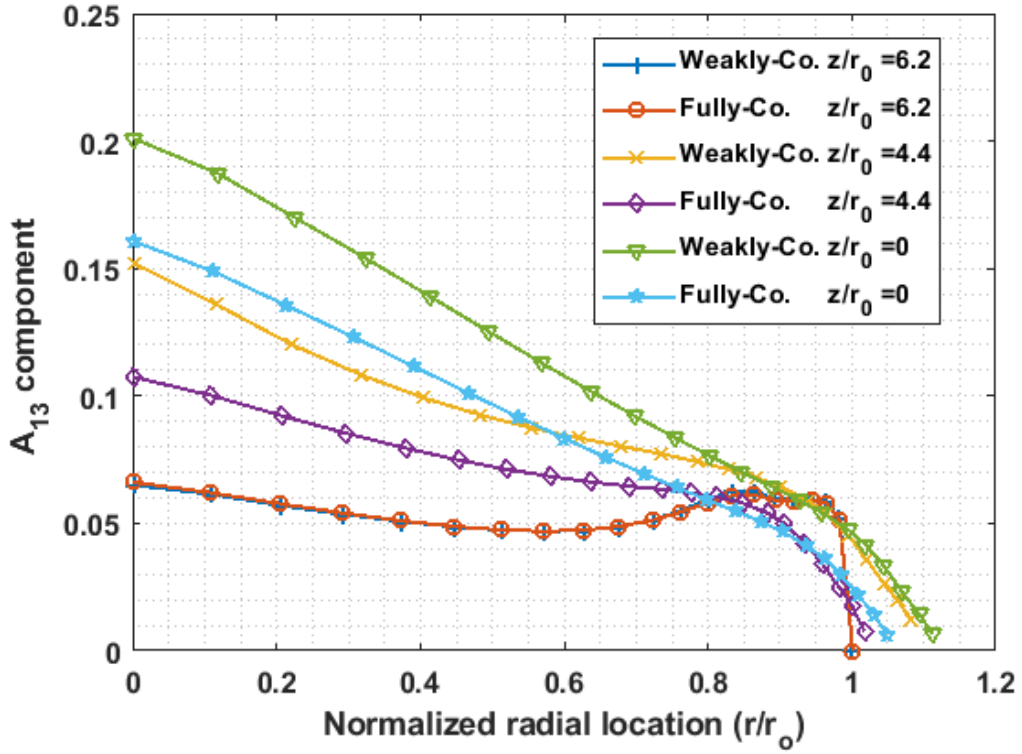

Figure 7-11. Profiles of A_{11}-versus-r Developing Along Direction of Flow.

Table 7-1. Computed Mean Elastic Constants of a 20% wt. CF-PEI Extrudate.

Solution	$\bar{E}_{11}$ (GPa)	$\bar{E}_{22}$ (GPa)	$\bar{E}_{33}$ (GPa)	$\bar{G}_{12}$ (GPa)	$\bar{G}_{13}$ (GPa)
Weakly-coupled	4.89	5.69	10.31	1.66	1.83
Fully-coupled	4.84	5.51	11.01	1.62	1.79

Table 7-1. Computed Mean Elastic Constants of a 20% wt. CF-PEI Extrudate (continued).

Flow model	$\bar{G}_{23}$ (GPa)	$\bar{\nu}_{12}$	$\bar{\nu}_{13}$	$\bar{\nu}_{23}$
Weakly-coupled	2.42	0.51	0.46	0.45
Fully-coupled	2.36	0.52	0.46	0.46

CHAPTER EIGHT

Summary and Future Works

Recent advancements of Large Area Additive Manufacturing (LAAM) polymer deposition combining the applications of fiber-filled polymers show the great potential of this energy-efficient manufacturing portfolio in fabricating light-weight large-scale composite structures and tooling for advanced engineering applications such as automobiles or aircrafts. Although promising future being seen (e.g., see [25, 103], where large-dimension parts and composite tooling are manufactured through the LAAM systems), the unclear relationships between manufacturing process parameters and the resulting properties of manufactured fiber filled polymer composite parts need to be addressed in order to enrich the applicability of the LAAM polymer deposition technology. This dissertation numerically models the complex flow physics and their inter-relations with the reinforced fibers including the non-Newtonian viscoelastic effects of the polymer melt, screw swirling kinematics effects and the fully-coupled fiber-flow effects on the fiber orientation and associated elastic properties of extruded composite materials as well as the fiber length attrition effects on the prediction of elastic properties in LAAM applications (cf. Figure 8-1), which contributes in bridging the knowledge gap of the unclear relationships between manufacturing process parameters and the resulting properties of manufactured fiber filled polymer composite parts.

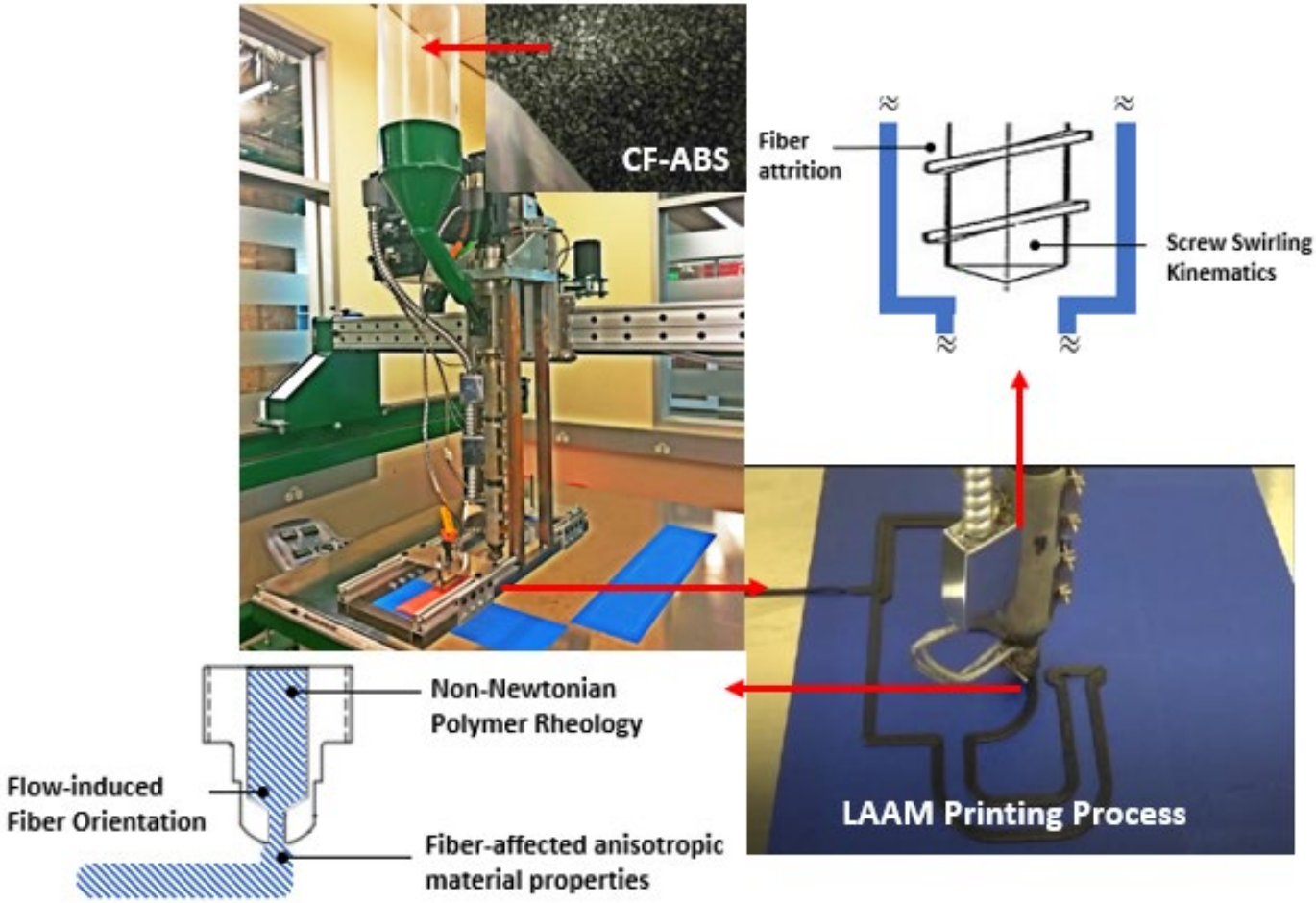

Figure 8-1. Explored Physics Associated with a LAAM Process of Polymer Composites.

Accomplishments through Chapters Four to Seven are particularly summarized as follows:

- Chapter Four: different categories of fluid flow models are applied to simulate the effects of polymer rheology in the nozzle orifice on the induced fiber orientation and associated elastic properties of composite feedstock processed, where the Newtonian model, Power law model, Carreau-Yasuda model, as well as a multi-mode PTT viscoelastic model and a Simplified Viscoelastic (SV) rheology model are investigated. Rheometry characterization of a virgin ABS polymer is carried out, from where the rheology properties obtained are implemented for the modeling. It was found that characterizing the melt flow by different rheology models yielded noticeable variation in predicted die swell, fiber orientation distribution and the ultimate elastic behavior of the extruded composites. The predicted die swell yielded by the PTT model was 50% higher than that of a Newtonian model result and over 100% higher those resulted by the generalized Newtonian Fluid (GNF) models (i.e., Power law and Carreau-Yasuda models). The SV model yielded die swell results that agreed well with those from the PTT model by careful adjustments of the rheology model parameters. Through the weakly couple formulation, the fiber orientation distribution within the extrudate was calculated from the melt flow velocity field with the Advani-Tucker equation. High fiber alignment in the direction of extrusion occurred near the high-shear flow edge region of the extrudate as well as the near-center region, which was due to the elongational effects of the free flow. Among the applied rheology models, the PTT model yielded the lowest principal fiber alignment while the Power law

model resulted in the highest fiber orientation in polymer extrusion direction. By employing the orientation homogenization method, the elastic properties of a printed extrudate of 13% CF-ABS were evaluated based on the predicted fiber orientation distributions, in which the estimated elastic modulus along extrusion direction showed noticeable variance across the extrudate. The numerically-integration-averaged elastic moduli generally match the published experimental work from preceding literature. The estimation indicated the composite extrudate exhibited quasi transverse isotropic behavior. In detail, the GNF models yielded higher Young's modulus along the principal direction while the PTT model resulted in a lower principal Young's modulus but higher values of shear moduli. This indicates that by considering the non-viscous rheology effects, the elastic properties of extrudate through AM systems reduced at longitudinal direction but increased at shear directions. In addition, the SV model yielded relatively similar data of fiber orientation distribution as well as elastic properties in comparison with the PTT model, especially in the shear dominant flow boundary, yet cost less computational time than the PTT model. In the future study of 3D deposition modelling of large-scale AM, the computationally cost-effective SV model is a reasonable alternative for conventional viscoelastic fluid models (e.g., PTT model).

- Chapter Five: the flow domain in a single screw extruder is simplified such that any hardware lying in the intersection region between the extruder and nozzle (e.g., valve or other structural components) is ignore, and essentially the screw tip, nozzle, and a strand of material beyond the nozzle exit where die swell occurs

are included to form a swirling flow model. With the created model, the screw swirling effects on the predicted fiber orientation and associated mean elastic properties of a polymer composite extrudate in a LAAM polymer deposition process are investigated. The weakly coupled analysis is performed to simulate the polymer melt flow and fiber orientation through a typical LAAM extrusion nozzle. The rheology properties of a molten 13% CF-ABS melt is fitted with a 5-mode viscoelastic PTT fluid model. The Wang-O'Gara-Tucker RSC fiber orientation model is applied to solve the fiber orientation state with computed kinematics of the uncoupled flows (i.e., flow fields are solved without any fiber effects counted). It is found that the swirling motion of the flow yields rotational streamlines and elongational flows that align fiber particles traveling along pathlines through the flow domain which differ from results computed for non-swirling flows. Additionally, the evolution of the second order orientation tensors through the flow domain exhibits significantly different trends if the consideration of swirling kinematics is included. In addition, the final orientation pattern of the extruded composite at the flow domain exit is different locally over the diameter of the bead when comparing swirling flow and straight flow models. Based on the computed steady-state orientation tensors with a prescribed orientation modelling parameter set, the effective elastic constants of a 13% CF-ABS are computed. The predicted principal tensile modulus from the swirling flow is 24.5% higher than that yielded by a straight flow. Moreover, the predicted data show more favorable agreement with previously published experimental data on a similar material system which supports our proposed methodology.

- Chapter Six: a statistics-based integration scheme is incorporated into the orientation homogenization method in estimating the effective elastic constants of a 13% wt. CF-ABS feedstock for LAAM systems, by which the screw-feeding-mechanism-resulted fiber aspect ratio distribution of the composite extruded can be included into consideration. The length of fibers in pellet feedstock and LAAM-deposited bead are measured. The fiber diameter is assumed to be non-affected through the single screw extrusion process and an average fiber diameter is estimated as 7 μm based on a related experimental work. The fiber aspect ratio of pellets and deposited beads are obtained by dividing the fiber length distribution measurements with the assumed constant diameter. A two-parameter Weibull probability distribution function is employed to characterize the statistical trends of measure fiber length data. The fiber aspect ratio distribution is then integrated into the orientation homogenization method to obtain the orientation-averaged elastic properties of a composite material extruded from LAAM applications. The fiber orientation of the extrudate is obtained from results of Chapter Four. The measured fiber length results show that the single screw extrusion degrades the length of fibers by a significant amount by comparing the measurements of the beads and pellets, such that the *PRD* of $\overline{a_r}$ in the pellet and bead results is 23.7%, indicating ~ 1/4 reduction on the fiber length geometry during the single screw extrusion process. On the other hand, the skewness of the fiber aspect ratio distribution in the bead results is smaller than that of the pellet results, such that the *PRD* between the mean and mode fiber aspect ratio of the pellet results is 16% which is more than three time larger of the *PRD* in the bead

results. Predicted mean elastic moduli of the 13% CF-ABS material vary locally across an extrudate bead, where the most intense variation of the properties is seen in property E_{33}, which is considered as a result of the fiber orientation of the extruded composites (i.e., fibers are highly aligned along the direction of the flow, which is the x_3 direction. Computed results of mean elastic constant $\bar{E}_{33}$ show significant differences when different sets of estimated fiber aspect ratio are implemented into the homogenization computation. If ignoring the fiber length attrition as well as the resulted distributed values of fiber aspect ratio, it is seen that the PRD of predicted $\bar{E}_{33}$ can be as high as 12%, i.e., comparing predicted $\bar{E}_{33}$ values by using {pellet measurement: $\bar{C}_{ijkl}(\overline{a_r})$} and {bead measurement: $\tilde{C}_{ijkl}^{\overline{a_r}^N}$} methods, respectively. In other words, it is of great importance to incorporate the fiber geometrical loss as well as the fiber aspect ratio distribution into the consideration of evaluating elastic properties of extruded composites in LAAM applications.

- Chapter Seven: to quantify the mutually dependent relations between the polymer melt flow and reinforced fiber kinetics, the governing equations of the isothermal creep flow and Advani-Tucker fiber orientation tensor approach are formulated by the Galerkin Finite Element Method and resulting systems of equations are solved through a customized MATLAB code. The GNF power law model is employed to characterize the shear thinning viscosity of the polymer melt of chosen material model, PEI. A one-dimensional streamline-wise remeshing technique is applied to identify the location of free extrudate die swell surface. The Streamline-Upwind Petrov Galerkin (SUPG) method is utilized to address the numerical instability.

Parameters of each mentioned numerical approaches are discussed delicately toward the convergence performance of the constructed program. Developed code is tested and validated through a thin-cavity-moulding central disc flow, where favourable agreement is seen between our computed results and those from prior literature. The algorithm is then tailored to characterize the coupled effects of flow/fiber-orientation solutions in a 2D axisymmetric nozzle tip flow with a short section of free extrudate, which represents the extrusion process of a LAAM application involved with the chose polymer feedstock, PEI, reinforced with 20% weight percentage discontinuous carbon fiber. The fully coupled solutions of flow fields exhibit notable differences as compared to the weakly-coupled simulation. In particular, the flow fields of v_r and v_z vary significantly due to the flow-fiber coupling effects, where the largest error between the weakly coupled and fully coupled results can be as high as 50% and 27% for v_r and v_z contours, respectively. The fully coupled solution of steady-state v_z component (i.e., at the flow exit) exhibits an increment of 13% as compared to the weakly coupled. In addition, the die swell ratio of the fully coupled solution exhibits a more than ~2× reduction as compared to the weakly-coupled-solved value, which generally matches the experimental reports on investigating die swell ratios of similar fill-polymers. Moreover, computed results of second orientation tensors also show great differences between the two sets of solutions, where the fiber alignment along the flow direction increases 17% by counting the flow-fiber coupling impacts. The mean elastic properties of $\bar{E}_{33}$ predicted using the weakly and fully coupled schemes exhibits a difference of 7%.

Regarding to the current achievements, future work is recommended as follows. Extending the MATLAB-customized fully coupled code presented in Chapter Seven to two and a half dimension flows, which otherwise may refer to the swirling flow studied in Chapter Five. This allows to count the interaction between the swirling kinematics included flow fields and the fiber orientation tensor fields. Another important improvement the proposed code may be to update the Advani-Tucker fiber orientation tensor of the flow domain with an advanced fiber orientation model, such as the RSC model that has been used in Chapters Four and Five. However, the scale parameter κ appearing in the RCS model governing equation (cf. Equation 3-17) as well as the coupling parameter N_p shown in Equation 3-28 require an in-depth investigation both numerically and experimentally to find proper values for these coefficients. Alternatively, recent publications of [79, 80] proposed another integrated form for counting the fiber orientation effects into the viscosity of the flow, where the above mentioned parameter fitting process is avoided. Hence, it is recommended to implement the anisotropic viscosity tensor approach given in [79, 80] to substitute Equation 3-28 for the coupling analysis.

In addition, experiments tailored toward validating the proposed simulations are needed as well. The geometry of the presented swirling flow model appearing in Chapter Five is a simplified version of the Model-19 extruder we refer to. A modified extruder is needed for further experimental validation, where the structural components in between the nozzle and upstream single screw extruder may be simplified. The simplified extruder can be used to generate samples of extrudate beads, from where fiber orientation tensor values can be measured experimentally and then used to compare with numerical

predicted values from swirling flow models. Moreover, we are also able to investigate the physical meaning of the scale factor κ (cf. Equation 3-17) and to explore the effective values of κ in quantifying the interactions between the screw swirling kinematics and the fiber orientation kinetics through the experimental-numerical combined analyses. Besides, a more rigorous investigation scheme is need for further validate the proposed homogenization approach appearing in Chapter Six. The procedure of fiber length measurements should be delicately designed to eliminate reading biases. Additionally, the elastic moduli of the deposited beads from where fiber attrition data are measure, should be quantified experimentally. Then the numerical predicted equivalent mean moduli can be directly verified with the experimental data.

APPENDICES

APPENDIX A

Tandon-Weng Equation

Tandon and Weng [87] developed a micromechanical model for predicting the elastic constants of aligned short fiber composites, which has been shown as a reliable numerical tool in numerical evaluations of the material properties of composite materials [88, 89]. The model can be written as [87]

$$E_{11} = \frac{E_m}{1+v_{frac}(A_1+2\nu_m A_2)/A}, \tag{A-1}$$

and

$$E_{22} = \frac{E_m}{1+v_{frac}[-2\nu_m A_3+(1-\nu_m)A_4+(1+\nu_m)A_5 A]/(2A)}, \tag{A-2}$$

and

$$G_{12} = G_m\left[1+\frac{v_{frac}}{\frac{G_m}{G_f-G_m}+2(1-v_{frac})S_{1212}}\right], \tag{A-3}$$

and

$$G_{23} = G_m\left[1+\frac{v_{frac}}{\frac{G_m}{G_f-G_m}+2(1-v_{frac})S_{2323}}\right], \tag{A-4}$$

and

$$\nu_{12} = \frac{\nu_m A-\nu_f(A_3-\nu_m A_4)}{A+\nu_f(A_1+2\nu_m A_2)}, \tag{A-5}$$

and

$$\nu_{23} = -1+\frac{E_{22}}{2G_{23}}, \tag{A-6}$$

For the above, fibers are aligned along x_1 direction. E, G, ν are tensile modulus, shear modulus and Poisson's ratio, respectively. v_{frac} refers to the fiber volume fraction and subscripts *m* and *f* denote the matrix and fiber, respectively. In addition, the material constants A_1, A_2, A_3, A_4, A_5, and A,are

$$A_1 = D_1(B_4 + B_5) - 2B_2, \tag{A-7}$$

and

$$A_2 = (1 + D_1)B_2 - (B_4 + B_5), \tag{A-8}$$

and

$$A_3 = B_1 - D_1B_3, \tag{A-9}$$

and

$$A_4 = (1 + D_1)B_1 - 2B_3, \tag{A-10}$$

and

$$A_5 = (1 - D_1)/(B_4 - B_5), \tag{A-11}$$

and

$$A = 2B_2B_3 - B_1(B_4 + B_5), \tag{A-12}$$

and constants B_i are

$$B_1 = v_{frac}D_1 + D_2 + (1 - v_{frac})(D_1S_{1111} + 2S_{2211}), \tag{A-13}$$

and

$$B_2 = v_{frac} + D_3 + (1 - v_{frac})(D_1S_{1122} + S_{2222} + S_{2233}), \tag{A-14}$$

and

$$B_3 = v_{frac} + D_3 + (1 - v_{frac})(S_{1111} + S_{2211} + D_1S_{2211}), \tag{A-15}$$

and

$$B_4 = v_{frac}D_1 + D_2 + (1 - v_{frac})(S_{1122} + D_1S_{2222} + S_{2233}), \quad \text{(A-16)}$$

and

$$B_5 = v_{frac} + D_3 + (1 - v_{frac})(S_{1122} + S_{2222} + D_1S_{2233}), \quad \text{(A-17)}$$

and constants D_j are written as

$$D_1 = 1 + \frac{2(G_f - G_m)}{\mathcal{L}_f - \mathcal{L}_m} \quad \text{(A-18)}$$

and

$$D_2 = \frac{\mathcal{L}_m - 2G_m}{\mathcal{L}_f - \mathcal{L}_m}, \quad \text{(A-19)}$$

and

$$D_3 = \frac{\mathcal{L}_m}{\mathcal{L}_f - \mathcal{L}_m}, \quad \text{(A-20)}$$

where $\mathcal{L}_f$, and $\mathcal{L}_m$ are Lame's constants that are expressed as

$$\mathcal{L}_f = \frac{E_f\nu_f}{(1+\nu_f)(1-2\nu_f)}, \quad \text{(A-21)}$$

and

$$\mathcal{L}_m = \frac{E_m\nu_m}{(1+\nu_m)(1-2\nu_m)}, \quad \text{(A-22)}$$

In addition, the non-zero components of the Eshelby tensor (S_{ijkl}) are [87]

$$S_{1111} = \frac{1}{2(1-\nu_m)}\left\{1 - 2\nu_m + \frac{3(a_r)^2-1}{(a_r)^2-1} - \left[1 - 2\nu_m + \frac{3(a_r)^2}{(a_r)^2-1}\right]g\right\}, \quad \text{(A-23)}$$

and

$$S_{2222} = \frac{3}{8(1-\nu_m)}\frac{(a_r)^2}{(a_r)^2-1} + \frac{1}{4(1-\nu_m)}\left[1 - 2\nu_m - \frac{9/4}{(a_r)^2-1}\right]g, \quad \text{(A-24)}$$

and

$$S_{3333} = S_{2222}, \quad \text{(A-25)}$$

and

$$S_{2233} = \frac{1}{4(1-\nu_m)}\left\{\frac{(a_r)^2/2}{(a_r)^2-1} - \left[1 - 2\nu_m + \frac{3/4}{(a_r)^2-1}\right] g\right\}, \tag{A-26}$$

and

$$S_{3322} = S_{2233}, \tag{A-27}$$

and

$$S_{2211} = \frac{-1}{2(1-\nu_m)}\frac{(a_r)^2}{(a_r)^2-1} - \frac{1}{4(1-\nu_m)}\left[1 - 2\nu_m - \frac{3(a_r)^2}{(a_r)^2-1}\right] g, \tag{A-28}$$

and

$$S_{3311} = S_{2211}, \tag{A-29}$$

and

$$S_{1122} = \frac{-1}{2(1-\nu_m)}\left[1 - 2\nu_m - \frac{1}{(a_r)^2-1}\right] + \frac{1}{2(1-\nu_m)}\left[1 - 2\nu_m + \frac{3/2}{(a_r)^2-1}\right] g, \tag{A-30}$$

and

$$S_{1133} = S_{1122}, \tag{A-31}$$

and

$$S_{2323} = \frac{1}{4(1-\nu_m)}\left\{\frac{(a_r)^2/2}{(a_r)^2-1} + \left[1 - 2\nu_m - \frac{3/4}{(a_r)^2-1}\right] g\right\}, \tag{A-32}$$

and

$$S_{3232} = S_{2323}, \tag{A-33}$$

and

$$S_{1212} = \frac{1}{4(1-\nu_m)}\left\{1 - 2\nu_m - \frac{(a_r)^2+1}{(a_r)^2-1} - \frac{2}{g}\left[1 - 2\nu_m - 3\frac{(a_r)^2+1}{(a_r)^2-1}\right]\right\}, \tag{A-34}$$

and additionally

$$g = \frac{a_r}{[(a_r)^2 - 1]^{3/2}}\left\{a_r[(a_r)^2 - 1]^{\frac{1}{2}} - \operatorname{acosh}(a_r)\right\} \tag{A-35}$$

The above concludes the equations of Tandon-Weng model.

APPENDIX B

Tangent Stiffness Matrices

The implementation of the N-R method for solving the shear thinning fluid flow as well as the second order orientation tensor fields requires the corresponding tangent stiffness matrices with respect to their finite element systems, respectively. In the following, the derivations of these tangent stiffness matrices are given sequentially. Firstly, for the non-linear flow system of a power law fluid, the tangent stiffness matrix is derived from a first order forward finite difference assumption such that

$$\boldsymbol{U^e} = \frac{d[\boldsymbol{H^e(v)}]}{d(\boldsymbol{v})} = \frac{\boldsymbol{H^e(v+\Delta v)-H^e(v)}}{\boldsymbol{\Delta v}}, \tag{B-1}$$

where $\boldsymbol{\Delta v}$ is a small increment with respect to the primary unknown $\vec{v}$. Plugging in the expression of $\boldsymbol{H^e(v)}$, in which Equations 7-12 to 7-14 are combined, we obtain that

$$\begin{aligned}\boldsymbol{U^e} = \int_\Omega [(\boldsymbol{B_s^e})^T\, \widetilde{\boldsymbol{V}}\, \boldsymbol{B_s^e}]\, d\Omega + \int_\Omega [(\boldsymbol{B_s^e})^T\, \widetilde{\boldsymbol{V}}\, \boldsymbol{B_s^e d^e}\, \tfrac{\partial \eta(\boldsymbol{N^e d^e})}{\partial \boldsymbol{d^e}}]\, d\Omega + \\ \gamma_e \int_\Omega [(\boldsymbol{B_s^e})^T\, \vec{\mathbf{1}}\, \vec{\mathbf{1}}^T\, \boldsymbol{B_s^e}] d\Omega,\end{aligned} \tag{B-2}$$

$\frac{\partial \eta(\boldsymbol{N^e d^e})}{\partial \boldsymbol{d^e}}$ is unknown in the above. Applying the forward Euler assumption (e.g., see [102]), we obtain that

$$\frac{\partial \eta(\boldsymbol{N^e d^e})}{\partial \boldsymbol{d^e}} = \frac{n-1}{(\dot{\gamma})^2}\eta(\, \boldsymbol{\nabla_s N^e d^e})^T \widetilde{\boldsymbol{V}}\, \boldsymbol{\nabla_s}, \tag{B-3}$$

Ultimately, the tangent stiffness matrix with applying the power law can be finalized as

$$\boldsymbol{U^e} = \int_\Omega (\boldsymbol{B_s^e})^T\{\eta[\dot{\gamma}]\widetilde{\boldsymbol{V}} + \eta[\dot{\gamma}]\frac{n-1}{(\dot{\gamma})^2}\widetilde{\boldsymbol{V}}\boldsymbol{B_s^e}\boldsymbol{d^e}(\boldsymbol{d^e})^T(\boldsymbol{B_s^e})^T\,\widetilde{\boldsymbol{V}}^T\}\boldsymbol{B_s^e}\,d\Omega + \gamma_e \int_\Omega [(\boldsymbol{B_s^e})^T\,\vec{\boldsymbol{1}}\,\vec{\boldsymbol{1}}^T\,\boldsymbol{B_s^e}]d\Omega, \tag{B-4}$$

where $\eta[\dot{\gamma}]$ refers to the function appearing in Equation 3-8, and $\dot{\gamma}$ is the scalar magnitude of the rate-of-deformation tensor that is formed with the velocity tensor obtained in the previous step.

Note, a reduced numerical integration scheme is applied to evaluate the integral form appearing in Equation B-4, such that, e.g., if the first integral of Equation B-4 is computed through 3-point G-Q integration then the second part of Equation B-4 (i.e., "$\gamma_e \int_\Omega [(\boldsymbol{B_s^e})^T\,\vec{\boldsymbol{1}}\,\vec{\boldsymbol{1}}^T\,\boldsymbol{B_s^e}]d\Omega$") need to be evaluated through the 2-point G-Q integration (c.f. Reddy [124]).

Similarly, the tangent stiffness matrix of the GFEM-formulated fiber orientation tensor system can be obtained by expanding the corresponding residual of the system as

$$\boldsymbol{H_a^e} = \int_\Omega \left\{\left[\frac{(\widetilde{N}_a^e)^T\boldsymbol{N^e}}{\Delta t} + \left(\widetilde{\boldsymbol{N}}_\boldsymbol{a}^\boldsymbol{e}\right)^T\boldsymbol{v}\cdot\nabla\boldsymbol{N_a^e}\right]\boldsymbol{d_a^e}|^p + \left[\left(\widetilde{\boldsymbol{N}}_\boldsymbol{a}^\boldsymbol{e}\right)^T\boldsymbol{m} + \frac{(\widetilde{N}_a^e)^T\boldsymbol{N_a^e}\boldsymbol{d_a^e}|^{p-1}}{\Delta t}\right]\right\} d\Omega. \tag{B-5}$$

Note, $\widetilde{\boldsymbol{N}}_\boldsymbol{a}^\boldsymbol{e}$ is a revised form of the weight function based on the SUPG method (e.g., see Equation 7-31). Then, the tangent stiffness matric of the fiber orientation problem is obtained by taking the derivative of Equation B-6 with respect to $\boldsymbol{d_a^e}$ such that

$$\boldsymbol{U_a^e} = \int_\Omega \left\{\left[\frac{(\widetilde{N}_a^e)^T\boldsymbol{N^e}}{\Delta t} + \left(\widetilde{\boldsymbol{N}}_\boldsymbol{a}^\boldsymbol{e}\right)^T\boldsymbol{v}\cdot\nabla\boldsymbol{N_a^e}\right] + \left[\left(\widetilde{\boldsymbol{N}}_\boldsymbol{a}^\boldsymbol{e}\right)^T\frac{d(\boldsymbol{m})}{d(\boldsymbol{d_a^e})}\right]\right\} d\Omega, \tag{B-6}$$

In the above, the expression of $\frac{d(\boldsymbol{m})}{d(\boldsymbol{d_a^e})}$ is implicit, whose analytical form was derived by VerWeyst [135] through the orthotropic closure approximation. The final expression of

$\frac{d(\boldsymbol{m})}{d(\boldsymbol{d}_{\boldsymbol{a}}^{\boldsymbol{e}})}$ is computationally expensive to be implemented. A similar problem adopted the forward Euler approach on $\frac{d(\boldsymbol{m})}{d(\boldsymbol{d}_{\boldsymbol{a}}^{\boldsymbol{e}})}$ and the results exhibited subtle difference as compared to the analytical solution, while the accuracy of the results retained. Thus, we herein employ this finite difference assumption for $\frac{d(\boldsymbol{m})}{d(\boldsymbol{d}_{\boldsymbol{a}}^{\boldsymbol{e}})}$ with a small perturbation of 10^{-5}. More detail on expanding the finite difference form of $\frac{d(\boldsymbol{m})}{d(\boldsymbol{d}_{\boldsymbol{a}}^{\boldsymbol{e}})}$ can be found in [139].

APPENDIX C

Determination of the Scale for SUPG

Prior literature stressed the scale of the SUPG implementation, where an over-scaled SUPG may distort the results by a significant amount as compared to the "true" solution (e.g., Smith, et al. [132] and VerWeyst and Tucker [53]). Herein, three values of SUPG scale, i.e., α = 0, 0.5, 1, are investigated in solving an uncoupled a shear thinning power law fluid flow assuming the coupling effects and the numerical stability in the fiber orientation solution are independent. Through the results given in Figures C-1 to C-3, it is clearly seen that the no-SUPG-involved orientation tensor contour exhibits significant wiggles. In addition, the contour stops showing notable difference as the scale increasing from 0.5 to 1. Consequently, we end up choosing α = 0.5 as the scale of SUPG for the power law fluid simulations. Admittedly, there still exists some wiggles near the shear boundary of the flow domain, while it is considered to yield no significance variation to the data comparison between the weakly-coupled and full-coupled solved results, which is the main scope of this research. In addition, 0.5 is also a suggested scale of SUPG for a GFEM-formulated fiber orientation problem in VerWeyst and Tucker [53]. Hence, it is convinced that the value of 0.5 is a proper value for the scale of SUPG implementation in this study.

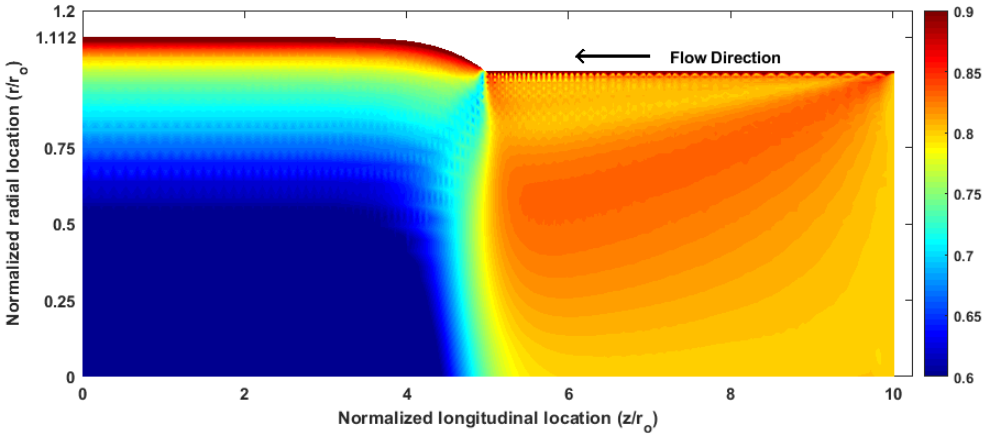

Figure C-1. A_{33} Component Contours Resulted from the SUPG Scaling Analysis at α=0.

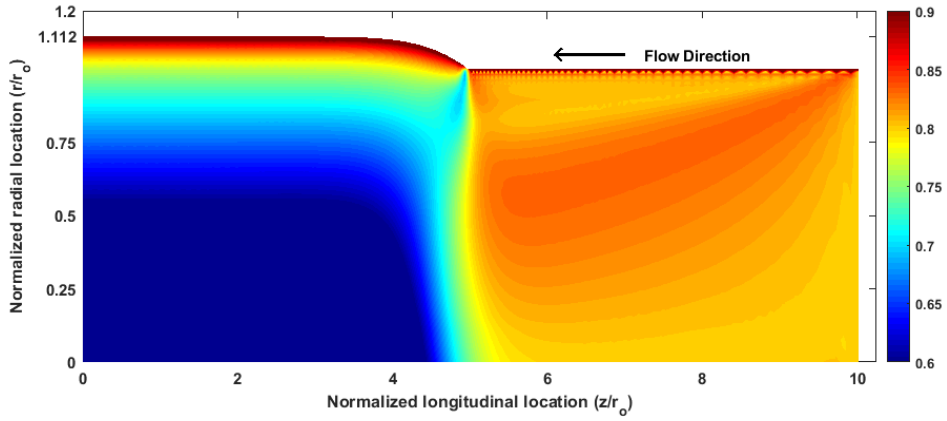

Figure C-2. A_{33} Component Contours Resulted from the SUPG Scaling Analysis at α=0.5.

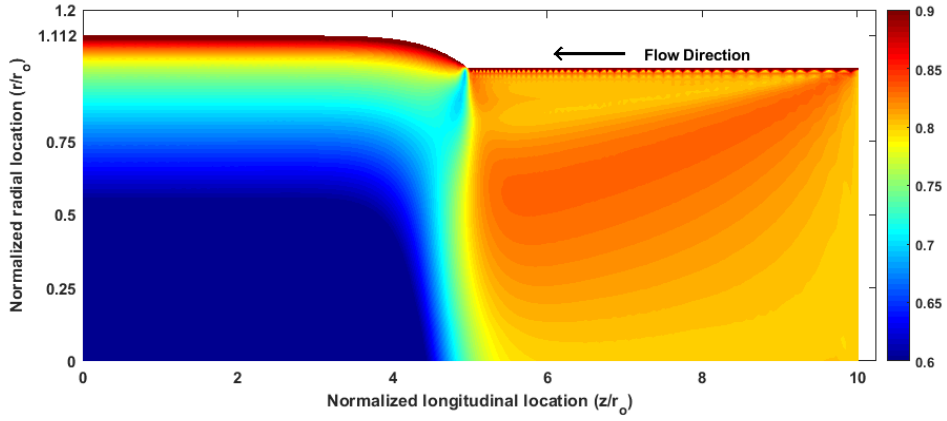

Figure C-3. A_{33} Component Contours Resulted from the SUPG Scaling Analysis at α=1.

APPENDIX D

Code Verification: Central Disc Flow

VerWeyst and Tucker [53] performed the coupled flow-fiber analysis on a central disc flow for injection moulding application. Herein, we employ the same conditions reported and compare our results with the published data. The flow domain and corresponding boundary conditions are shown in Figure D-1. A fully developed velocity profile is imposed at flow inlet based on the volume flow rate of 22.5 cm^3/s [53]. The flow solvent is Newtonian, and the viscosity is 1000 Pa s. N_p is set as 7.75 and flow domain is meshed with 4-node quadrilateral elements as did in one of VerWeyst's paper [53]. The time step is set as 10^{-4} initially, and after 68 times of coupling iterations (which is running for a sufficiently long period of time), the code is manually terminated and a large time step of 5×10^{-4} is imposed for another 10 and 50 times, respectively.

The results obtained from the three runs are given through Figures D-2 and D-3. Notice, the velocity components appearing in Figure D-2 are normalized using the same approach as proposed by VerWeyst and Tucker [53] (e.g., see Equation 7-34). The 'soln. #1' appearing in the legends of Figures D-2 and D-3 refers to the results obtained after the first 68 times coupling iterations with step size of 10^{-4}, and then 'soln. #2' and 'soln. #3' refer to separately the results obtained with additional 10 and 50 coupling iterations with step size of 5×10^{-4}.

The major deviation between our results and the reported is in Figure D-3A, where results of the fiber orientation tensor component A_{11} at the initial portion of the

mold thin cavity are compared. The error is main contributed by that a fully alignment along flow direction is imposed in our code (as suggested by [94] to ensure the convergence behavior of the code, while VerWeyst and Tucker [53] did not apply such assumption, as assuming their commercial software involved algorithm is more stable than ours. In exception to that, it is seen that the results yielded by the proposed code is approaching the published data closely, as the coupling iteration marching forward in the pseudo time domain. With a flow domain in large aspect ratio (as the one shown in Figure D-1), we note that the steady state of the coupled solution is seldom achieved numerically. However, the trends appearing in Figures D-2 and D-3 exhibit favourable agreement and thus the code is believed to yield reasonable estimations on the flow-fiber coupling effects in axial flow domains.

We notice that the later two cases (e.g., soln. #2, #3 appearing in Figures D-2 and D-3) consume much less time as compared to the first run with a step size of 10^{-4}. Due to the high degree of nonlinearity, the iterative coupling scheme has to start with a sufficiently small value of step size to ensure the convergence. While as the simulation runs to a much more stable condition after a significant amount of iterations, larger time steps can be applied and the convergence still retains (e.g., see [53]). In other words, an adaptive time step size can reduce the time consumption of the coupling code. This though beyond the scope of this research but is interesting to be investigated for optimizing the performance of proposed code in another in-depth study.

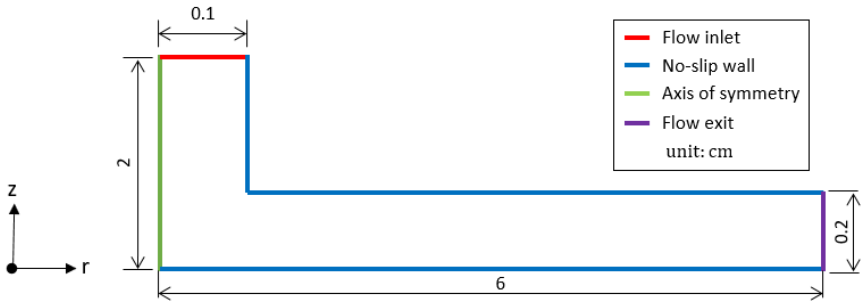

Figure D-1. 2D Axisymmetric Flow Domain Modelling of a Central Disc Injection Mold Internal Geometry.

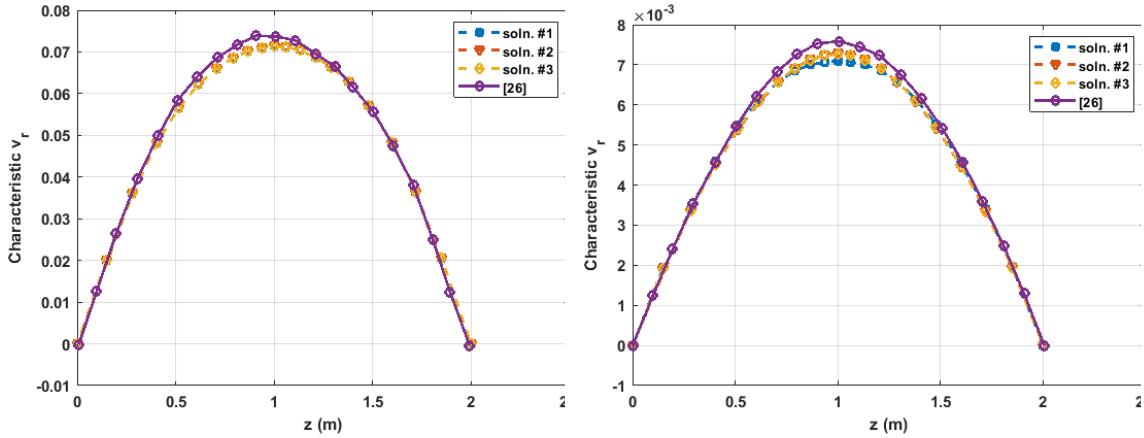

(A) (B)

Figure D-2. Normalized Radial Velocity Profiles along Gap-Wise Direction (z-direction) Computed by the Proposed Code and VerWeyst and Tucker [53]: (A) at z = 0.5 cm; (B) at z = 5 cm.

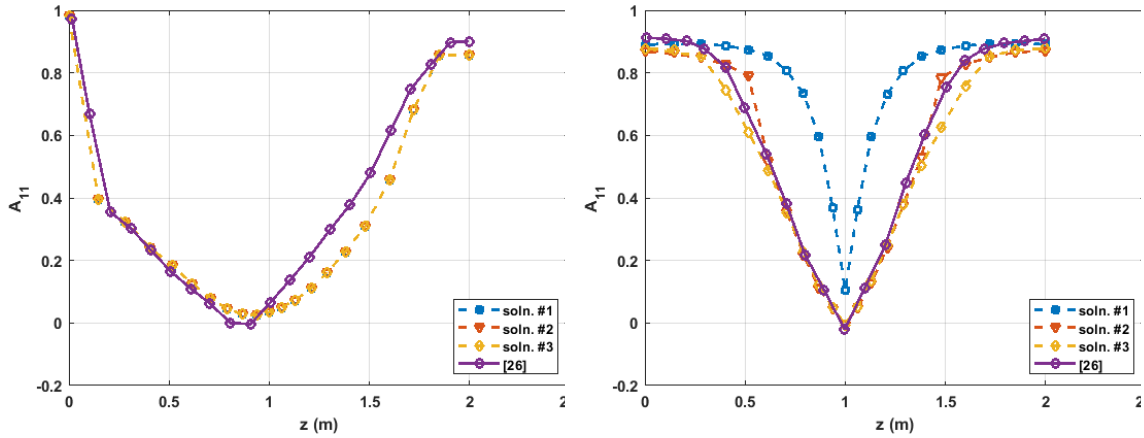

(A) (B)

Figure D-3. Fiber Orientation Tensor Component A_{11} Computed by the Proposed Code and VerWeyst and Tucker [53]: (A) at z = 0.5 cm; (B) at z = 5 cm.

BIBLIOGRAPHY

[1] L.J. Hornbeck, Digital light processing: a new MEMS-based display technology, Technical digest of the sensor symposium, The Institute of Electrical Engineers of Japan, 1996, pp. 297-304.

[2] B. Mueller, D. Kochan, Laminated object manufacturing for rapid tooling and patternmaking in foundry industry, Computers in Industry 39(1) (1999) 47-53.

[3] P.F. Jacobs, Rapid prototyping & manufacturing: fundamentals of stereolithography, Society of Manufacturing Engineers1992.

[4] D.L. Bourell, H.L. Marcus, J.W. Barlow, J.J. Beaman, Selective laser sintering of metals and ceramics, International Journal of Powder Metallurgy (Princeton, New Jersey) 28(4) (1992) 369-381.

[5] D. Feeney, FFF Vs. SLA Vs. SLS: 3D Printing. <https://www.sd3d.com/fff-vs-sla-vs-sls/#targetText=Speed%20and%20resolution%20of%20SLS,runs%20of%20small%2C%20precise%20parts>).

[6] B.L. Douglass, C.R. Douglass III, Fused filament fabrication system and method, Google Patents, 2016.

[7] W. Zhong, F. Li, Z. Zhang, L. Song, Z. Li, Short fiber reinforced composites for fused deposition modeling, Materials Science and Engineering: A 301(2) (2001) 125-130.

[8] R.W. Gray IV, D.G. Baird, J.H. Bøhn, Thermoplastic composites reinforced with long fiber thermotropic liquid crystalline polymers for fused deposition modeling, Polymer composites 19(4) (1998) 383-394.

[9] K.V. Wong, A. Hernandez, A review of additive manufacturing, ISRN Mechanical Engineering 2012 (2012).

[10] X. Gong, T. Anderson, K. Chou, Review on powder-based electron beam additive manufacturing technology, ASME/ISCIE 2012 international symposium on flexible automation, American Society of Mechanical Engineers Digital Collection, 2013, pp. 507-515.

[11] H. Bikas, P. Stavropoulos, G. Chryssolouris, Additive manufacturing methods and modelling approaches: a critical review, The International Journal of Advanced Manufacturing Technology 83(1-4) (2016) 389-405.

[12] C.E. Duty, V. Kunc, B. Compton, B. Post, D. Erdman, R. Smith, R. Lind, P. Lloyd, L. Love, Structure and mechanical behavior of Big Area Additive Manufacturing (BAAM) materials, Rapid Prototyping Journal 23(1) (2017) 181-189.

[13] A.A. Hassen, R. Springfield, J. Lindahl, B. Post, L. Love, C. Duty, U. Vaidya, R.B. Pipes, V. Kunc, The durability of large-scale additive manufacturing composite molds, CAMX 2016 (2016).

[14] Thermwood, LSAM - Large Scale Additive Manufacturing. <http://www.thermwood.com/lsam_home.htm>).

[15] M. Talagani, S. DorMohammadi, R. Dutton, C. Godines, H. Baid, F. Abdi, V. Kunc, B. Compton, S. Simunovic, C. Duty, Numerical simulation of big area additive manufacturing (3D printing) of a full size car, SAMPE Journal 51(4) (2015) 27-36.

[16] C. Eberle, D.C. Webb, T. Albers, C. Chen, Commercialization of new carbon fiber materials based on sustainable resources for energy applications, Oak Ridge National Laboratory (2013).

[17] C. Duty, J. Failla, S. Kim, T. Smith, J. Lindahl, V. Kunc, Z-Pinning approach for 3D printing mechanically isotropic materials, Additive Manufacturing 27 (2019) 175-184.

[18] J.R. Raney, B.G. Compton, J. Mueller, T.J. Ober, K. Shea, J.A. Lewis, Rotational 3D printing of damage-tolerant composites with programmable mechanics, Proceedings of the National Academy of Sciences 115(6) (2018) 1198-1203.

[19] B.P. Heller, D.E. Smith, D.A. Jack, Effects of extrudate swell and nozzle geometry on fiber orientation in Fused Filament Fabrication nozzle flow, Additive Manufacturing 12 (2016) 252-264.

[20] D. Zhang, D.E. Smith, D.A. Jack, S. Montgomery-Smith, Numerical evaluation of single fiber motion for short-fiber-reinforced composite materials processing, Journal of Manufacturing Science and Engineering 133(5) (2011) 051002.

[21] C. Duty, Personal Communication, 2017.

[22] S.G. Advani, C.L. Tucker III, The use of tensors to describe and predict fiber orientation in short fiber composites, Journal of rheology 31(8) (1987) 751-784.

[23] F. Folgar, C.L. Tucker III, Orientation behavior of fibers in concentrated suspensions, Journal of reinforced plastics and composites 3(2) (1984) 98-119.

[24] R.S. Bay, Fiber orientation in injection-molded composites: a comparison of theory and experiment, University of Illinois at Urbana-Champaign, 1991.

[25] L.J. Love, V. Kunc, O. Rios, C.E. Duty, A.M. Elliott, B.K. Post, R.J. Smith, C.A. Blue, The importance of carbon fiber to polymer additive manufacturing, Journal of Materials Research 29(17) (2014) 1893-1898.

[26] H. Ramanath, M. Chandrasekaran, C.K. Chua, K.F. Leong, K.D. Shah, Modelling of extrusion behaviour of biopolymer and composites in fused deposition modelling, Key Engineering Materials, Trans Tech Publ, 2007, pp. 1241-1244.

[27] H. Ramanath, C. Chua, K. Leong, K. Shah, Melt flow behaviour of poly-ε-caprolactone in fused deposition modelling, Journal of Materials Science: Materials in Medicine 19(7) (2008) 2541-2550.

[28] N. Mostafa, H.M. Syed, S. Igor, G. Andrew, A study of melt flow analysis of an ABS-Iron composite in fused deposition modelling process, Tsinghua Science & Technology 14 (2009) 29-37.

[29] B. N. Turner, R. Strong, S. A. Gold, A review of melt extrusion additive manufacturing processes: I. Process design and modeling, Rapid Prototyping Journal 20(3) (2014) 192-204.

[30] B.P. Heller, D.E. Smith, D.A. Jack, Planar deposition flow modeling of fiber filled composites in large area additive manufacturing, Additive Manufacturing 25 (2019) 227-238.

[31] S.K. Singh, Understanding the effect of extrusion processing parameters on physical, nutritional and rheological properties of soy white flakes based aquafeed in a single screw extruder, (2016).

[32] S. Goris, Experimental Study on Fiber Attrition of Long Glass Fiber-Reinforced Thermoplastics under Controlled Conditions in a Couette Flow, Annual technical conference and exhibition-Society of Plastics Engineers, 2017.

[33] Z. Ke, H. Zhongqi, Y. Shupan, C. Wanghua, Numerical simulation for exploring the effect of viscosity on single-screw extrusion process of propellant, Procedia Engineering 84 (2014) 933-939.

[34] S.V. Canevarolo, A.C. Babetto, Effect of screw element type in degradation of polypropylene upon multiple extrusions, Advances in Polymer Technology: Journal of the Polymer Processing Institute 21(4) (2002) 243-249.

[35] A.L. Kelly, E.C. Brown, P.D. Coates, The effect of screw geometry on melt temperature profile in single screw extrusion, Polymer Engineering & Science 46(12) (2006) 1706-1714.

[36] K. Ramani, D. Bank, N. Kraemer, Effect of screw design on fiber damage in extrusion compounding and composite properties, Polymer composites 16(3) (1995) 258-266.

[37] B. Hausnerová, N. Honkova, A. Lengálová, T. Kitano, P. Saha, Rheology and fiber degradation during shear flow of carbon-fiber-reinforced polypropylenes, Polymer Science Series A 48(9) (2006) 951-960.

[38] M. Aigner, D. Salaberger, T. Köpplmayr, B. Heise, S. Schausberger, A. Buchsbaum, D. Stifter, J. Miethlinger, Determining the orientation, distributions, and concentration of glass fibers in polymer matrix using X-ray computed tomography and optical coherence tomography images, Conference on Industrial Computed Tomography-Non destructive Testing, 3D Materials Characterisation und Dimensional Measurement, 2014, pp. 395-402.

[39] H. Zhuang, P. Ren, Y. Zong, G. Dai, Relationship between fiber degradation and residence time distribution in the processing of long fiber reinforced thermoplastics, Express Polym Lett 2(8) (2008) 560-568.

[40] R. Bailey, H. Kraft, A study of fibre attrition in the processing of long fibre reinforced thermoplastics, International Polymer Processing 2(2) (1987) 94-101.

[41] X. Jin, J. Wang, FIBER BREAKAGE CALCULATION FOR INJECTION MOLDED LONG FIBER COMPOSITES, 11th ANTEC Conference, 2011.

[42] J.H. Phelps, A.I.A. El-Rahman, V. Kunc, C.L. Tucker III, A model for fiber length attrition in injection-molded long-fiber composites, Composites Part A: Applied Science and Manufacturing 51 (2013) 11-21.

[43] Y. Béreaux, J.-Y. Charmeau, M. Moguedet, Modelling of fibre damage in single screw processing, International Journal of Material Forming 1(1) (2008) 827-830.

[44] T.L. Bayush, B. Thattai, S. Pillay, U. Vaidya, PROCESSING AND CHARACTERIZATION OF HEMP FIBER REINFORCED POLYPROPYLENE COMPOSITES, ECCM15 - 15TH EUROPEAN CONFERENCE ON COMPOSITE MATERIALS, Venice, Italy, 2012.

[45] G. Gamon, P. Evon, L. Rigal, Twin-screw extrusion impact on natural fibre morphology and material properties in poly (lactic acid) based biocomposites, Industrial Crops and Products 46 (2013) 173-185.

[46] A. Inoue, K. Morita, T. Tanaka, Y. Arao, Y. Sawada, Effect of screw design on fiber breakage and dispersion in injection-molded long glass-fiber-reinforced polypropylene, Journal of Composite Materials 49(1) (2015) 75-84.

[47] Z. Wang, D. Smith, Rheology effects on predicted fiber orientation and elastic properties in large scale polymer composite additive manufacturing, Journal of Composites Science 2(1) (2018) 10.

[48] Y. Zhang, Y. Chou, Three-dimensional finite element analysis simulations of the fused deposition modelling process, Proceedings of the Institution of Mechanical Engineers, Part B: Journal of Engineering Manufacture 220(10) (2006) 1663-1671.

[49] B. Brenken, Extrusion Deposition Additive Manufacturing of Fiber Reinforced Semi-Crystalline Polymers, Purdue University, 2017.

[50] E. BAROCIO, B. BRENKEN, A. FAVALORO, J. RAMIREZ, V. KUNC, R.B. PIPES, Fusion bonding simulations of semi-crystalline polymer composites in the extrusion deposition additive manufacturing process, Proceedings of the American Society for Composites—Thirty-second Technical Conference, 2017.

[51] B. Brenken, E. Barocio, A. Favaloro, V. Kunc, R.B. Pipes, Fused filament fabrication of fiber-reinforced polymers: A review, Additive Manufacturing 21 (2018) 1-16.

[52] J. Nixon, B. Dryer, D. Chiu, I. Lempert, D.I. Bigio, Three parameter analysis of fiber orientation in fused deposition modeling geometries, Annual Technical Conference - ANTEC, Conference Proceedings 2 (2014) 985-995.

[53] B.E. VerWeyst, C.L. Tucker III, Fiber suspensions in complex geometries: Flow/orientation coupling, The Canadian Journal of Chemical Engineering 80(6) (2002) 1093-1106.

[54] D.E.S. Zhaogui Wang, Simulation of Mutually Dependent Polymer Flow and Fiber Filled in Polymer Composite Deposition Additive Manufacturing, Solid Freeform Fabrication Symposium, Austin, TX, USA, 2019.

[55] T. Russell, B. Heller, D. Jack, D. Smith, Prediction of the fiber orientation state and the resulting structural and thermal properties of fiber reinforced additive manufactured composites fabricated using the big area additive manufacturing process, Journal of Composites Science 2(2) (2018) 26.

[56] J. Wang, J.F. O'Gara, C.L. Tucker III, An objective model for slow orientation kinetics in concentrated fiber suspensions: Theory and rheological evidence, Journal of Rheology 52(5) (2008) 1179-1200.

[57] J.P. Lewicki, J.N. Rodriguez, C. Zhu, M.A. Worsley, A.S. Wu, Y. Kanarska, J.D. Horn, E.B. Duoss, J.M. Ortega, W. Elmer, 3D-printing of meso-structurally ordered carbon fiber/polymer composites with unprecedented orthotropic physical properties, Scientific reports 7 (2017) 43401.

[58] M. Crochet, R. Keunings, Die swell of a Maxwell fluid: numerical prediction, Journal of Non-Newtonian Fluid Mechanics 7(2-3) (1980) 199-212.

[59] X.-L. Luo, R. Tanner, A pseudo-time integral method for non-isothermal viscoelastic flows and its application to extrusion simulation, Rheologica acta 26(6) (1987) 499-507.

[60] X.L. Luo, E. Mitsoulis, Memory phenomena in extrudate swell simulations for annular dies, Journal of Rheology 33(8) (1989) 1307-1327.

[61] C. Béraudo, A. Fortin, T. Coupez, Y. Demay, B. Vergnes, J. Agassant, A finite element method for computing the flow of multi-mode viscoelastic fluids: comparison with experiments, Journal of non-newtonian fluid mechanics 75(1) (1998) 1-23.

[62] V. Ganvir, A. Lele, R. Thaokar, B. Gautham, Prediction of extrudate swell in polymer melt extrusion using an Arbitrary Lagrangian Eulerian (ALE) based finite element method, Journal of Non-Newtonian Fluid Mechanics 156(1-2) (2009) 21-28.

[63] W. Limtrakarn, Y. Pratumwal, J. Krunate, C. Prahsarn, W. Phompan, T. Sooksomsong, W. Klinsukhon, Circular Die Swell Evaluation of LDPE Using Simplified Viscoelastic Model, King Mongkut's University of Technology North Bangkok International Journal of Applied Science and Technology 6(3) (2013) 59-68.

[64] N. Clemeur, B. Debbaut, A pragmatic approach for deriving constitutive equations endowed with pom–pom attributes, Rheologica Acta 46(9) (2007) 1187-1196.

[65] T.C. Papanastasiou, A.N. Alexandrou, Isothermal extrusion of non-dilute fiber suspensions, Journal of Non-Newtonian Fluid Mechanics 25(3) (1987) 313-328.

[66] J. Rosenberg, M. Denn, R. Keunings, Simulation of non-recirculating flows of dilute fiber suspensions, Journal of non-newtonian fluid mechanics 37(2-3) (1990) 317-345.

[67] A. Bellini, S. Güçeri, Mechanical characterization of parts fabricated using fused deposition modeling, Rapid Prototyping Journal 9(4) (2003) 252-264.

[68] E.R. Fitzharris, N. Watanabe, D.W. Rosen, M.L. Shofner, Effects of material properties on warpage in fused deposition modeling parts, The International Journal of Advanced Manufacturing Technology 95(5-8) (2018) 2059-2070.

[69] W. Michaeli, Extrusion dies for plastics and rubber: design and engineering computations Hanser Publishers, Munich, 2003.

[70] S.G. Advani, C.L. Tucker III, A numerical simulation of short fiber orientation in compression molding, Polymer composites 11(3) (1990) 164-173.

[71] R.S. Bay, C.L. Tucker III, Fiber orientation in simple injection moldings. Part I: Theory and numerical methods, Polymer composites 13(4) (1992) 317-331.

[72] Z. Tadmor, C.G. Gogos, Principles of polymer processing, John Wiley & Sons2013.

[73] D.G. Baird, D.I. Collias, Polymer processing: principles and design, John Wiley & Sons2014.

[74] A. Polyflow, Polyflow 15.0 user's guide, ANSYS, Inc 2013.

[75] G.B. Jeffery, The motion of ellipsoidal particles immersed in a viscous fluid, Proceedings of the Royal Society of London. Series A, Containing papers of a mathematical and physical character 102(715) (1922) 161-179.

[76] J.H. Phelps, C.L. Tucker III, An anisotropic rotary diffusion model for fiber orientation in short-and long-fiber thermoplastics, Journal of Non-Newtonian Fluid Mechanics 156(3) (2009) 165-176.

[77] N. Phan-Thien, X.-J. Fan, R. Tanner, R. Zheng, Folgar–Tucker constant for a fibre suspension in a Newtonian fluid, Journal of Non-Newtonian Fluid Mechanics 103(2-3) (2002) 251-260.

[78] H.-C. Tseng, R.-Y. Chang, C.-H. Hsu, An objective tensor to predict anisotropic fiber orientation in concentrated suspensions, Journal of Rheology 60(2) (2016) 215-224.

[79] H.-C. Tseng, R.-Y. Chang, C.-H. Hsu, The use of principal spatial tensor to predict anisotropic fiber orientation in concentrated fiber suspensions, Journal of Rheology 62(1) (2018) 313-320.

[80] A.J. Favaloro, C.L. Tucker III, Analysis of anisotropic rotary diffusion models for fiber orientation, Composites Part A: Applied Science and Manufacturing 126 (2019) 105605.

[81] J.G.V. Evans, The flow of a suspension of force-free rigid rods in a Newtonian fluid, University of Cambridge, 1975.

[82] G. Lipscomb II, M.M. Denn, D. Hur, D.V. Boger, The flow of fiber suspensions in complex geometries, Journal of Non-Newtonian Fluid Mechanics 26(3) (1988) 297-325.

[83] C.L. Tucker III, Flow regimes for fiber suspensions in narrow gaps, Journal of Non-Newtonian fluid mechanics 39(3) (1991) 239-268.

[84] S.M. Dinh, R.C. Armstrong, A rheological equation of state for semiconcentrated fiber suspensions, Journal of Rheology 28(3) (1984) 207-227.

[85] G. Ausias, J.-F. Agassant, M. Vincent, Flow and fiber orientation calculations in reinforced thermoplastic extruded tubes, International Polymer Processing 9(1) (1994) 51-59.

[86] J.S. Cintra Jr, C.L. Tucker III, Orthotropic closure approximations for flow‐induced fiber orientation, Journal of Rheology 39(6) (1995) 1095-1122.

[87] G.P. Tandon, G.J. Weng, The effect of aspect ratio of inclusions on the elastic properties of unidirectionally aligned composites, Polymer composites 5(4) (1984) 327-333.

[88] C.L. Tucker III, E. Liang, Stiffness predictions for unidirectional short-fiber composites: review and evaluation, Composites science and technology 59(5) (1999) 655-671.

[89] D.A. Jack, D.E. Smith, Elastic properties of short-fiber polymer composites, derivation and demonstration of analytical forms for expectation and variance from orientation tensors, Journal of Composite Materials 42(3) (2008) 277-308.

[90] D.N. Sibley, Viscoelastic Flows of PTT Fluid, 2010.

[91] A. Inc., in: A.P.U.s. Guide (Ed.) Canonsburg, PA, USA, 2013.

[92] C. Duty, C. Ajinjeru, V. Kishore, B. Compton, N. Hmeidat, X. Chen, P. Liu, A.A. Hassen, J. Lindahl, V. Kunc, What makes a material printable? A viscoelastic model for extrusion-based 3D printing of polymers, Journal of Manufacturing Processes 35 (2018) 526-537.

[93] B.P. Heller, Effects of nozzle geometry and extrudate swell on fiber orientation in Fused Deposition Modeling nozzle flow, 2015.

[94] S. Ranganathan, S.G. Advani, A simultaneous solution for flow and fiber orientation in axisymmetric diverging radial flow, Journal of Non-Newtonian Fluid Mechanics 47 (1993) 107-136.

[95] V. Verleye, Prediction of fiber orientation in complex injection molded parts, ASME Appl. Mech. Division 175 (1993) 139-163.

[96] K.J. Meyer, J.T. Hofmann, D.G. Baird, Initial conditions for simulating glass fiber orientation in the filling of center-gated disks, Composites Part A: Applied Science and Manufacturing 49 (2013) 192-202.

[97] K. Reddy, R. Tanner, Finite element solution of viscous jet flows with surface tension, Computers & Fluids 6(2) (1978) 83-91.

[98] Y.-c. Fung, A first course in continuum mechanics, Englewood Cliffs, NJ, Prentice-Hall, Inc., 1977. 351 p. (1977).

[99] Z. Wang, D.E. Smith, Numerical analysis of screw swirling effects on fiber orientation in large area additive manufacturing polymer composite deposition, Composites Part B: Engineering (2019) 107284.

[100] W. Cox, E. Merz, Correlation of dynamic and steady flow viscosities, Journal of Polymer Science 28(118) (1958) 619-622.

[101] K. Xiao, C. Tzoganakis, Rheological properties of HDPE-wood composites, SPE ANTEC; Society of Plastics Engineers: Houston, TX, USA 39 (2003) 975-979.

[102] C.C. Steven, Applied Numerical Methods With Matlab: For Engineers And Scientists, Tata McGraw Hill Education Private Limited2007.

[103] V. Kunc, Advances and challenges in large scale polymer additive manufacturing, Proceedings of the 15th SPE Automotive Composites Conference, Novi, MI, USA, 2015, pp. 9-11.

[104] T. Russell, A.J. David, Fiber Aspect Ratio Characterization and Stiffness Prediction in Large-Area, Additive Manufactured, Short-Fiber Composites, SPE ACCE 2019, Novi, Mi, USA, 2019.

[105] D. Jiang, D.E. Smith, Anisotropic mechanical properties of oriented carbon fiber filled polymer composites produced with fused filament fabrication, Additive Manufacturing 18 (2017) 84-94.

[106] W.K. Chin, H.T. Liu, Y.D. Lee, Effects of fiber length and orientation distribution on the elastic modulus of short fiber reinforced thermoplastics, Polymer Composites 9(1) (1988) 27-35.

[107] F. Ularych, M. Sova, J. Vokrouhlecḱy, B. Turčić, Empirical relations of the mechanical properties of polyamide 6 reinforced with short glass fibers, Polymer composites 14(3) (1993) 229-237.

[108] S.-Y. Fu, B. Lauke, Effects of fiber length and fiber orientation distributions on the tensile strength of short-fiber-reinforced polymers, Composites Science and Technology 56(10) (1996) 1179-1190.

[109] I. The MathWorks, MATLAB and Statistics Toolbox Release 2018b, Natick, Massachusetts, United States.

[110] T. Mori, K. Tanaka, Average stress in matrix and average elastic energy of materials with misfitting inclusions, Acta metallurgica 21(5) (1973) 571-574.

[111] N. Laws, R. McLaughlin, The effect of fibre length on the overall moduli of composite materials, Journal of the Mechanics and Physics of Solids 27(1) (1979) 1-13.

[112] R. Hill, A self-consistent mechanics of composite materials, Journal of the Mechanics and Physics of Solids 13(4) (1965) 213-222.

[113] B. Budiansky, On the elastic moduli of some heterogeneous materials, Journal of the Mechanics and Physics of Solids 13(4) (1965) 223-227.

[114] J. Halpin, Stiffness and expansion estimates for oriented short fiber composites, Journal of Composite Materials 3(4) (1969) 732-734.

[115] J. Hermans, Elastic Properties of Fiber Reinforced Materials When Fibers Are Aligned, Koninklijke Nederlandse Akademie Van Weteschappen-Proceedings Series B-Physical Sciences 70(1) (1967) 1-&.

[116] S.C. Tjong, Structural and mechanical properties of polymer nanocomposites, Materials Science and Engineering: R: Reports 53(3-4) (2006) 73-197.

[117] S.-Y. Fu, X.-Q. Feng, B. Lauke, Y.-W. Mai, Effects of particle size, particle/matrix interface adhesion and particle loading on mechanical properties of particulate–polymer composites, Composites Part B: Engineering 39(6) (2008) 933-961.

[118] D.A. Jack, Advanced analysis of short-fiber polymer composite material behavior, University of Missouri--Columbia, 2006.

[119] R.V. Hogg, McKean, J.W. and Craig, A.T., Introduction to Mathematical Statistics, Pearson Prentice Hall, Upper Saddle River, NJ2005.

[120] R.O. Ebewele, Polymer science and technology, CRC press2000.

[121] B.N. Sharma, S.A. Kijewski, L.S. Fifield, Y. Shin, C.L. Tucker, M.D. Sangid, Reliability in the characterization of fiber length distributions of injection molded long carbon fiber composites, Polymer Composites 39(12) (2018) 4594-4604.

[122] M.G. Carvalho, P.J. Ferreira, A.A. Martins, M.M. Figueiredo, A comparative study of two automated techniques for measuring fiber length, Tappi journal (2) (1997) 137-142.

[123] E. Bertevas, J. Férec, B.C. Khoo, G. Ausias, N. Phan-Thien, Smoothed particle hydrodynamics (SPH) modeling of fiber orientation in a 3D printing process, Physics of Fluids 30(10) (2018) 103103.

[124] J. Reddy, An introduction to the finite element method, McGraw-Hill New York, USA2004.

[125] D.H. Chung, T.H. Kwon, Numerical studies of fiber suspensions in an axisymmetric radial diverging flow: the effects of modeling and numerical assumptions, Journal of Non-Newtonian Fluid Mechanics 107(1-3) (2002) 67-96.

[126] A. Ben-Israel, A Newton-Raphson method for the solution of systems of equations, Journal of Mathematical analysis and applications 15(2) (1966) 243-252.

[127] A.S. Householder, Principles of numerical analysis, Courier Corporation 2006.

[128] R. Tanner, R. Nickell, R. Bilger, Finite element methods for the solution of some incompressible non-Newtonian fluid mechanics problems with free surfaces, Computer Methods in Applied Mechanics and Engineering 6(2) (1975) 155-174.

[129] M. Crochet, R. Keunings, On numerical die swell calculation, Journal of Non-Newtonian Fluid Mechanics 10(1-2) (1982) 85-94.

[130] A.N. Brooks, T.J. Hughes, Streamline upwind/Petrov-Galerkin formulations for convection dominated flows with particular emphasis on the incompressible Navier-Stokes equations, Computer methods in applied mechanics and engineering 32(1-3) (1982) 199-259.

[131] D.E. Smith, D.A. Tortorelli, C.L. Tucker III, Optimal design for polymer extrusion. Part I: Sensitivity analysis for nonlinear steady-state systems, Computer Methods in Applied Mechanics and Engineering 167(3-4) (1998) 283-302.

[132] D.E. Smith, D.A. Tortorelli, C.L. Tucker III, Optimal design for polymer extrusion. Part II: Sensitivity analysis for weakly-coupled nonlinear steady-state systems, Computer Methods in Applied Mechanics and Engineering 167(3-4) (1998) 303-323.

[133] C. Swaminathan, V. Voller, Streamline upwind scheme for control-volume finite elements, part I. Formulations, Numerical Heat Transfer, Part B Fundamentals 22(1) (1992) 95-107.

[134] C. Ajinjeru, V. Kishore, J. Lindahl, Z. Sudbury, A.A. Hassen, B. Post, L. Love, V. Kunc, C. Duty, The influence of dynamic rheological properties on carbon fiber-reinforced polyetherimide for large-scale extrusion-based additive manufacturing, The International Journal of Advanced Manufacturing Technology 99(1-4) (2018) 411-418.

[135] B.E. VerWeyst, Numerical predictions of flow-induced fiber orientation in three-dimensional geometries, (1999).

[136] S. Chung, T. Kwon, Numerical simulation of fiber orientation in injection molding of short ‐ fiber ‐ reinforced thermoplastics, Polymer Engineering & Science 35(7) (1995) 604-618.

[137] S.B. Kharchenko, J.F. Douglas, J. Obrzut, E.A. Grulke, K.B. Migler, Flow-induced properties of nanotube-filled polymer materials, Nature materials 3(8) (2004) 564.

[138] A. Materials, Supplier Data - Polyetherimide (PEI) (Goodfellow). <https://www.azom.com/properties.aspx?ArticleID=1883>).

[139] C. Tucker, E. Wetzel, S. Comas-Cardona, Mixing and microstructure control in polymer processing, University of Illinois at Urbana-Champaign, 1999 Summary of Engineering Research, University of Illinois at Urbana-Champaign: A Report of Activities During Calendar Year 1998(USA), 1999 (1999) 300.